Spring 2021

NANOELECTRONIC DEVICES FOR SENSITIVE DETECTION OF BIOMARKERS IN HEALTHCARE MONITORING

MD NIAZUL ISLAM KHAN
University of New Hampshire, Durham

NANOELECTRONIC DEVICES FOR SENSITIVE DETECTION OF BIOMARKERS IN HEALTHCARE MONITORING

BY

NIAZUL I. KHAN

MS, University of Ulm, Ulm, Germany 2012

BS, Bangladesh Univ. of Eng. & Tech. (BUET), Dhaka, Bangladesh 2009

DISSERTATION

Submitted to the University of New Hampshire

In Partial fulfillment of

The Requirements for the Degree of

Doctor of Philosophy

in

Electrical and Computer Engineering

May 2021

This dissertation has been examined and approved in partial fulfillment of the requirements for the degree of Doctor of Philosophy in Electrical & Computer Engineering by:

Dissertation Director, Dr. Edward Song,
Assistant Professor of Electrical & Computer Engineering
University of New Hampshire

Dr. John LaCourse
Professor of Electrical & Computer Engineering
University of New Hampshire

Dr. John Tsavalas
Associate Professor of Chemistry
University of New Hampshire

Dr. Qiaoyan Yu
Associate Professor of Electrical & Computer Engineering
University of New Hampshire

Dr. Young Jo Kim
Assistant Professor of Chemical Engineering
University of New Hampshire

On April 30, 2021

Original approval signatures are on file with the University of New Hampshire Graduate School.

DEDICATION

The dissertation is dedicated to-

My better half

Laboni Akter

My parents

Abdul Latif & Amena Begum

My son

Faizan Latif

ACKNOWLEDGEMENTS

This dissertation would not have been possible without the help of so many people. First of all, I would like to express my sincere gratitude to my PhD advisor, Dr. Edward Song, for believing in my ability and giving me the opportunity to work with him. It is his guidance, encouragement and support that made this dissertation a success. He spent a significant amount of his time discussing my research results, academic progress, and scientific writings. I would also like to thank him for maintaining the financial support throughout the PhD journey.

I would also like to thank my committee members, Prof. John LaCourse, Prof. Qioayan Yu, Prof. John Tsavalas, Prof. Young Jo Kim for their valuable time and important suggestions on my dissertation. Special thanks to Prof. Tsavalas for the fruitful discussions at different stages of my research as one of our collaborators.

I would like to thank my lab mates: Sujoy, Gaurab, Alec, Habib, Kaitlyn for their support and insightful discussions.

Finally, I would like to express my gratitude to my parents for their sacrifices to bring me at this position. Special gratitude to my mon who has been living in Bangladesh without the company of her only son and his family even after the demise of my dad. Her only satisfaction is that I succeed in my life.

Last but not the least, I would like to thank my wife, Laboni, for the support she provided me all through this journey. Without her support and constant company, it would not have been possible to reach this stage of my dissertation. I also thank my loving son, Faizan, who consistently inspired to work hard for this dissertation.

TABLE OF CONTENTS

LIST OF FIGURES

LIST OF TABLES

ABSTRACT

In recent years, nanomaterials have demonstrated their potential to enhance the sensitivity and utility of biosensors due to their superior electrical and mechanical properties. Specifically, carbon-based nanomaterials, such as carbon nanotubes (CNTs) and graphene have proven their practicality over other nanomaterials because of their low-cost, wide availability, high surface-to-volume ratio, and potential biocompatibility, to name a few. These nanomaterials when incorporated with biosensing devices are expected to enhance the critical sensing performances of the biosensors. Therefore, in this dissertation, these carbon nanomaterials are utilized to build nanoelectronic devices for highly sensitive and selective detection of protein biomarkers—biological molecules expressed in response to diseases like cancer, malaria, AIDS, Alzheimer's, etc. Graphene when used in field-effect transistor (FET) configuration has shown to be effective in biosensing. However, such graphene FET (GFET)-based biosensors suffer from several drawbacks, limiting their performances and usage. Thus, most of the work in my dissertation focuses on the development of graphene FET (GFET)-based biosensors for protein detection as well as the enhancement of performances by optimizing electrode design and integrating to microfluidics. The novelty of this work lies in the first detection of lysozyme, a model protein biomarker, with a limit of detection in the clinically relevant range. Moreover, this GFET platform is further advanced by integrating to microfluidics platform where real-time sensing of another protein biomarker, namely thrombin, is demonstrated with the lowest limit of detection reported so far with GFET.

For selective detection, biosensors are often equipped with a recognition element, alternatively known as the bioreceptor. Aptamers were used throughout this work because they offer a number of unique properties that make them a suitable candidate with respect to its counterparts such as antibodies and enzymes. Sensing performances and applicability of the sensors often depend on the proper functionalization of aptamers on the sensing surfaces. Therefore, this dissertation also focuses on the development of novel aptamer immobilization methods to enhance reproducibility, automation, as well as rapid, easy and mass-scale production. Besides GFET-based biosensors, a disposable low-cost electrochemical biosensor was also developed for the selective detection of lysozyme protein. The main goal of the project is to explore the feasibility of using inkjet-printing as a novel means for aptamer immobilization on electrodes.

CNTs mixed with aptamers at a certain ratio not only enhances the printability of the ink, but also augments the conductivity of the electrode. With this printing-based novel aptamer immobilization method, the detection of lysozyme was demonstrated with the sensitivity comparable to other conventional methods.

Finally, the flexibility of graphene is exploited to build a flexible GFET envisioned for wearable biosensor. To avoid the expensive and sophisticated microfabrication, the electrodes are printed with conductive silver ink on a flexible substrate. Kapton®, a polyimide film is chosen because of its flexibility, chemical and thermal stability. With this Kapton-based flexible GFET sensor, a real-time detection of interleukin-6 (IL-6) protein, a well-known cytokine and a key biomarker for various immune responses, was demonstrated for the first time.

In summary, the dissertation provides guidelines and insights for the development of highly sensitive nanoelectronic devices envisioned for a low-cost, highly reproducible, rapid, portable, and miniaturized biosensor for healthcare monitoring. In particular, this research sheds light on the feasibility of using carbon nanotubes (CNTs) and graphene for the exciting new applications in the field of biosensing.

CHAPTER 1: INTRODUCTION

1.1. Motivation

In ancient times, healthcare used to be provided at the patient's side – doctors used to visit the patients with whatever medical diagnostic tools they had to treat their patients (Figure 1.1). But with the advent of modern sophisticated and bulky medical instruments, healthcare has transferred from the patient's side to remote hospitals and diagnostic centers (Figure 1.2A). Nowadays, patients are required to visit a hospital or a clinic to receive healthcare. However, the situation becomes an issue in the developing countries where there is a shortage of enough hospitals and clinics as well as lack of proper means of transportation.

Figure 1.1. Healthcare system in ancient times. Doctors used to visit the patients to diagnose their diseases. (Source: www.chinesemedicalnews.com)

Recently, there has been a concerted effort to bring the healthcare back to the patient's side, where visiting a hospital or a doctor may be less frequent, thanks to the progress in miniaturization and portable technology that led to the development of point-of-care (POC) diagnostic devices. One of the examples of commercialized POC devices is the glucose sensor (Figure 1.2B) to monitor and quantify the sugar level in blood at home.

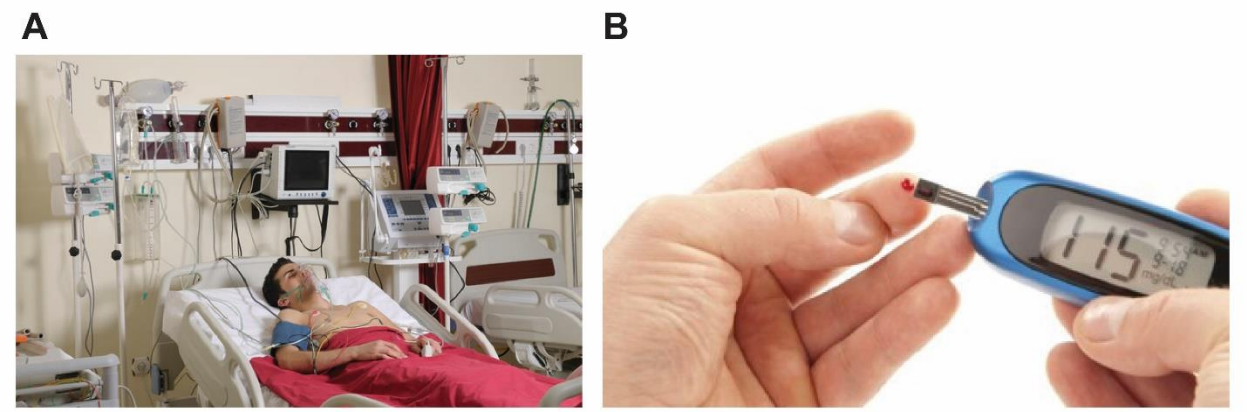

Figure 1.2. Transformation towards point-of-care: (A) bulky laboratory setup located at remote hospitals and clinics, and (B) the glucose POC device used to monitor and quantify sugar level in the blood.

One of the major components of these POC devices is the biosensor. Other applications of biosensors are drug delivery, environmental monitoring, soil quality monitoring, food quality monitoring, toxins of defense interest, water quality management, and prosthetic devices as illustrated in Figure 1.3. Due to the versatile applications of biosensors, the research on biosensors has been constantly boosting up, as seen by the exponential increase in the number of publications

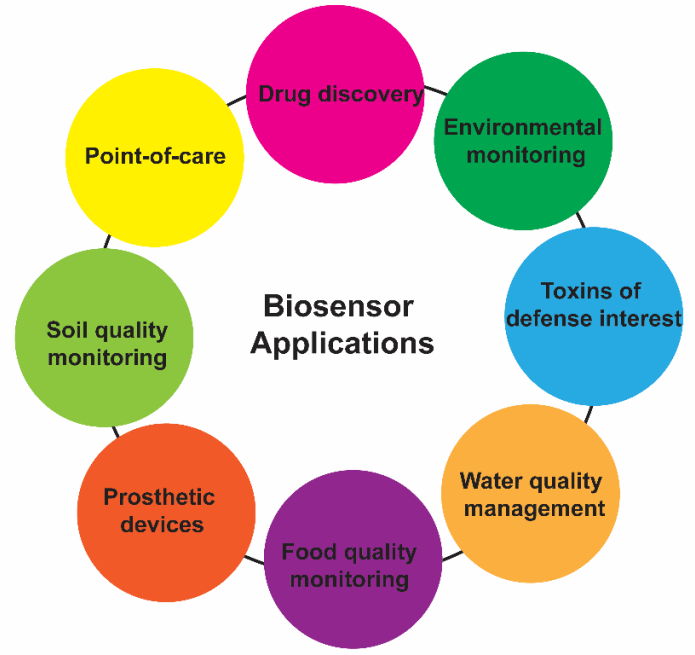

Figure 1.3. Applications of biosensors in different fields.

with a keyword ‘biosensor’ as presented in Figure 1.4A. Figure 1.4B shows the global market for biosensors that is quite large and is only expected to grow in the coming years as interest in food quality, health care monitoring, disease diagnostics, and national security continue to grow.

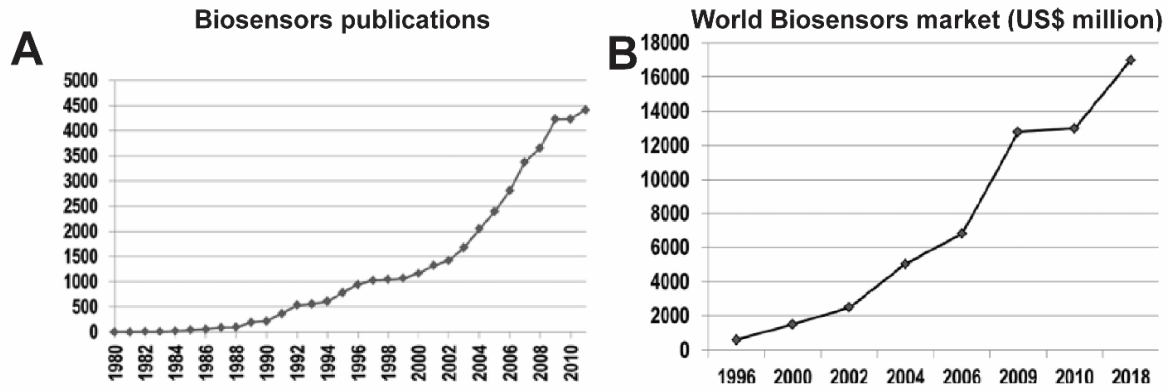

Figure 1.4. Graphs showing (A) the number of publications on the keyword “biosensor” during the period 1980 to 2011, and (B) the world market for biosensors estimated from various commercial sources. Adapted from [1].

1.2. Thesis Overview

The purpose of this thesis is to offer insight into the emerging technology in the development of biosensors. The focus of the thesis is to explore the field of nanoelectronics and nanoelectronic devices to enhance the sensitivity of nanobiosensors as well as to solve issues in conventional methods for functionalizing bioreceptors. Nanoelectronics which can simply be defined as the electronics of nanomaterials, are particularly important for biosensors because of the versatile advantages they incorporate to the sensing systems, such as high selectivity and sensitivity, biocompatibility, miniaturization, etc. Among different nanomaterials, carbon nanomaterials such as carbon nanotube and graphene provide exciting new opportunities for biosensing applications due to their extraordinary electrical and mechanical properties.

In this thesis, CNTs are used to develop an electrochemical biosensor for the detection of lysozyme protein which can act as a biomarker for a number of diseases such as breast cancer, Alzheimer’s, rheumatoid arthritis, malaria, etc. Herein, we also explore the possibility of using inkjet-printing to fabricate this biosensor by depositing CNT on the electrode. The concept of inkjet-printing has

been around for quite some time, but recently it has attracted much attention as a deposition technique due to its several advantages such as controllability of deposited ink with great precision, rapid and automated printing process at low-cost, printability of multiple materials simultaneously as well as easy development of microarrays. Moreover, inkjet-printing is an "additive" manufacturing technique as opposed to the "subtractive" manufacturing techniques like lithography, that significantly reduces the amount of material wastage.

Upon completion of this inkjet-printed CNT biosensor, another new carbon nanomaterial graphene is exploited to develop a field-effect transistor (FET) biosensor which is later integrated to microfluidics to extract the combined advantages of graphene and microfluidics, such as high sensitivity, flexibility, and compatibility with lab-on-a-chip devices.

The next goal is to push this GFET detection platform further towards flexible electronics to develop wearable biosensors, which are non-invasive devices that can be worn or mated with the human skin to continuously and closely monitor an individual's activities without interrupting or limiting the user's daily routine. To develop this flexible GFET, a flexible substrate is used to replace the rigid SiO_2/Si substrate. Here, I use Kapton®, a polyimide film as the flexible substrate due to the advantages it offers. To avoid the high cost and complexity in microfabrication, electrodes are formed by simply printing commercially available conductive silver ink on the flexible substrate.

1.3. Thesis Outline

This thesis presents the development and application of nanoelectronic devices for biosensing specially protein sensing. A major part of this thesis focuses on the development and application of GFET devices for detection of protein biomarkers. Apart from GFET-based biosensing, a novel inkjet-printed electrochemical biosensor is developed and applied for sensing of protein. To accommodate them along with the theoretical background, the thesis is divided into nine chapters.

Chapter 2 provides the theoretical background of biosensors—definition, history and evolution, and classification of biosensors of particular interest. A brief introduction to aptamers as recognition elements as well as to proteins as biomarkers is also presented. Chapter 3 presents the

background for carbon-based nanoelectronics, especially the electronics of two popular carbon nanomaterials, namely CNT and graphene.

Chapter 4 describes the development of the novel inkjet-printed biosensor. The chapter presents the detailed protocol for the CNT-aptamer ink preparation, characterization and measurements as well as discusses the results.

Chapter 5, 6 and 7 are built on the development and application of GFET-based sensors. Specifically, Chapter 5 describes the first detection of lysozyme protein with a nanomolar limit of detection. Chapter 6 further advances this GFET platform by integrating with microfluidics and demonstrates the sensing of another protein thrombin with picomolar limit of detection—lowest among the other GFET-based thrombin sensors reported so far. Chapter 7 discusses the extension of this rigid GFET to a flexible platform and presents the development of this flexible GFET on a polyimide film along with the demonstration of the real-time detection of a sweat-based protein, namely interleukin-6 (IL-6).

Chapter 8 presents a novel aptamer immobilization method on GFET platform where commercially available amine-linked aptamers are preconjugated with pyrene group and this pyrene tagged aptamers, soluble in water-based solvents, are exposed to GFETs. This chapter discusses the detailed process and characterization of the preconjugation as well as the measurement results showing the sensing of IL-6 protein as a representative analyte.

Finally, Chapter 9 presents the concluding remarks as well as future work.

CHAPTER 2: FUNDAMENTALS OF BIOSENSORS

2.1. What is a Biosensor?

According to the definition of International Union for Pure and Applied Chemistry (IUPAC), a biosensor is a self-contained integrated device which is capable of providing specific quantitative or semi-quantitative analytical instrumentation using a biological recognition element (biochemical receptor) in direct spatial contact with a transducer element [1]. It can simply be viewed as a device that converts a physical or biological event into a measurable signal. As can be seen in Figure 2.1, it consists of three main parts: (1) a biorecognition molecule or a bioreceptor (aptamer, tissue, microorganism, organelle, cell receptors, enzyme, antibody, protein, etc.) which is a biologically derived material or biomimetic component that provides selectivity to the target analyte, (2) a transducer (physicochemical, optical, piezoelectric, electrochemical, etc.) that converts the resulting signal from the interaction of the analyte to the biosensing element into a measurable and quantifiable signal (in most cases electrical signal), and (3) the associated electronics or data analysis system which is primarily responsible for signal processing and user-friendly visualization of the sensing results.

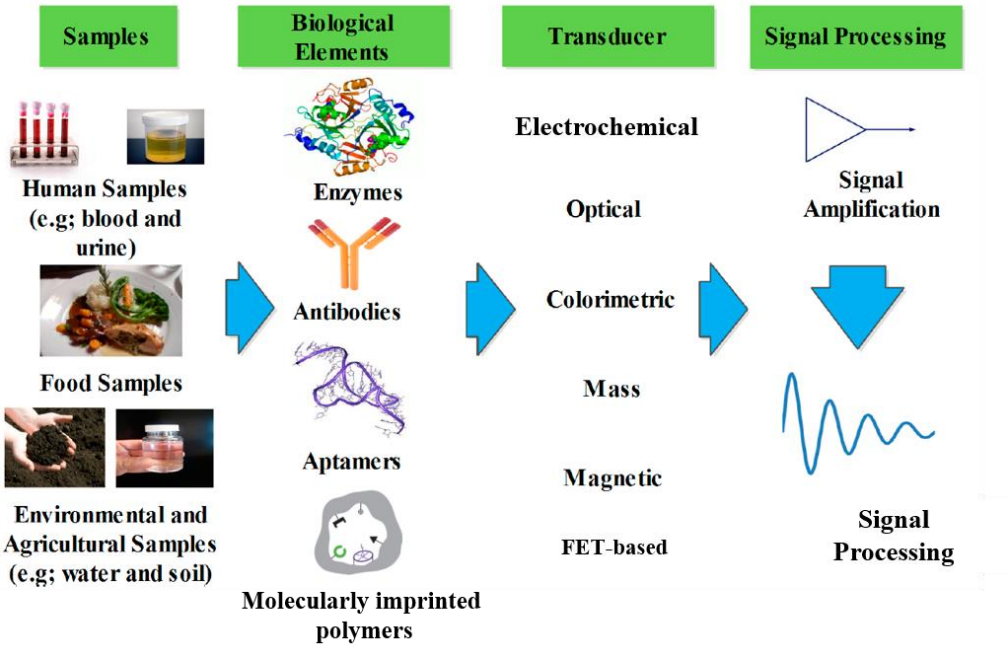

Figure 2.1. Schematic illustration showing different parts of a biosensor: (a) biorecognition elements, (b) transducers, and (d) data analysis system. Reproduced from [2].

There are several classes of bioreceptors with distinct structures that uniquely affect the biosensor performance. These numerous bioreceptors can be categorized into two main types -- natural and synthetic. *Natural* bioreceptors, such as antibodies and enzymes, are biologically derived constructs that take advantage of naturally evolved physiological interactions to achieve analyte specificity. On the other hand, *synthetic* bioreceptors, such as aptamers and molecularly imprinted polymers (MIPs) are artificially engineered structures developed to mimic physiologically defined interactions [3].

2.2. History and Evolution of Biosensors

The history of biosensors dates back to the 1950s, when Leland Clark Jr. invented the first and foremost electrochemical oxygen biosensor in 1956. Known as the Clark oxygen electrode, it consisted of a sliver/silver chloride reference electrode and a platinum cathode at which oxygen was reduced [4]. This oxygen electrode was later combined by Clark and Lyons with glucose oxidase incorporated in a dialysis membrane to measure the concentration of glucose in solution [5]. A couple of years later in 1967, Updike and Hicks described the first "enzyme electrode" for in vitro quantification of glucose in solution and in tissues. The electrode was engineered through immobilization of glucose oxidase in a polymerized gelatinous membrane that coated a polarographic oxygen electrode, thus serving as an enzyme transducer to catalyze an electrochemical reaction upon recognition of glucose [5].

Later in 1969, the first potentiometric enzyme electrode was developed by Guilbault and Montalvo to realize a urea sensor based on the immobilization of urease onto an ammonium-selective liquid membrane electrode [6]. Since then, a broad range of biosensors have been developed for in vitro and in vivo applications, whose nature ranges from enzymatic, to antibody, polypeptide, aptamer, or nucleic acids-based. Similarly, the evolution of a variety of transduction mechanisms has diversified the field of biosensors, ranging from electrochemical and electronic biosensors to thermic biosensors that measure the changes in temperature associated with the amount of heat generated by an enzyme-catalyzed reaction; microbial biosensors which integrate micro-organisms with a physical transducer, such as an electrochemical device, to monitor specific analytes or biomarkers typically through the production of electroactive metabolites; immunobiosensors based on recognition of target species by recombinant antibodies or antibody

fragments; optical biosensors, based on the differences in optical diffraction or changes in the emission of light signals upon target binding. The field is now a multidisciplinary area of research that bridges the principles of basic sciences (physics, chemistry, and biology) with fundamentals of micro/nanotechnology, electronics, and applicatory medicine [7], [8]. Figure 2.2 shows the timeline for biosensors development until 2010.

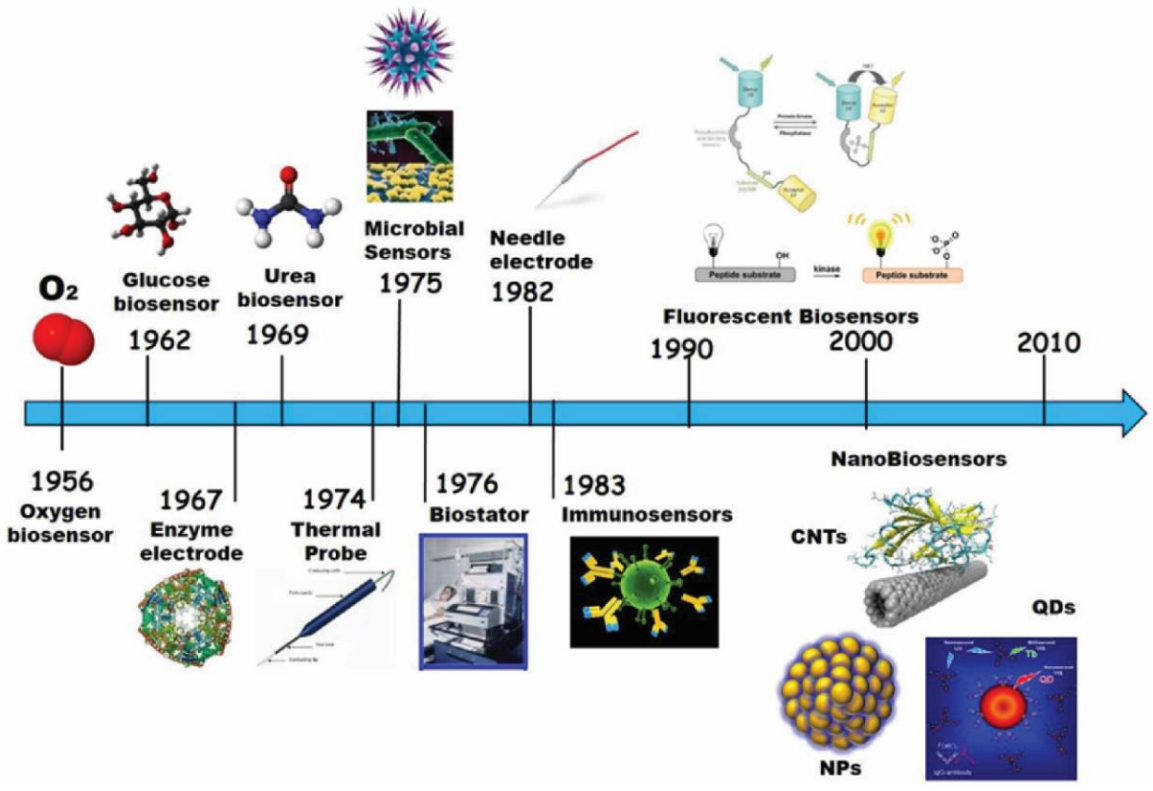

Figure 2.2. History and evolution of biosensors over time. Reproduced from [7].

2.3. Aptamers as Biorecognition Elements

Derived from the Latin word *aptus* meaning "to fit", aptamers are often used as one of the most trending biorecognition elements. First reported in 1990, aptamers recognize specific ligands and bind to various target molecules from small ions to large proteins with high affinity and specificity [9]. Aptamers are single-stranded oligonucleotides designed through a combinatorial selection process called Systematic Evolution of Ligands by Exponential Enrichment (SELEX). As shown in Figure 2.3, SELEX is an iterative process to search a library of randomly generated oligonucleotide sequences ($10^{15} – 10^{18}$) for strong binding affinities between the target analyte and oligonucleotide sequences, ensuring a selective and strong interaction pair. The cycle starts with

incubation of the target bioanalyte with an oligonucleotide library containing all potential aptamer sequences. Unbound aptamer sequences are washed away, and the bound aptamers are collected and go through polymerase chain reaction (PCR) amplification to regenerate the oligonucleotide library for the next SELEX round [3].

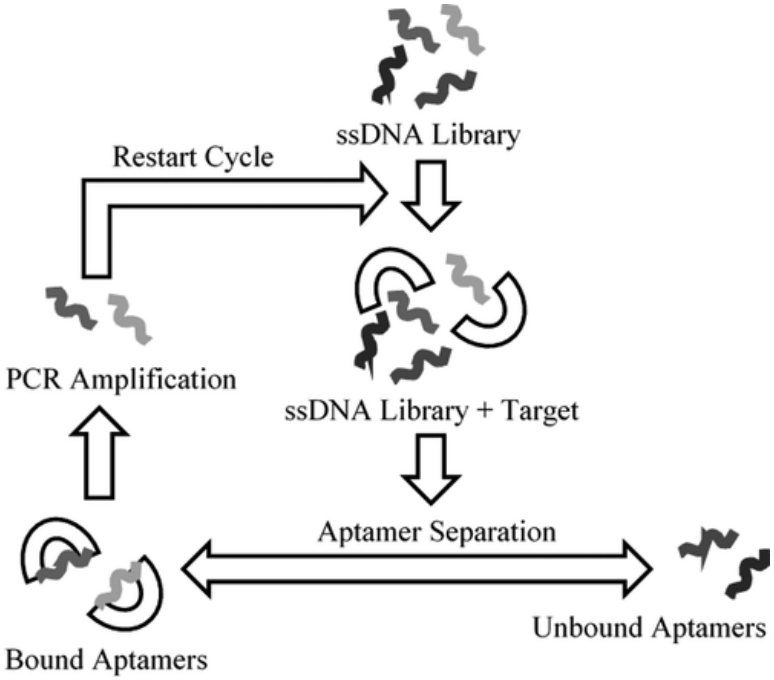

Figure 2.3. Schematic illustration of aptamer production by Systematic Evolution of Ligands by Exponential Enrichment (SELEX) process. Reproduced from [3].

Typically, around 30 – 100 nucleotides long aptamers possess high chemical stability, mass-producibility and reusability, longer shelf life, low production cost, small size and no batch-to-batch variations making them superior to their counterparts like antibodies, enzymes, proteins, etc. Moreover, aptamers undergo conformation change when they specifically interact with their targets, thus omitting the need for additional labeling process during monitoring of target binding events [10]. Due to these advantages, aptamers are often used as an integral part of biosensors leading to the creation of new research field called *aptasensors*. Due to their versatile potential applicability, aptamers are used for all our biosensors designed in this work.

2.4. Sensing of Protein Biomarkers

A biomarker is a biological characteristic that is objectively measured and evaluated as indicators of normal biological processes, pathogenic processes or pharmacological responses to a therapeutic intervention [11]. They can be used to determine disease onset, manifestation, progression, efficacy of drug treatment, and patient's susceptibility to develop a certain type of disease [12]. Among all biomarkers, proteins represent the most studied molecules because of (1) their direct association with the disease state [13] as well as (2) the availability of a large range of analytical instrumentation to identify and quantify proteins in complex biological samples, such as blood, saliva, etc. [14]. It is also possible to generate aptamers for almost every protein target, which make protein biomarkers a convenient target for aptamer-based biosensors. The high structural complexity of proteins allows them to bind with aptamer binding by stacking interactions, shape complementarity, electrostatic interactions, and hydrogen bonding. Moreover, in principle, proteins can present more than one binding site for aptamers, allowing the selection of a pair of aptamers binding to different regions of the target and enabling sandwich-assay based biosensors [15]. Hundreds of protein biomarkers have already been discovered for different diseases such as, cancer, Alzheimer's, AIDS, rheumatoid arthritis, malaria, tuberculosis, leprosy, sarcoidosis, Crohn's and cardiovascular diseases so far and researches are being done to discover more protein biomarkers, which is one of the goal of the research field *proteomics*.

2.5. Classification of Biosensors

As mentioned earlier, biosensors can be classified into different types depending on the detection principles they use. Figure 2.4 illustrates the four main types that will be discussed in this section.

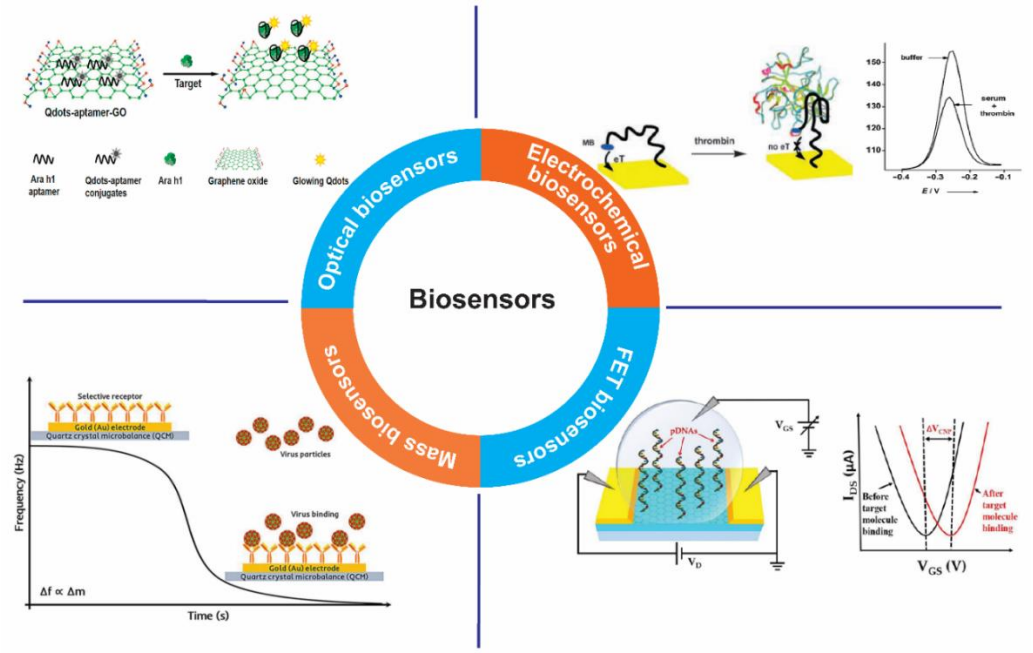

Figure 2.4. Schematic illustration showing the types of biosensors based on different detection principles.

2.5.1. Optical biosensor

Optical detection is one of the most commonly used popular detection principles because it offers multiple advantages, such as direct, real-time, and highly sensitive detection of many biological and chemical substances. Optical detection works by exploiting the interaction of the optical field with a biorecognition element to produce an electrical signal which is proportional to the concentration of the analyte. The signal can be either absorbance, fluorescence, chemiluminescence, colorimetry, interferometry, or surface plasmon resonance.

Among different optical detection mechanisms, fluorescence-based detection is by far the most widely used sensing technique. Fluorescence-based techniques work on the basis of the Förster resonance energy transfer (FRET) which involves the coupling of a fluorescent molecule that emits visible light (fluorophore) to another fluorescent molecule that absorbs visible light and emits at invisible wavelengths (quencher). Figure 2.5 shows the mechanism for FRET-based optical biosensor used by Weng and Neethirajan who utilized quantum dots-aptamer–GO complexes (QDs-aptamer-GO) as probes for sensitive detection of food allergens [16]. This device utilized quantum dots-aptamer–GO complexes (QDs-aptamer-GO) as probes that undergo conformational

change upon interaction with the food allergens. In the absence of the target analyte, the fluorescence of the QDs is quenched via FRET process between the QDs-aptamer probes and GO due to their self-assembly through specific π-π stacking interaction, resulting in no fluorescence signal. Upon binding with the target analyte, due to conformational change of the aptamers, QDs-aptamer probes are released from the GO leading to the recovery of fluorescence of QDs.

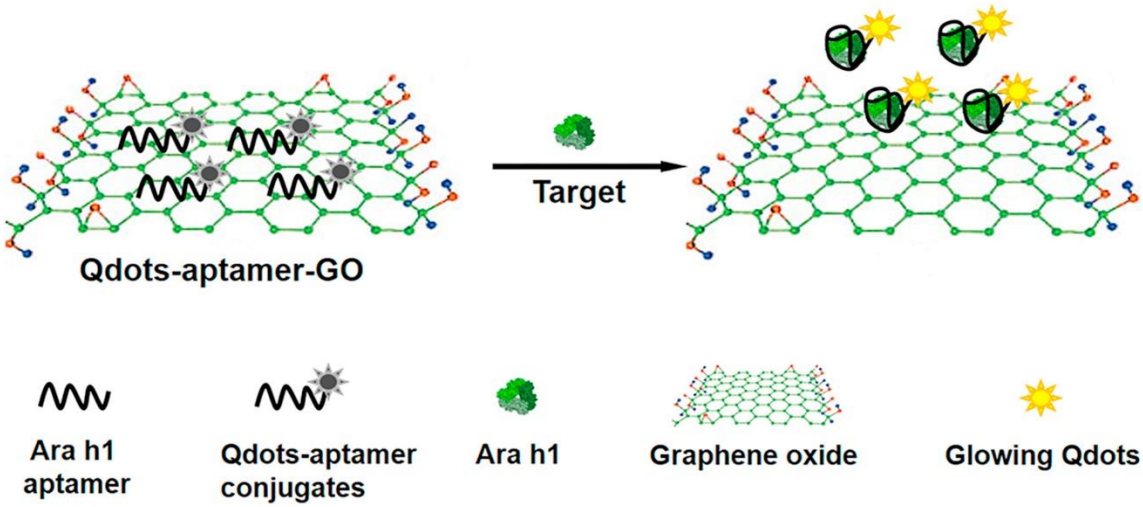

Figure 2.5. Schematic diagram showing the FRET-based sensing mechanism. Reprinted from [16].

Though optical biosensors exhibit high sensitivity, often they require labels such as methylene blue, fluorophore, etc. requiring complex chemistry for attaching the labels to the recognition elements. Also, optical biosensors are bulky, and require sophisticated laboratory setup along with trained technicians, thus increasing the overall cost of the sensor setup.

2.5.2. Electrochemical biosensor

Electrochemical biosensors provide an attractive means to analyze the content of a biological sample due to the conversion of a biological event to an electrical signal. For example, the reaction under investigation generates a measurable current (amperometric/voltammetric), a measurable potential or charge accumulation (potentiometric), or alters the electrical conductivity between electrodes. Electrochemical impedance spectroscopy (EIS), or impedimetric sensing, is also a commonly used technique where a biological or chemical event causes a change in the impedance (both resistance and reactance) at the liquid-electrode interface [17].

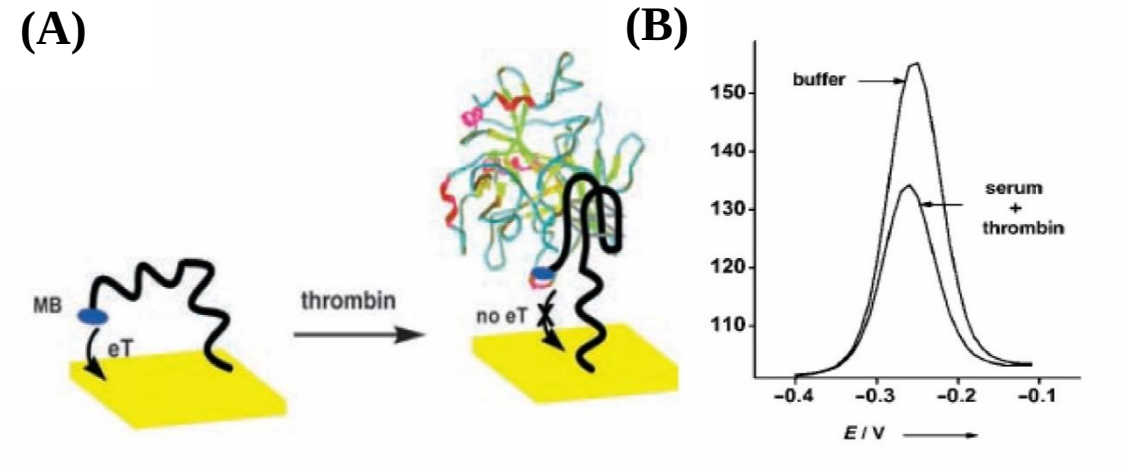

Figure 2.6. Electrochemical biosensor: (A) target-induced conformation change of aptamer; and (B) voltammogram as the sensor responds to 64 nM thrombin in 50% blood serum. Adapted from [18].

Amperometric detection is the first electrochemical technique adopted in microscale [19]. Amperometric biosensors are those devices that transduce the biological recognition events caused by the oxidation or reduction of an electroactive biological species at the sensing surface into an electrical signal for the quantification of an analyte within a sample matrix. The intrinsic simplicity of the transducer lends itself to low-cost portable devices for applications ranging from disease diagnosis to environmental monitoring [20]. On the other hand, a voltammetric sensing is a technique where the electrical potential at the working electrode is scanned from one preset value to another, and the cell current is recorded as a function of the applied potential [21]. One of the pioneers of electrochemical biosensor is Professor Kevin Plaxco from the University of California, Santa Barbara (UCSB) who exploited the target-induced conformation change of aptamers to develop an aptasensor for sensitive detection of thrombin [18] as schematically illustrated in Figure 2.6.

Unlike amperometric technique, this voltametric technique monitors the redox activity across a range of applied potentials manifesting well-defined current peaks [22]. Voltammetry has been practiced for a long time and has revolutionized analytical chemistry. The main advantages of using voltametric methods over spectroscopy or chromatography include their high sensitivity,

precision, accuracy and cost effectiveness. In the past, voltametric techniques were difficult to apply without computer controlled potential scan and were not nearly as useful as they are today. However, in present days, these techniques are largely available due to the advent of computers and their key role in the control and measurement of the potentials and currents of potentiostats [21].

Another popular electrochemical detection mechanism is the label-free impedimetric technique which works by measuring the impedance of the electrode/electrolyte interface over a wide range of frequencies. The resulting spectrum is called the electrochemical impedance spectrum (EIS) that can be used to monitor the changes in the electrical properties of the biosensor at different stages, including different fabrication steps as well as the detection of target recognition events. It offers several unique advantages that include the ease of signal quantification, the ability to separate the surface binding events from the solution impedance, non-invasive measurement, real-time monitoring, and label-free detection, making it an effective tool for electrochemical interrogation [23]. EIS can analyze both the resistive and capacitive properties of the electrode surface upon excitation/perturbation of the system at equilibrium by a small amplitude sinusoidal excitation signal [24]. One of the common representation of the EIS is the Nyquist plot (Figure 2.7A), that can be modeled by the Randles circuit as seen in Figure 2.7B. It consists of a solution resistance (R_S), a double-layer capacitance (C_{dl}), a charge transfer resistance (R_{ct}), and the Warburg impedance (Z_W). R_S is inserted as a series element because all the current passes through the uncompensated solution, while the parallel elements are introduced because the total current through the electrode is the sum of distinct contribution from the Faradic process and the double-layer capacitance charging.

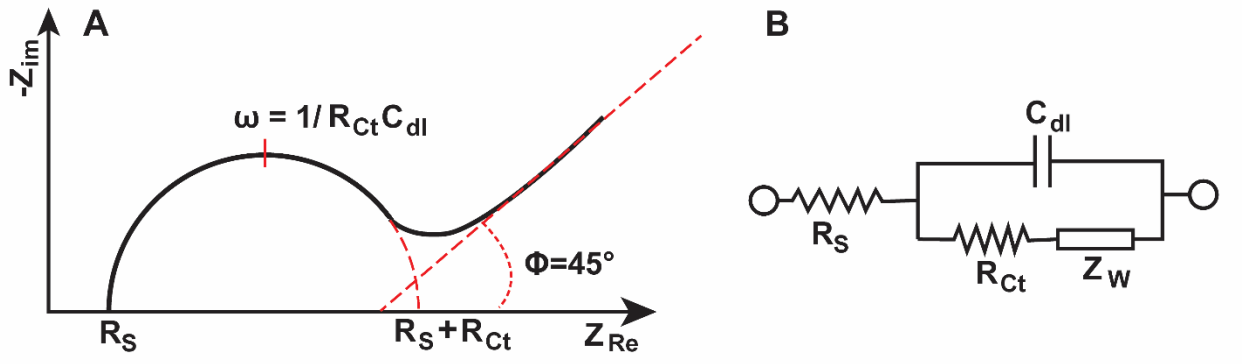

Figure 2.7. The Nyquist plot (A); and the corresponding Randles circuit (B).

C_{dl} and R_{ct} are often used as the detection parameters in biosensing as they represent the dielectric and insulating features at the electrode/electrolyte interface, while R_S and Z_W depend on the bulk properties of the electrolyte and the diffusion of the redox probe, respectively [25]. For example, Chen et al. employed the change of R_{ct} to implement a label-free impedimetric biosensor for highly sensitive detection of lysozyme protein [26]. Lysozyme binding aptamer was modified on a gold

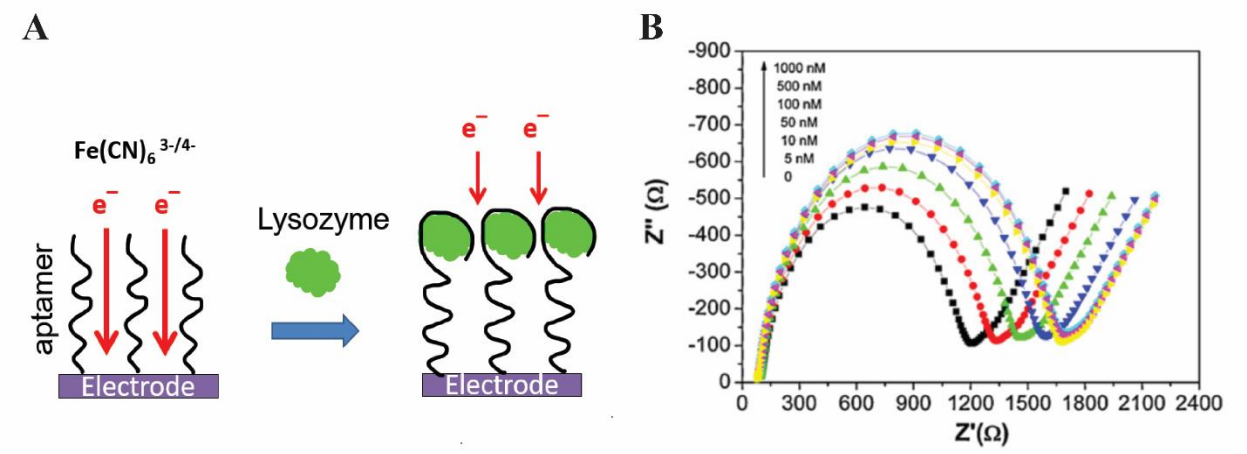

Figure 2.8. Label-free impedimetric biosensors based on electrochemical impedance spectroscopy: (A) working principle; and (B) EIS measurements for different concentrations of lysozyme.

electrode and EIS measurements were performed in $[Fe(CN)_6]^{4-/3-}$ redox couple. As seen in Figure 2.8A, binding of lysozyme to aptamer blocks the path for charge transfer from the redox couple to the electrode, effectively increasing the charge transfer resistance R_{ct} which is reflected in Figure 2.8B. Due to the huge promise EIS offers, we have designed and implemented an impedimetric biosensor for selective detection of lysozyme protein that is presented in Chapter 3.

2.5.3. Field-effect transistor biosensor

Field-effect transistors (FETs) have attracted much attention in the biosensing community as they offer many advantages such as ease of miniaturization, low-cost, large-scale integration capability with the existing manufacturing process as well as label-free, rapid, and highly sensitive detection of analytes [27]. A typical FET biosensor is composed of a semiconducting channel that connects the source and the drain electrodes. Upon adsorption of the biomolecules on the channel surface, a change in the electric field occurs which affects the gate potential of the device resulting in a change in the charge carrier density within the channel of the FET. Such change in the drain current

can be conveniently measured and be utilized as an interrogation strategy to probe the adsorbed biomolecules.

This type of sensing mechanism has been demonstrated in the past for detecting target analytes in various media including gases, aqueous liquid, as well as in human serum [27]–[32]. For example,

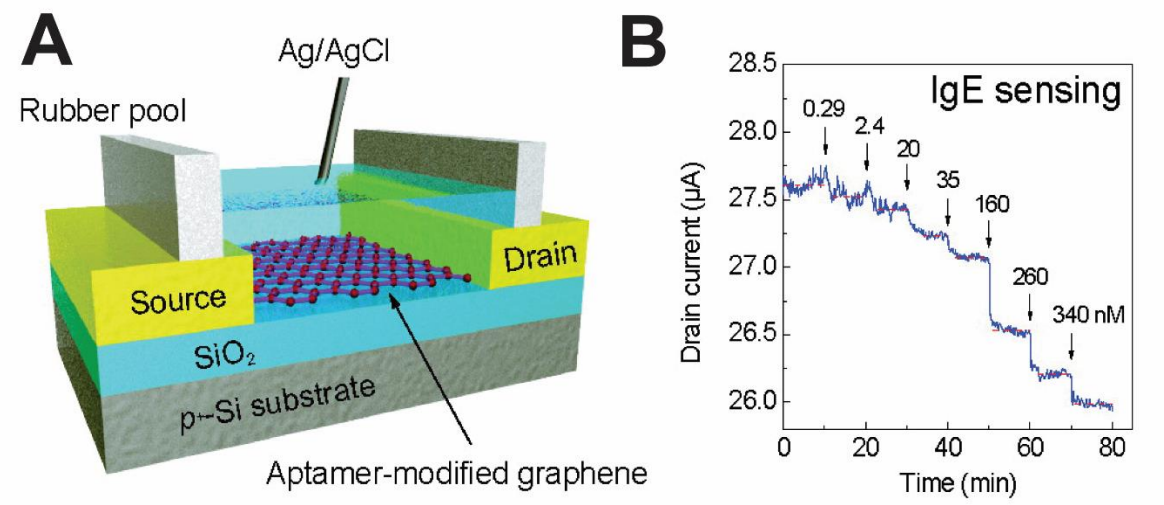

Figure 2.9. Schematic representation of the working principle of FET biosensor: (A) Device structure of the electrolyte-gated graphene FET biosensor. (B) Time course of I_D for the biosensor. At 10-min intervals, various concentrations of IgE were injected. Reproduced from [32].

Ohno et al. demonstrated a label-free immunosensing of IgE protein using an aptamer-modified graphene FETs (Figure 12A) [32]. The aptamer-modified graphene FETs showed selective electrical detection of IgE protein. From the dependence of the drain current variation on the IgE concentration, they also estimated the dissociation to be 47 nM, indicating good affinity (Figure 2.9).

2.5.4. Mass sensitive biosensor

Gravimetric or mass sensitive biosensors work on the basic principle of measuring the change in the mass at the sensing surface caused by the binding of the analyte to the receptors. Most mass sensitive biosensors use piezoelectric quartz crystals which can be either in the form of resonating crystals (such as quartz crystal microbalance, QCM) or surface acoustic wave (SAW) devices [33]. The QCM biosensors have been very popular in the area of rapid detection of pathogens [34] and

toxins [35] because of their multifarious advantages such as ease of use, shorter analysis time, low-cost, as well as the possibility of label-free and real-time detection. On the other hand, SAW-based biosensors can detect acoustic waves generated by the interdigital transducers (IDTs) which are periodic metallic bars deposited on a piezoelectric material. Upon recognition of an analyte by the immobilized receptors, the velocity of the SAW changes that produces signal by the driving electronics. Figure 2.10 shows the operating principle of a QCM-based mass sensitive biosensor

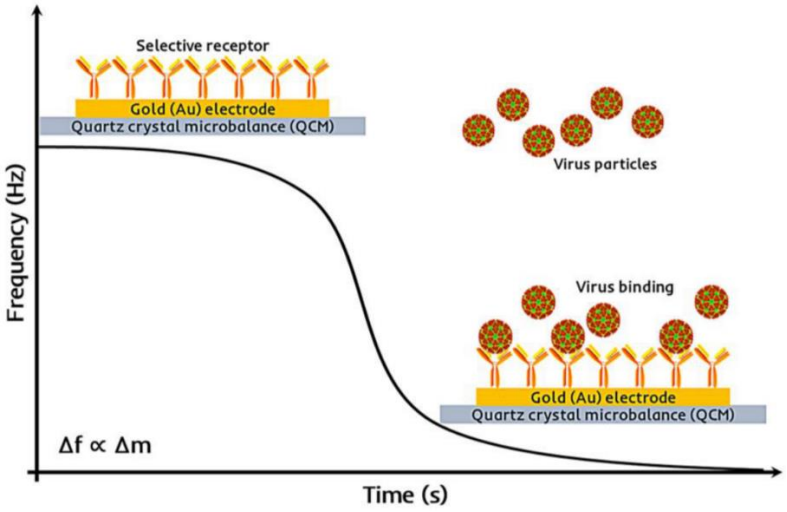

Figure 2.10. Operating principle of a QCM-based mass sensitive biosensor. When any analyte binds to the selective receptor, a change in the mass loading occurs that can be detected by a change in the frequency. Reproduced from [36].

for virus recognition. The change in mass in response to virus binding with the selective receptor is detected as a change in frequency of QCM transducer.

2.6. Summary

The following table (Table 2.1) summarizes the advantages and disadvantages of the four detection techniques described above.

Table 2.1. Advantages and disadvantages of different detection techniques [33].

Types of biosensor	Advantages	Disadvantages

Optical	High sensitivity, remote controllable	Often requires labels, costly, fragile, and bulky setup
Electrochemical	Good resolution, excellent accuracy, repeatability	Susceptible to temperature changing, short shelf-life
FET based	Highly sensitive, faster response, mass producible, label-free	Not suitable for receptors longer than the Debye length
Mass sensitive	Highly sensitive, suitable for target molecules that don't have electrically conducting property or optical signal (e.g. virus)	Fragile and mechanically unstable

In this thesis, we developed two types of biosensors, namely the impedimetric and the GFET-based, for selective detection of protein biomarkers.

2.7. Conclusion

In this chapter, I describe the basics of biosensors—definition, working principle, history, and evolution. A brief introduction of aptamers as recognition elements and proteins as target biomarkers is also presented. In addition, I present different types of biosensors, namely optical biosensor, electrochemical biosensor, field-effect transistor biosensor, and mass sensitive biosensor. In particular, their working principle, state-of-the-art development as well as the challenges are delineated. Finally, their comparative advantages and disadvantages are summarized in table.

CHAPTER 3: CARBON-BASED NANOTECHNOLOGY FOR BIOSENSING

3.1. Introduction

Modern technology is characterized by its emphasis on miniaturization, a trend to manufacture ever smaller mechanical, optical and electronic products and devices. For example, in the IC industry, remarkable technological progress has occurred in terms of reductions in the size of transistors, thus increasing the number of transistors per chip. This trend, which is known as the Moore's law (Figure 3.1), states that the number of transistors in an IC doubles about every two years [37]. This trend of miniaturization has evolved in time and taken us to the nanometric regime, leading to the term "nanoelectronics". Essentially, nanoelectronics is the application of

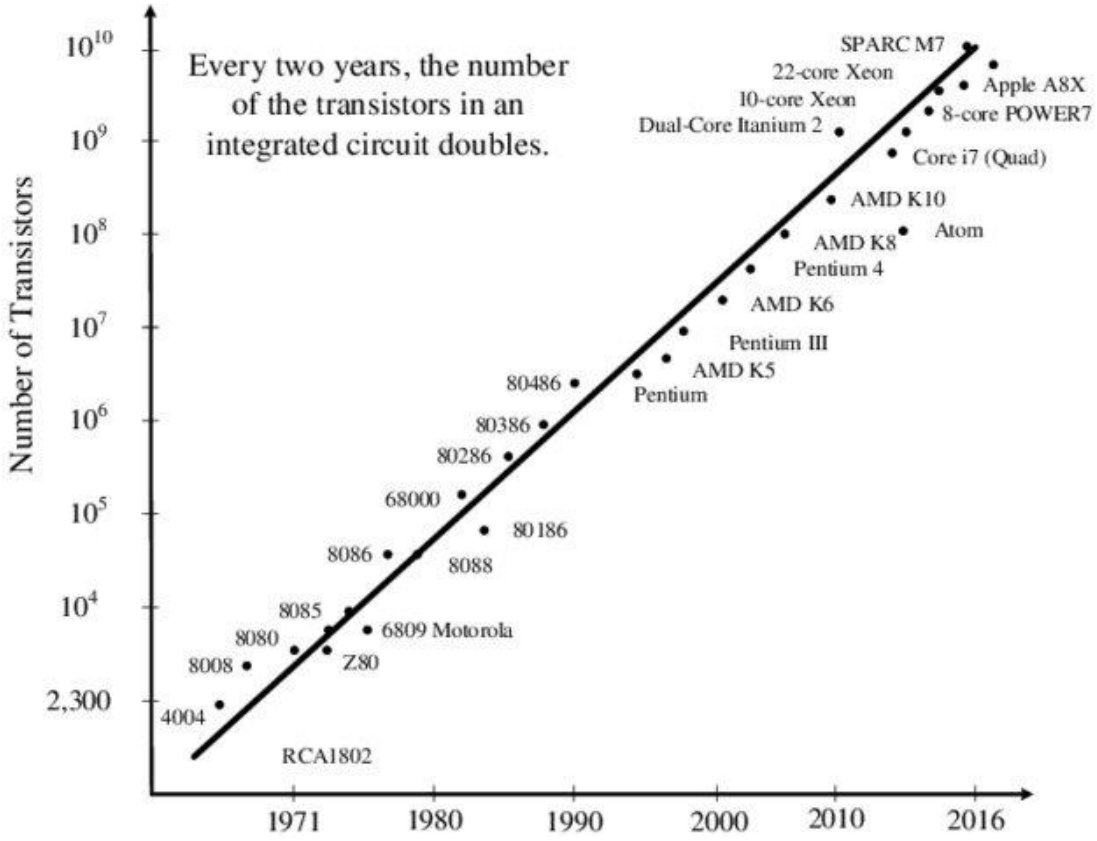

Figure 3.1. The number of transistors in the CPU as a function of time. The trend shows a doubling approximately every two years which is known as the Moore's law. Reproduced from [37].

nanotechnology[1] for electronic components and aims at improving the capabilities of electronics such as display, size, and power consumption of the device for everyday use [38]. It is based on the quantum mechanical properties of the hybrid material, semiconductor, one dimensional (1D) materials such as nanotubes, 2D materials such as graphene, and so forth. The integration of nanoelectronics and nanoelectronic devices with biosensors leading to the term *nanobiosensors* has become very popular due to different advantages it offers to the sensor. These advantages are achieved by using different nanomaterials as the biosensing interface and nanodevices as the transducers.

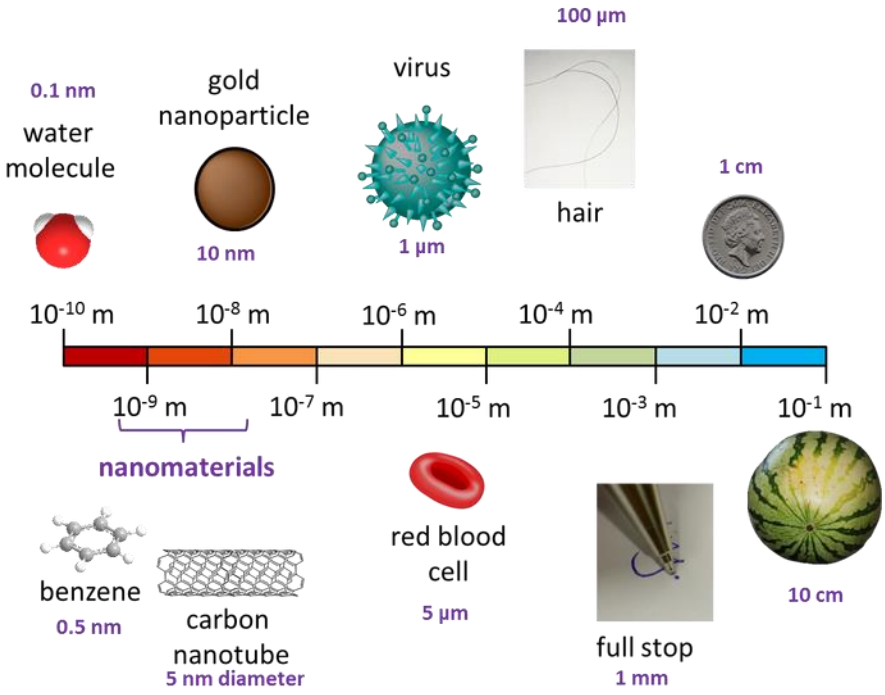

Figure 3.2. Nanoscale showing the dimension range for nanomaterials. Reproduced from [39].

Nanomaterials are materials with minimum one dimension in the nanoscale (Figure 3.2). In this scale, nanomaterials possess unique properties that play significant role in the development of

[1] According to the National Nanotechnology Initiative (NNI), nanotechnology is the understanding and control of matter at dimensions between approximately 1 and 100 nm, where unique phenomena enable novel applications.

biosensors. This significance arises from the fact that nanomaterials can help address some key issues in designing biosensors. Such issues include: (1) design of the biosensing interface so that the analyte selectively interacts with the biosensing surface; (2) achievement of efficient transduction of the biorecognition event; (3) increase in the sensitivity and selectivity of the biosensors; and (4) improvement of response times in highly sensitive systems [40]. More specifically, nanomaterials make biosensors compatible with biological matrices so that they can be used in complex biological samples or even in vivo; enable fabrication of viable biosensors that operate within confined environments such as inside cells; and simultaneous detection of multiple biosensors in one device. Nanomaterials can be classified as zero-, one-, and two -dimensional systems. This includes semiconductor quantum dots, metallic nanoparticles, metallic or semiconductor nanowires or nanotubes, nanostructured conductive polymers or nanocomposites, mesoporous materials, etc. Among them carbon-based nanostructures are the most popular because of their low-cost, wide-availability, potential biocompatibility, etc.

The electronic configuration of carbon in ground state is $1s^2 2s^2 2p^2$. But in excited state, carbon can exist in three different states corresponding to sp^3-, sp^2-, and sp- hybridization of their valence orbitals leading to the formation of different carbon allotropes. These allotropes enable the formation of different types of carbon nanomaterials such as CNTs, graphene, carbon dots, carbon nanofibers, nanodiamonds, and buckminsterfullerene as seen in Figure 3.3. The following section will discuss the fundamentals of carbon nanoelectronics with respect to carbon nanotubes and graphene.

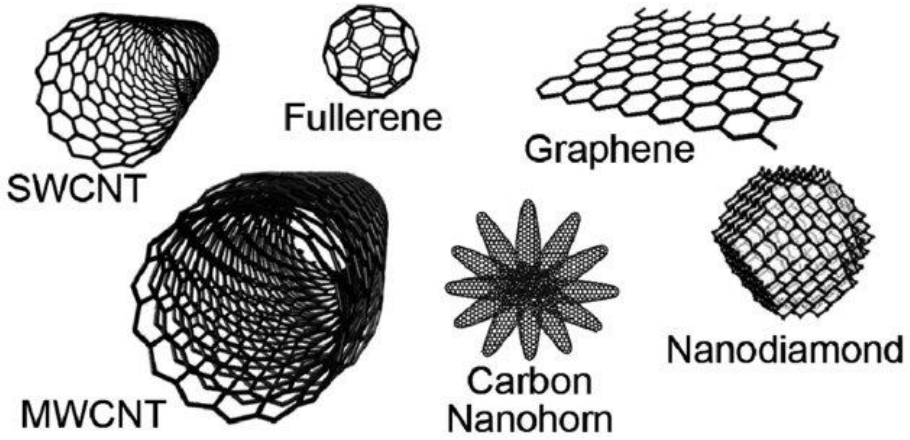

Figure 3.3. Various forms of carbon nanostructures. Reproduced from [41].

3.2. Carbon Nanoelectronics

The field of carbon nanoelectronics has grown significantly with rapid developments in device performances and high yield assembly of single-walled carbon nanotubes (SWCNT) and graphene-based devices. Such a rapid growth is largely fueled by the unique single-atomic layer honey-comb structure of these carbon allotropes, that leads to many extraordinary physical properties such as extremely high electron and hole mobilities (potentially in excess of 100,000 $cm^2/V/s$), extremely high strength (greater than steel), along with other extreme properties [42], [43]. In this section, the electronics of these carbon nanomaterials, CNTs and graphene in particular, will be discussed.

3.2.1. Carbon nanotubes (CNTs)

To date, arguably the most widely studied one-dimensional (1D) material in nanoelectronics is the carbon nanotube. CNTs are well-ordered, graphitic sheet rolled up into a hollow cylinder of sp^2-hybridized carbon atoms [40]. They can be classified into two categories – single-walled carbon nanotubes (SWCNTs) and multi-walled carbon nanotubes (MWCNTs). Though SWCNTs and MWCNTs are similar in certain aspects, they have some striking differences. Structurally, SWCNTs are single sheets of graphene rolled into cylinders, MWCNTs are composed of several concentric tubes (approx. 6 – 25) that share the same longitudinal axis. As 1D carbon allotropes, CNTs have lengths that can range from several hundred nanometers to several millimeters, but their diameter depends on their types: for MWCNTs, the outer diameter is typically 30 – 50 nm and for SWCNTs, it is typically 0.7 – 2.0 nm [44].

Among different electronic properties, the conductivity of the CNTs is especially critical for their role as nanomaterials in electrochemistry. While MWCNTs are regarded as metallic—a highly attractive property for an electrode, the electronic properties of SWCNTs are controlled by the chiral vector, that connects the centers of two hexagons. The chiral vector is given by $C = na_1 + ma_2$ (Figure 3.4), where a_1 and a_2 are the unit vectors of the graphene lattice, and the pair of integers (*n, m*) is called the chiral index or just chirality. Depending on the chirality, SWCNTs can be either metallic if (*n-m*) is multiple of 3; or semiconducting otherwise [40]. Thus, with small diameter SWCNTs approximately two-thirds are semiconducting, and one-third are metallic. However, as the diameter of the tubes increases, the bad gap tends to zero resulting in zero band-

gap semiconductor. Therefore, the varieties of conductivities in a mixture of SWCNTs can complicate their applications in electrochemistry compared to MWCNTs.

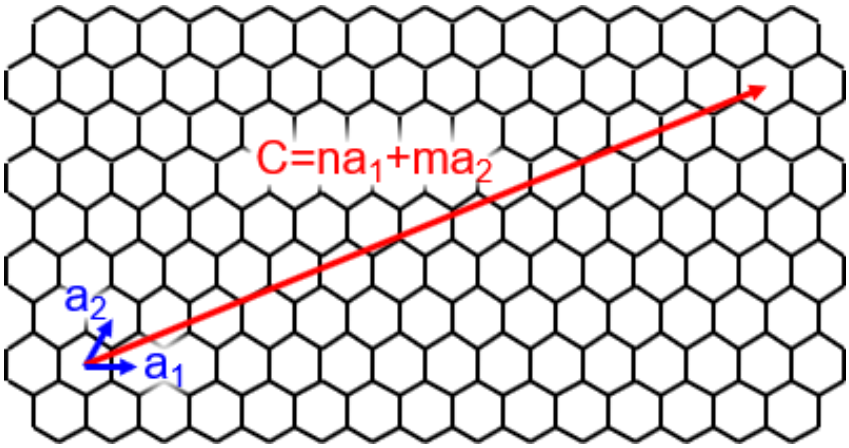

Figure 3.4. Chirality in SWCNTs. A chiral vector C can be defined by a chiral index (n, m) using the basis vectors a1 and a2 of a graphene sheet. Reproduced from [45].

CNTs can be produced by different methods such as chemical vapor deposition (CVD), laser ablation and arc discharge [46]. The resulting product not only contains the CNTs, but also contains the catalyst particles and amorphous carbons as impurities. In addition, the CNTs are not identical in length and chirality. This is one reason why the large-scale manufacturing of identical CNT devices still remains a challenge [47].

Electrochemically, CNTs are not very reactive due to their highly graphitized nature. But there is evidence that favorable electrochemical properties of SWCNTs can be achieved from oxygenated carbon species, especially carboxyl moieties that are produced on the tips of the nanotubes during acid purification [48], [49]. This is in contrast to the MWCNTs that experience slow rate of heterogeneous electron transfer if functionalized with oxygen-containing groups [50], [51]. According to Pumera et al., the oxygen-containing groups in fact play a minor role in the heterogeneous electron transfer for electrochemically activated MWCNTs [52]. Rather, they suggest that the increased heterogeneous electron transfer is due to an increase of the density of edge-like sites on the sidewalls of the tubes.

The electrochemical behavior of CNTs was explored by several groups to design and implement aptamer-based biosensors [53], [54]. For example, Rohrbach et al. have implemented a label-free impedimetric aptasensor for selective detection of lysozyme using MWCNTs [54]. The working electrode was modified with MWCNTs which was deposited by simple pipetting of carboxylated (5%) MWCNT suspension. In the following step, aminated anti-lysozyme aptamers were immobilized on the working electrode via the covalent linkage between the carboxylic groups of the nanotubes and the amino groups of the aptamers (Figure 3.5A). When any lysozyme binding occurs, the net positive charge of the aptamer-lysozyme interaction enhances the charge transfer from the redox couple to the working electrode, thereby decreasing the charge-transfer resistance, R_{ct} (Figure 3.5B). By monitoring the change in R_{ct}, they were able to detect lysozyme with a detection limit of 862 nM.

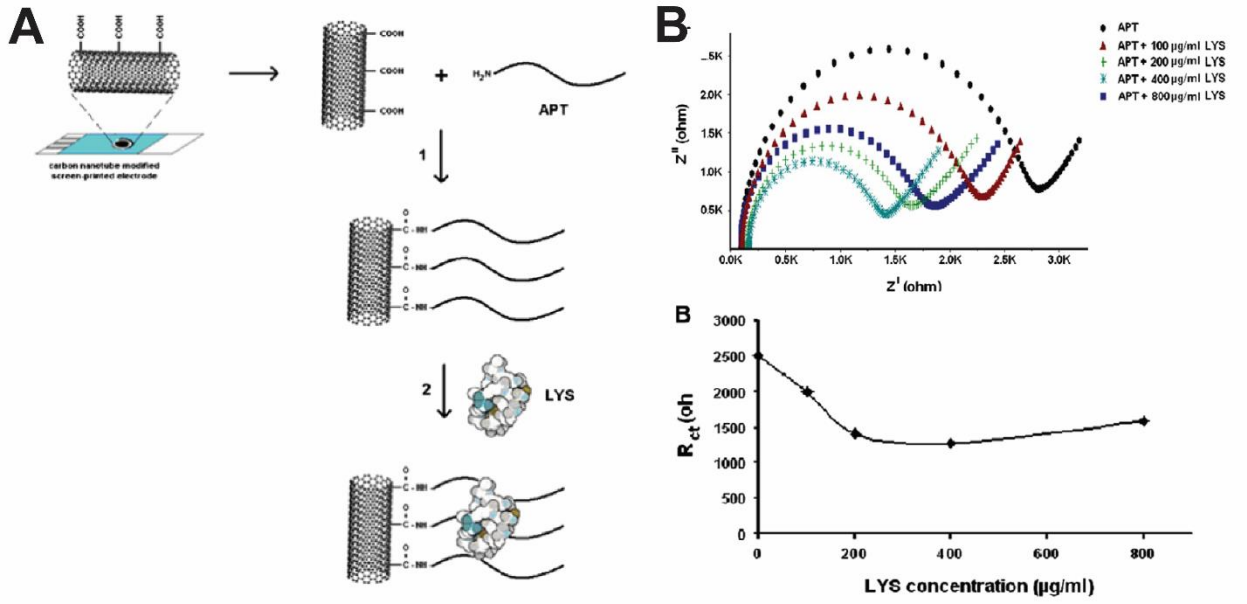

Figure 3.5. Impedimetric biosensor for label-free detection of lysozyme using MWCNTs: (A) modification of the working electrode with MWCNTs; and (B) electrochemical impedance spectroscopy measurements for different concentrations of lysozyme and the corresponding calibration curve. Reproduced from [54].

The sidewalls of the nanotubes being very hydrophobic, dispersion and manipulation of CNTs in common solvents for controlled modification of electrode surface presents a major challenge.

Moreover, their tendency to aggregate and form clusters owing to high van-der-Waals force between the tubes limit their dispersibility in aqueous or polar solvents [48], [55]. As a consequence, dispersing tubes is usually performed in non-polar organic solvents such as dimethyl formamide (DMF), N-Methyl-2-pyrrolidone (NMP), tetrahydrofuran (THF) or with the aid of surfactants, polymers such as nucleic acids or oxygenated functional groups such as carboxylic acids [48], [53], [56]. Figure 3.6 illustrates the nucleic acid-assisted dispersion of CNTs where single-stranded DNA (ssDNA) helically wraps the CNT using the $\pi - \pi$ stacking internactions between the nucleotide base of the ssDNA and the CNT sidewall, thus converting it into a water-soluble object [57]. Several research groups have used this nucleic acid-assisted dispersion of CNTs to implement nucleic acid aptamer-based biosensors [58], [59]. For example, Lian et al. has developed a piezoelectric aptamer biosensor on interdigital electrode (IDE) for selective detection of lysozyme protein [59]. The IDE was modified with aptamer-wrapped-SWCNTs which was connected to the oscillator circuit in series with the piezoelectric quartz crystal (SPQC). In the presence of target lysozyme, the SWCNTs, being substituted by the lysozyme with greater affinity towards the aptamer than the SWCNTs, came off from the IDE surface causing a frequency change of the SPQC-IDE.

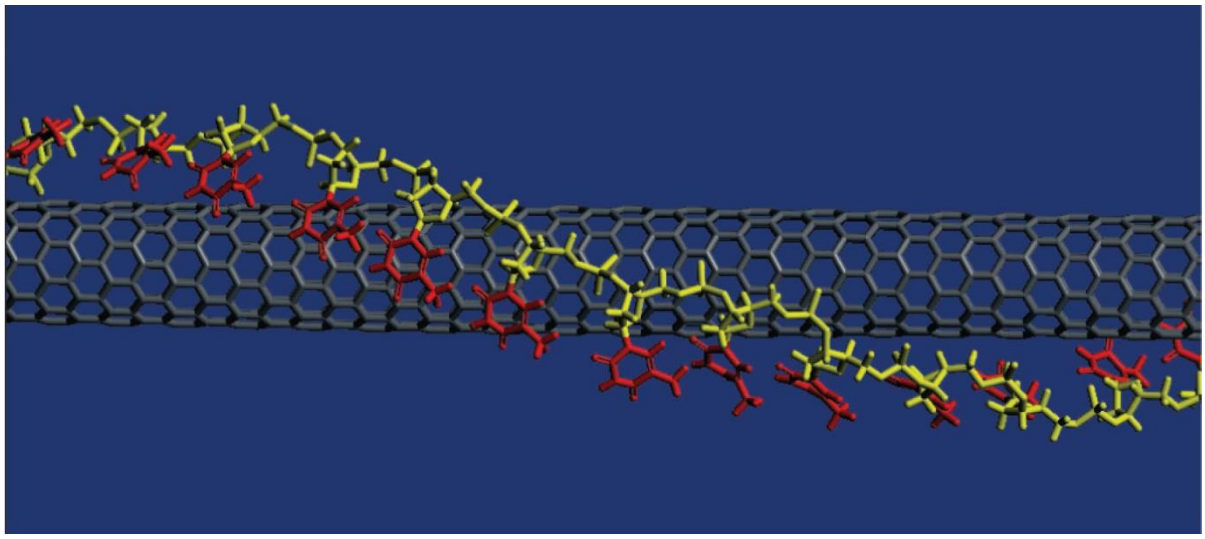

Figure 3.6. Nucleic acid-assisted dispersion of CNT where DNA wraps the CNT helically making it water-soluble. Reproduced from [57].

There are several deposition methods of carbon nanotubes experimented by many groups, such as the dip coating [60], spray coating [61]–[63], electrophoretic deposition [64], printing [65]–[68] and others. Among them, printing is one of the prominent methods of interest today. Specially, inkjet-printing offers several unique advantages such as low cost, rapid printing, easy formation of microarrays, automation, easy patterning control and mass-producibility [56]. Inkjet-printing is currently being used to deposit various types of conductive nanomaterials such as gold and silver. Although these metals are excellent conductors, carbon nanotube-based inks are becoming very popular because of their lower cost and more versatile properties in the sense that they can behave both as a semiconductor and a conductor. In this thesis, the possibility of employing inkjet-printing of CNTs was explored for implementing electrochemical detection of protein biomarkers. Aptamers are used as the receptors that simultaneous act as one the dispersing agents for the CNTs for preparing the ink for the ink-jet printer.

3.2.2. Graphene

Known as the world's first 2D material, graphene has revolutionized the field of biosensing due to its many advantages that make it compatible with biosensing platforms. It was first isolated and characterized in 2004 by two researchers: Andre Geim and Kostia Novoselov of the University of Manchester, bringing them the Nobel prize in physics in 2010 [69]. With a thickness of single atomic layer, graphene is isolated from graphite that can be considered as a stacked pile of multiple graphene layers held together by van-der-Waals forces. It is the thinnest known material with a thickness of 0.35 nm and is composed of sp^2 -bonded carbon atoms arranged in hexagonal network [70]. Though incredibly flexible, it is the strongest ever measured material that demonstrates excellent conductivity to electricity (better conductivity than copper) and shows unique morphological properties.

Graphene can be produced by different methods such as mechanical exfoliation, chemical vapor deposition (CVD), etc. The first demonstrated process used by Geim and Novoselov to derive graphene was exfoliation of graphite by using a simple scotch tape technique [71]. While mechanical exfoliation is a reliable method for producing high quality defect free graphene, it produces only a few micrometer-sized sheet and the process being time consuming, not suitable for large scale production. By contrast, chemical vapor deposition is a cost and time effective

method of producing high quality graphene in large scale. A typical CVD process for graphene is performed under vacuum and uses heated substrate to break apart the atoms in a gaseous hydrocarbon such as methane. The remaining carbon atoms then align themselves atop the substrate in the distinctive hexagonal structure of graphene. The graphene film can then be transferred to the desired substrate through various techniques. A disadvantage of the CVD process is that the growth and transfer process can produce defects in the graphene lattice. Perfecting the CVD process is an ongoing goal and is necessary for the commercialization of the many useful applications of graphene.

In the past decades, graphene has been experiencing unparalleled usage in the material world and has recently gained significant attention in the field of electrochemical and FET sensors thanks to its ability to be integrated with different nanomaterials, such as metals, metal oxides, and quantum dots [72], [73]. The biocompatibility of graphene in biosensing generates from the combination of its versatile properties, such as, enhanced specific surface area, electrical conductivity, chemical stability, ease of manipulation, integration-capabilities with different nanomaterials, high sensitivity to biomolecules as well as good adsorption capability [70]. The theoretical specific surface area of graphene is 2630 m^2/g [74] which is approximately twice the specific surface area of CNT that ranges from 50 – 1315 m^2/g [75]. With such excellent physical properties, graphene can even achieve the detection of single molecule making it a promising candidate for biosensing. Another property that makes graphene suitable for biosensing is its ease of functionalization. Graphene surface can easily be modified with a variety of chemical groups or biomolecules, thanks to its hydrophobicity in nature and the tendency to form agglomerates in most of the solvents due to van-der-Waals forces [70].

Many of the graphene's excellent electronic properties originate from its unique band structure that exhibits the degeneration of the valence and conduction band at the Dirac point. The degeneration at the Dirac point indicates that graphene has a zero bandgap that can be modulated by physical or chemical surface modifications. Also in the hexagonal honeycomb lattice, each carbon atom with its three sp^2-hybridized planar orbitals forms a strong sigma bond (Figure 3.7) with three neighboring carbon atoms resulting in a strong graphene structure that offers the longest 'mean free path' on the order of several microns among any known nanomaterial

[70], [76]. On the other hand, the delocalized electrons in the π bonds above and below the basal plane contributes to the high electrical conductivities and mobilities: the room-temperature mobility has been measured at 15,000 $cm^2V^{-1}s^{-1}$ while a clean, suspended single layer graphene has achieved 230,000 $cm^2V^{-1}s^{-1}$ at temperatures near absolute zero. This high carrier mobility makes graphene a suitable candidate for biosensing with excellent sensitivity as even a single biomolecule that comes into contact with its surface can module these properties either by *n*- or *p*-type doping, surface charge induced gating or by Shottkey-barrier modification [40], [70].

As a transducer material, graphene has been investigated by many research groups. For example, Lu et al. have implemented a sensing platform for selective detection of DNA and proteins using graphene oxide [77]. Chang et al. have developed a graphene-based fluorescence resonance energy transfer (FRET) biosensor for sensitive detection of thrombin with a detection limit as low as 31.3 pM which is two orders of magnitude lower than CNT based fluorescence sensors [78]. Others have incorporated graphene into a field-effect transistors (FETs) for detection of various target analytes including antigens, antibodies, and charged molecules [32], [79]–[83].

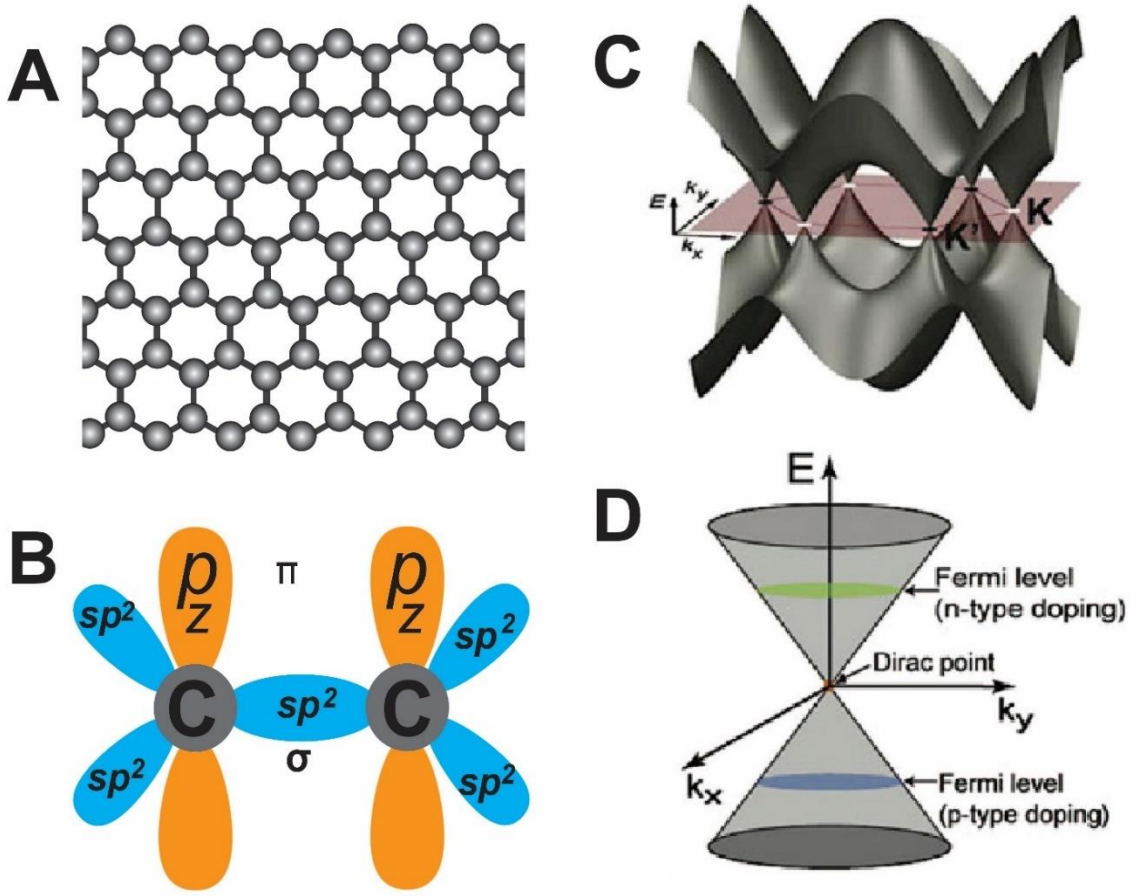

Figure 3.7. Electronic properties of graphene: (A) lattice structure; (B) sp^2 hybridization; (C) 3D band structure; and (D) the approximation of the low-energy band-structure as two cones touching at a single point called Dirac point (bottom). Adapted from [70].

3.2.2.1. Graphene FET (GFET) as an emerging nanoelectronic device

A field-effect transistor (FET) is an electronic device which is capable of modulating the current through a semiconducting channel by the application of an electric field. In a GFET, graphene is used as the semiconducting channel between two metal electrodes: source and the drain that lie atop an electrical insulator such as SiO_2 (Figure 3.8A). Whenever any charged molecule comes in contact with the graphene film, it causes a measurable change in the channel conductance leading to a change in the drain-source current, which can be used as a readout signal for the sensing mechanism.

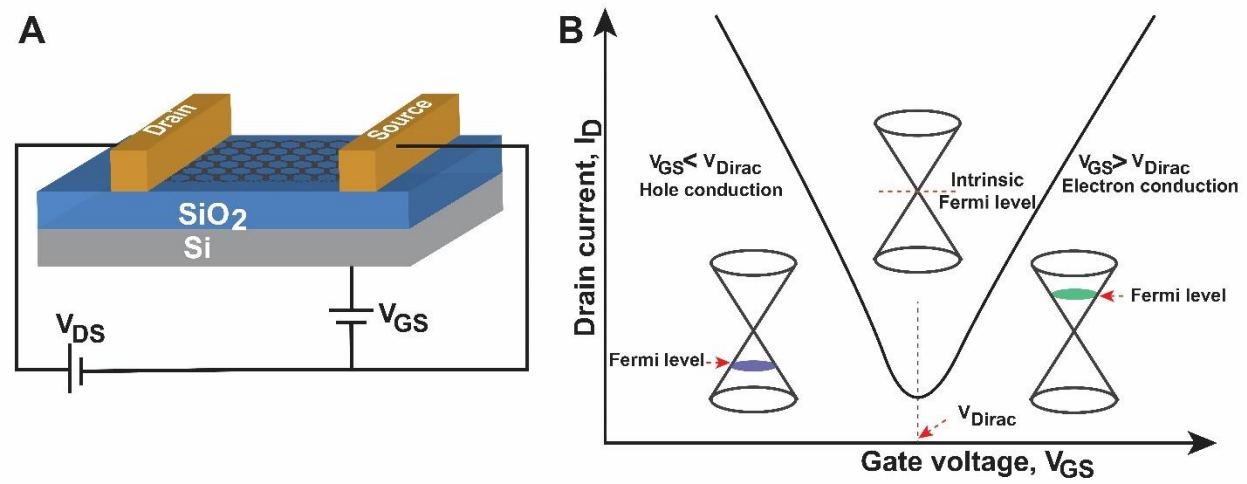

Figure 3.8. Schematic illustration of the (A) device structure of a graphene filed-effect transistor (back-gated); and (B) ambipolar transfer characteristics of the GFET device showing regions for hole and electron conduction.

Due to zero-bandgap structure of graphene, carriers (electrons and holes) can be converted to each other at the Dirac point resulting in the formation of ambipolar transfer characteristics as shown in Figure 3.8B. In the absence of any doping, the gate voltage at the minimum current is the charge neutrality point, V_{CNP}, usually referred to as the Dirac voltage, $V_{Dirac.}$, which corresponds to having the Fermi level at the Dirac point (Intrinsic Fermi level). For $V_{GS} > V_{Dirac}$ the Fermi level is in the conduction band and the channel current is due to the electron conduction, while for $V_{GS} < V_{Dirac}$ the Fermi level is in the valence band and the channel current is due to the hole conduction. With V_{GS} near V_{Dirac}, there are a few of either type of carriers and the conductivity of graphene is minimum. However, the non-zero current here is due to the thermal distribution of carriers as well as spatial fluctuations in energy of the Dirac point [84]. Any adsorbed charged molecule on graphene channel surface can induce a horizontal shift to the Dirac point, which can be used as an additional sensing mechanism.

3.2.2.2. Electrolyte-Gated GFET (EGFET)

To apply a GFET to the in-vitro real-time biosensing, the graphene channel must be in exposed to the sample solution. This can effectively be done by replacing the insulating material covering the gate electrode with an electrolyte solution leading to the so-called electrolyte-gate GFET (EGFET)

device [85]. An EGFET is schematically illustrated in Figure 3.9A. There are several advantages of EGFETs compared to conventional GFETs discussed above. The advantages are listed below [85]–[87]:

- Low operating potential (<1V) preventing undesired redox reaction or even water splitting enabling sensing of biomolecules in aqueous environment.
- Very stable performance and high transconductance.
- Low noise operation.
- Enables real-time measurement.

In an EGFET, the semiconductor channel and the gate electrode are in direct contact with the electrolyte, forming two electrical double layer (EDL) capacitors (C_{G1} and C_{G2}) in series (Figure 3.9B), equivalently known as the geometrical capacitance, C_G. The total capacitance can be expressed by the following equation [88]:

$$\frac{1}{C} = \frac{1}{C_G} + \frac{1}{C_Q}$$

Where C_Q is the quantum capacitance of graphene is related to the Fermi level shift and hence the potential drop across this capacitance controls the Fermi level shift. Each of the geometrical capacitance can be modeled as a parallel plate capacitor with a plate distance *d*, which is equal to a new quantity called the Debye length.

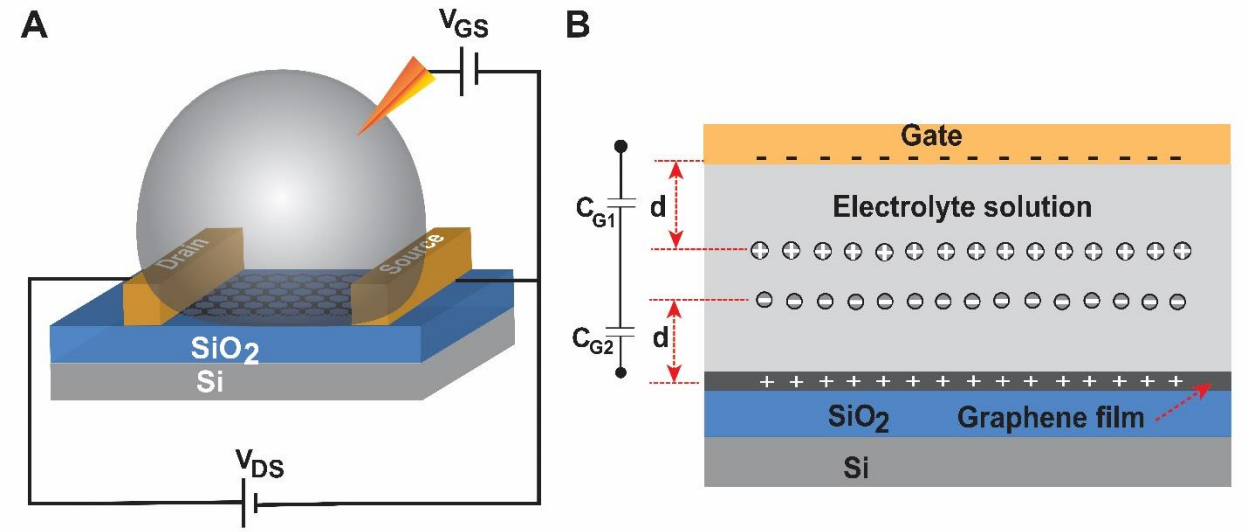

Figure 3.9. Electrolyte-gated graphene field effect transistor: (A) Schematic illustration; and (B) the electrical double layer capacitors formed at the graphene-solution and gate electrode-solution interfaces.

To fully describe the graphene FET-based sensing mechanism, two major effects caused by the presence of charged molecules on the graphene film must be considered; that is the electrostatic gating effect and the charge transfer doping effect. These two effects impose opposing actions on the sensing mechanisms. The actual sensing mechanism may be determined by the combination of these two mechanisms.

The electrostatic gating effect dominates when the concentration of the adsorbed charged molecule is high so that the inter-molecular distance is less than the Debye length and the adsorbed molecules behave as one of the two plates of the electric double layer (EDL) formed on the graphene-electrolyte interface. Now, any additional charged molecule adsorbed on graphene will modulate this charge density in the EDLs resulting in a change in the channel current as well as causing a shift in the Dirac point. If the adsorbed biomolecules are positively (or negatively) charged, the Dirac voltage will shift in the negative (or positive) direction. In other words, if more positive charges are attached to graphene, the applied voltage must be less positive in order to compensate for the additional charge [89], [90].

The charge transfer doping effect is caused by the direct charge transfer (Figure 3.10) from the adsorbed molecules to graphene channel especially when the adsorbed species are at low concentration or weekly charged. In this case, the adsorption density is quite small and the distance between the adsorbed molecules is larger than the Debye length of the channel material and the charge transfer is dominant between the adsorbed species and the channel material. The Dirac voltage shift caused by the charge transfer doping effect is in the opposite direction to that caused by the electrostatic gating effect. For example, if the adsorbed molecules are positively (or negatively) charged, the Dirac voltage will shift in the positive (or negative) direction [89].

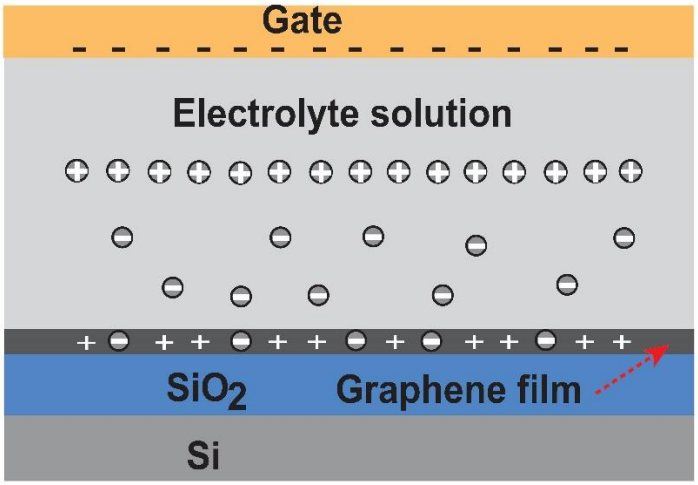

Figure 3.10. Schematic illustration of doping effect in graphene field-effect transistor.

Due to the several advantages EGFETs offer with respect to the biosensing applications, several groups have implemented this configuration for developing GFET based biosensors for highly sensitive detection of biomolecules. As an example, Wang et al. successfully used a label-free EGFET device for immunoglobin E (IgE) biomarker in human serum with a limit of detection in 47 pM [91]. Hao et al. developed another EGFET biosensor for real-time monitoring of insulin with a limit of detection of 35 pM [79]. They also demonstrated that these GFET biosensors can find applications in clinical diagnostics for label-free monitoring of insulin and timely prediction of accurate insulin dosage.

3.2.2.3. Debye length

One of the factors that limit the capabilities of GFET biosensors is the Debye length, which is the maximum distance away from the graphene surface beyond which the GFET device is able to screen a charge. The Debye screening length of an electrolyte is given by [92]:

$$d = \sqrt{\frac{\epsilon\epsilon_0 k_B T}{2nZ^2e^2}}$$

where n is the bulk concertation of ions in the solution, Z is the charge of the ion and e is the charge of an electron. The Debye length can be approximated as:

$$d \approx 0.96\sqrt{\frac{0.1}{c}}\,\text{nm}$$

where c is the molar concentration of the buffer salt solution. For aptamer-based GFET sensors, the concentration of buffer solution should be such that the Debye length is essentially greater than the aptamer length.

Another factor that limits the performance of a GFET biosensing device is the Faradic currents which are created by the reduction or oxidation of the molecules at the liquid-electrode interface. This causes an unwanted leakage current through the gate electrode. In general, Faradic currents should be less than 1 nA. One of the ways to reduce Faradic currents is by passivation of the electrodes with a layer of oxide to reduce the interaction between the electrode surface and the solution [93].

3.3. Conclusion

In this chapter, I discuss the theory of carbon-based nanoelectronics. Specially, two popular carbon nanomaterials, namely CNT and graphene are discussed—their electronic and electrochemical properties, manufacturing, as well as significance in biosensing. Moreover, I present a brief literature review on biosensing principles using both nanomaterials.

CHAPTER 4: INKJET-PRINTED APTAMER-BASED ELECTROCHEMICAL BIOSENSOR

4.1. Introduction

Aptamers hold great interest to the scientific community due to their versatile advantages with regards to biosensing. Their many advantages, including high affinity and binding efficiency to the target analyte, chemical and thermal stability, resistance to harsh environmental conditions, long shelf-life, mass producibility at low-cost, and reusability make aptamers attractive alternatives to their natural counterparts, such as antibodies and enzymes [54], [94]. Selected in vitro by a well-established technique known as the Systematic Evolution of Ligands by EXponential enrichment (SELEX), aptamers can be used for the selective detection of a broad range of analytes including proteins, peptides, amino acids, drugs, metal ions, and even whole cells [95]. The detection of lysozyme has received much attention among researchers because of its various significances in medicine, as well as in the food industry. Having a molecular weight of 14.4 kDa with a primary sequence containing 129 amino acids and an isoelectric point of 11.0, lysozyme is a ubiquitous enzyme widely available in diverse organisms such as bacteria, bacteriophages, fungi, plants, and mammals [96], [97]. Lysozyme also plays an important role as a biomarker for diagnosing diseases such as breast cancer [98], Alzheimer's disease [99], rheumatoid arthritis [100], malaria [101], AIDS [102], tuberculosis and leprosy [103], sarcoidosis [104], and Crohn's disease [105]. Typically, the concentration of lysozyme in a healthy person's saliva is 13.8 µg/mL [59], whereas the concentration is 0.463–2.958 µg/mL in a healthy person's serum [94].

Existing aptamer-based biosensors use different detection schemes such as high-performance liquid chromatography (HPLC), quartz crystal microbalance (QCM), surface plasmon resonance (SPR), and fluorescence-based optical detection. However, these methods suffer from several drawbacks as they are often time-consuming, expensive, operated by highly trained technicians, and performed in a laboratory setting [54], [106]. However, as an alternative, electrochemical detection offers the potential for a rapid, low-cost, and sensitive detection of the target species. Especially, electrochemical impedance spectroscopy (EIS) has proven to be a powerful and

sensitive tool for investigating the features of surface-modified electrodes [106]. EIS can be used to monitor the changes in the electrical properties of the biosensor at different stages, including different fabrication steps as well as the detection of target recognition events [26]. The unique advantages of EIS include the ease of signal quantification, the ability to separate the surface binding events from the solution impedance, non-invasive measurement, real-time monitoring, and label-free detection, making it an effective tool for electrochemical interrogation [26].

An important step towards the fabrication of the aptamer-based electrochemical biosensor is the immobilization of the aptamer probes onto the working electrode so that the target recognition by the aptamer can be transduced into a measurable electrical signal. Rohrbach et al. developed a lysozyme biosensor where the covalent coupling between the carboxylic groups of CNT and the amino groups linked to the aptamer was used to immobilize the aptamer [54]. An EDC/NHS coupling-based immobilization technique has been exploited by Kara et al. to develop an aptamer-based biosensor for the detection of thrombin with a detection limit of 105 pM using EIS [53]. Others have used thiol-gold binding [59], [106], [107], biotin-avidin affinity-based binding [108], and surface adsorption [109] to immobilize aptamers on the respective electrodes. However, such approaches can be difficult to reproduce, often require complex chemistry, lack control over aptamer density, and may not be suitable for large-scale manufacturing and mass production.

Herein, we explore the possibility of using the inkjet-printing technique for a reliable and reproducible aptamer immobilization method. We propose the use of a dispersed CNT-aptamer complex as a printable ink to be deposited on the electrode. The ink exploits the strong π–π stacking interaction between the nucleotide bases of the single stranded DNA and the sidewalls of the CNT [57]. Inkjet-printing is finding applications in areas such as flexible electronics, disposable sensors, and wearable devices [110]. Particularly, due to its on-demand printability of the devices, inkjet-printed sensors can potentially be used as point-of-care (POC) diagnostic tools and disposable testing kits. In contrast to other existing aptamer immobilization techniques, the proposed approach of inkjet-printing offers many advantages, including mass producibility, uniform deposition of materials, fully automated process, and high throughput [110]–[112]. We also demonstrate in this work that the aptamer density can be controlled by utilizing the number of printing layers. After the deposition of the CNT-aptamer ink, the sensor is then used for the

detection of lysozyme using EIS. The binding affinity of our aptamer probe to lysozyme was confirmed by the square wave voltammetric techniques using methylene blue (MB)-labeled aptamers (see Appendix B).

Figure 4.1 presents the working principle of our proposed biosensor. Figure 4.1A shows the CNT-aptamer complex deposited on the working electrode. Due to the negatively charged backbone as well as the insulating property of the aptamers, the charge (electron) transfer from the redox probe (e.g., ferro- and ferri-cyanide) to the electrode is hindered, i.e., the charge transfer resistance (R_{ct}) is large as illustrated by the larger diameter of the Nyquist plot in Figure 4.1B. When the sensor is exposed to lysozyme as shown in Figure 4.1C, the aptamer unwraps itself from the CNT due to its preferential binding to the lysozyme. This conformational change in the aptamers opens up the path for electrons to easily flow from the redox probes to the working electrode, resulting in an enhancement in the rate of charge transfer and thus a reduction in R_{ct}, as shown in Figure 4.1D with a smaller radius of the Nyquist curve.

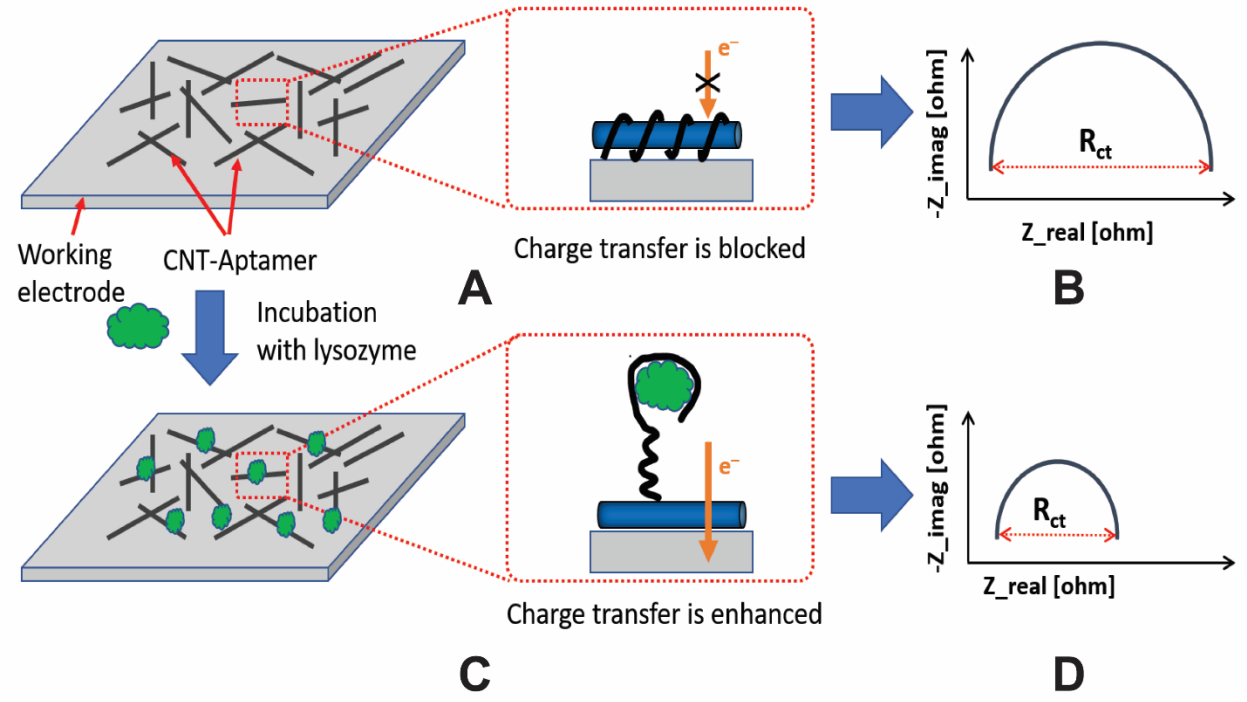

Figure 4.1. Working principle of the aptamer-based biosensor. Initially, the printed sensor blocks the charge transfer from the redox probe to the electrode due to the negative backbone of DNA bases (A); and the corresponding Nyquist curve (B). When exposed to the lysozyme, the anti-lysozyme aptamer unwraps itself from the carbon nanotube (CNT) and binds to the lysozyme,

opening up the current path for enhanced charge transfer (D); and the corresponding Nyquist curve (D).

4.2. Materials and Methods

4.2.1. Materials

Multi-walled carbon nanotubes (>99.9% purity, 30–50 nm outer diameter, 10–20 μm length) modified with carboxyl functional groups (–COOH) were purchased from Cheap Tubes (VT, USA) and used without further modification. Single-stranded anti-lysozyme DNA oligonucleotides (sequence designed by Ellington and co-workers [113]) were synthesized by Sigma-Aldrich. The sequence of the oligonucleotides is: 5′-ATC AGG GCT AAA GAG TGC AGA GTT ACT TAG-3′. Methylene blue (MB)-labeled and thiolated DNAs with the same sequence (thiol group attached at the 5′ end MB attached at 3′ end) were purchased from LGC Biosearch Technologies (CA, USA). Lysozyme from chicken egg white, bovine serum albumin, and thrombin were also purchased as lyophilites from Sigma-Aldrich. The stock solutions were prepared by dissolving the lyophilites in fresh ultrapure triple-distilled water and stored at −20 °C until used. The diluted solutions of proteins were prepared in 50 mM phosphate buffer solution (PBS, pH 7.4, Sigma-Aldrich).

4.2.2. Electrochemical Assay

The Bio-Logic VSP-300 potentiostat was used for the electrochemical measurements. All experiments were performed using screen-printed carbon electrodes (SPCEs) purchased from DropSens (Spain). These disposable SPCEs consist of three electrodes: a carbon working electrode (WE), a carbon counter electrode (CE) and a silver pseudo reference electrode (RE). The WE is circular in geometry with a diameter of 4 mm.

4.2.3. Ink Preparation

First, 0.25 mg/mL of multi-walled carbon nanotubes (MWCNTs) were mixed with 5 μM lysozyme binding aptamer in 30% N-methyl pyrrolidone (NMP) solution. Next, the mixture was sonicated using an ultrasonic bath sonicator for 2 h and then centrifuged at 6000 rpm for 30 min in order to remove any MWCNT aggregates. Afterwards, the supernatant was collected and loaded into the ink cartridge for printing. The unused ink was stored in a refrigerator at 4 °C.

4.2.4. Inkjet-Printing

The Fujifilm Dimatix Materials Printer (DMP-2831) was used for the inkjet-printing. It uses a 16-jet Dimatix Materials Cartridge with 10 pL drop volumes. The minimum patterning resolution of this printer was reported to be 20 µm according to the product specification sheet. Each device was printed with 5 layers of the CNT-aptamer ink. The ink was printed at a voltage of 40 V, a nozzle temperature of 35 °C and a 5 kHz jetting frequency. The amount of ink printed per layer is estimated to be approximately 315 nL (see Appendix A for detailed calculation).

4.2.5. Removal of the Unbound Aptamers

After the printing process, the SPCE devices were dried on a hotplate at 35 °C and gently washed with deionized (DI) water to remove any unbound DNAs. The effect of washing is presented in Figure 4.2.

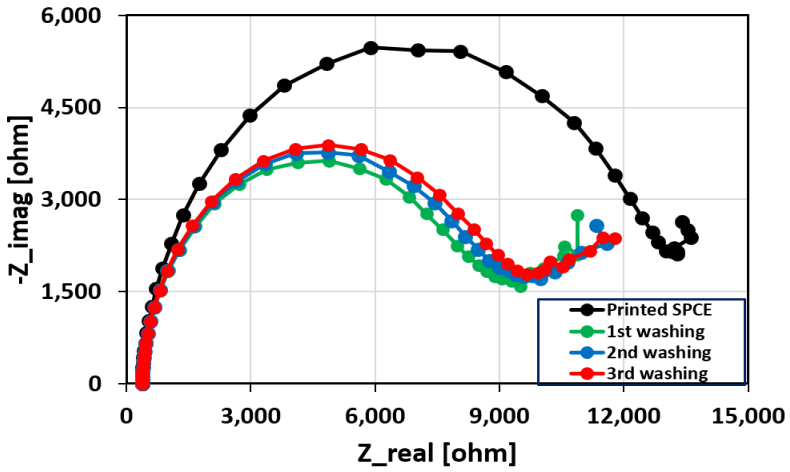

Figure 4.2. The effect of washing on the printed sensor. After the first wash, the R_{ct} value obtained from the Nyquist curve drops by approximately 31%. Subsequent washes do not significantly change the radius of the Nyquist curves, suggesting that the remaining aptamers are securely attached to the CNTs.

It can be seen that the radius of the Nyquist curve corresponding to the first wash drops significantly and remains stable for the subsequent washes. This indicates that the majority of the unbound or loosely bound aptamers have been removed after the first rinsing procedure during which 31% reduction in the charge transfer resistance has been observed.

4.2.6. EIS Measurements

The electrochemical impedance spectroscopy (EIS) measurements were performed with 1 mM $K_4[Fe(CN)_6]/K_3[Fe(CN)_6]$ (1:1) mixture (pH: 7.25) as a redox probe prepared in 10 mM PBS. The impedance was measured in a frequency range from 100 kHz to 100 mHz with a DC potential of 0.115 V versus Ag pseudo reference with a sinusoidal AC voltage of 5 mV RMS. The sampling rate was 10 points per decade. The charge transfer resistance (R_{ct}) of the equivalent circuit was obtained by fitting the measured Nyquist curve using a modified Randles circuit.

First, the EIS measurement was taken on a CNT-aptamer ink-printed SPCE by placing a 50 µL droplet of the ferro-/ferri-cyanide solution on the surface of the electrode for obtaining the baseline measurement (this will be called pre-lysozyme measurement). Next, the same device was exposed to a 50 µL droplet of lysozyme of varying concentrations (0, 0.25, 0.50, 1, 2, 5, 10, and 20 µg/mL) and incubated for 15 min. The electrode was then rinsed with 50mM PBS buffer followed by rinsing in DI water to remove any unbound lysozyme protein. Afterwards, a second EIS measurement was performed to obtain the response of lysozyme binding with the aptamers (this will be called post-lysozyme measurement).

After making two rounds of EIS measurements on the same device, one for the pre-lysozyme condition and one for the post-lysozyme condition, the R_{ct} values were obtained by curve-fitting the Nyquist plot to the modified Randles circuit model. The relative change of the transduction signal (ΔR_{ct}) can be calculated in percentage as follows:

$$\Delta R_{ct}(\%) = \frac{R_{ct,post} - R_{ct,pre}}{R_{ct,pre}} \times 100\% \quad (1)$$

where $R_{ct,pre}$ and $R_{ct,post}$ denote the charge transfer resistances of the pre-lysozyme and post-lysozyme measurements, respectively.

4.2.7. Chronocoulometric Experiments

To calculate the packing density of aptamers on the WE, chronocoulometry (CC) was performed by applying a pulsed voltage with a pulse width of 200 mV versus Ag pseudo reference and a pulse period of 10 s. First, the measurement was done with the sensor in 10 mM Tris-HCl buffer. Next, the sensor was incubated in 1 mM hexamine ruthenium (III) chloride (RuHex) in 10 mM Tris-HCl

for 1 h. Then, the sensor was washed in DI water to remove any excess RuHex that was not bound to the DNA aptamer. Finally, the CC was performed for the RuHex incubated sensor. Following the experiment, the aptamer packing density was calculated from the CC intercepts at $t = 0$. See Appendix C for the experimental details.

4.3. Results and Discussion

4.3.1. Patternability of the CNT-Aptamer Ink

The patternability of the aptamers has been characterized optically by fluorescence imaging. For the ink preparation, the aptamers were labeled with a fluorescence (6-FAM) modified at the 5′ end. Different numbers of layers (one to eight) were printed on a microporous PET transparency film as a single droplet array, as shown in Figure 4.3A. The droplet array was washed with DI water before imaging to remove loosely adsorbed aptamers that remained from the ink. The intensity profile of the array is presented in Figure 4.3B against the number of printed payers. It can be seen that, for the number of print layers from one to six, the fluorescence intensity is proportional to the number of layers. However, for seven and eight layers of printing, the intensity decreases slightly. This decrease in intensity for higher number of layers can be attributed to the possible quenching of the fluorophore due to the overcrowding of the aptamers that can lead to the cross-hybridization among neighboring aptamers, a potential result of the self-complimentary nature of the individual aptamer sequences [114]. Furthermore, the coffee ring effect [115] becomes more pronounced for higher number of layers, as can be seen in Figure 4.3A. In summary, we have demonstrated the ability to control the density of the immobilized aptamer by choosing the proper number of printed layers. Furthermore, a minimum patterning resolution of 40 μm was obtained with the CNT-aptamer ink. Figure 4.3C shows the scanning electron microscope (SEM) image of the CNT-aptamer ink, which shows well-dispersed nanostructures that allow easy access to the aptamers by lysozyme proteins.

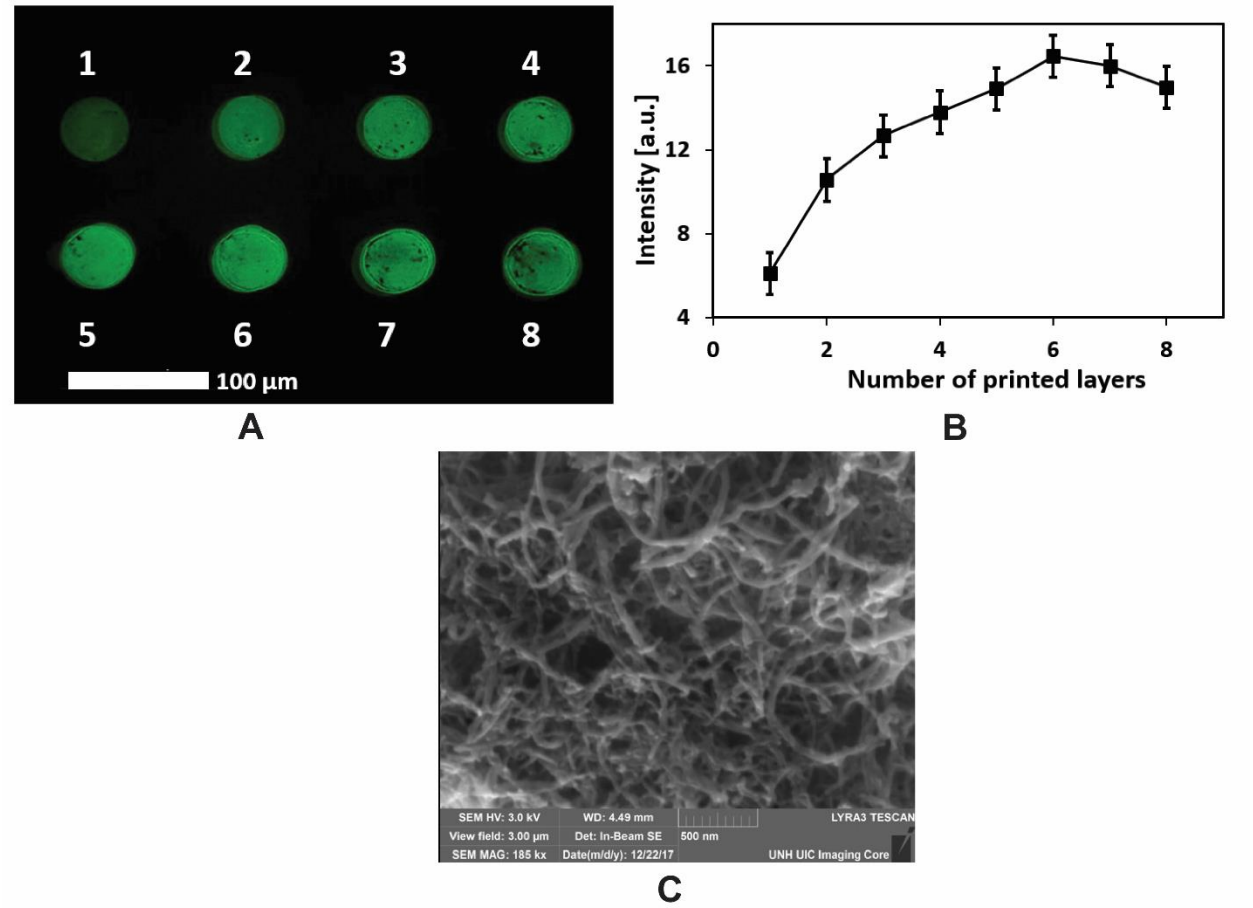

Figure 4.3. (A) Fluorescence image of the printed CNT-aptamer ink in a single-droplet array with different numbers of layers (as indicated by the numbers in the image); and (B) the intensity profile of the printed circles versus the number of layers. Each droplet has a diameter of 40 µm; (C) shows an SEM image of the CNT-aptamer ink used for lysozyme recognition.

4.3.2. Characterization of the Sensor

Figure 4.4 shows the Nyquist curves of the SPCE with different modifications on the working electrode: (a) bare device, (b) with CNT ink printed, and (c) with CNT-aptamer ink printed. When the electrode is printed with CNT only, the charge transfer resistance (R_{ct}) decreases due to the highly conducting nature of MWCNT. However, when the electrode is printed with the CNT-aptamer ink, the R_{ct} increases significantly due to the negative charges of the single-stranded DNA oligonucleotides, as well as the electrical shielding of the CNTs by the insulating DNAs.

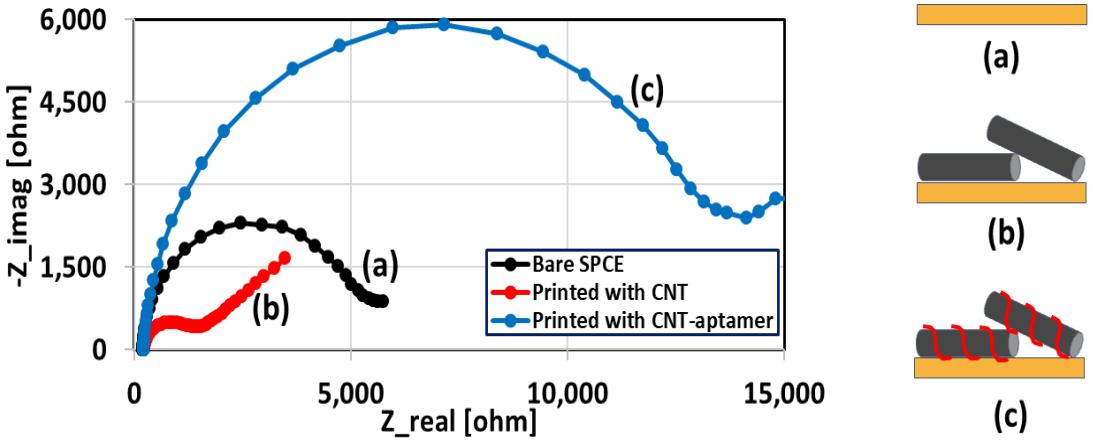

Figure 4.4. The Nyquist curves obtained with electrochemical impedance spectroscopy (EIS) measurements at different modification stages of the electrode: (a) bare screen-printed carbon electrode (SPCE); (b) printed with CNT ink; and (c) printed with CNT-aptamer ink. Aptamer wrapping to CNTs significantly increases the charge transfer resistance (R_{ct}) due to the negative backbone of the DNA aptamers.

Figure 4.5 compares the responses of the printed sensor before and after exposure to the target protein biomarker. As can be seen from the figure, when the sensor is exposed to lysozyme, R_{ct} decreases considerably. This can be attributed to the conformational changes of the anti-lysozyme aptamers upon specific binding to the target, resulting in an unwrapping of the DNAs from the CNTs. The unwrapped aptamers are then removed from the device via rinsing the electrode, thereby decreasing the charge transfer resistance.

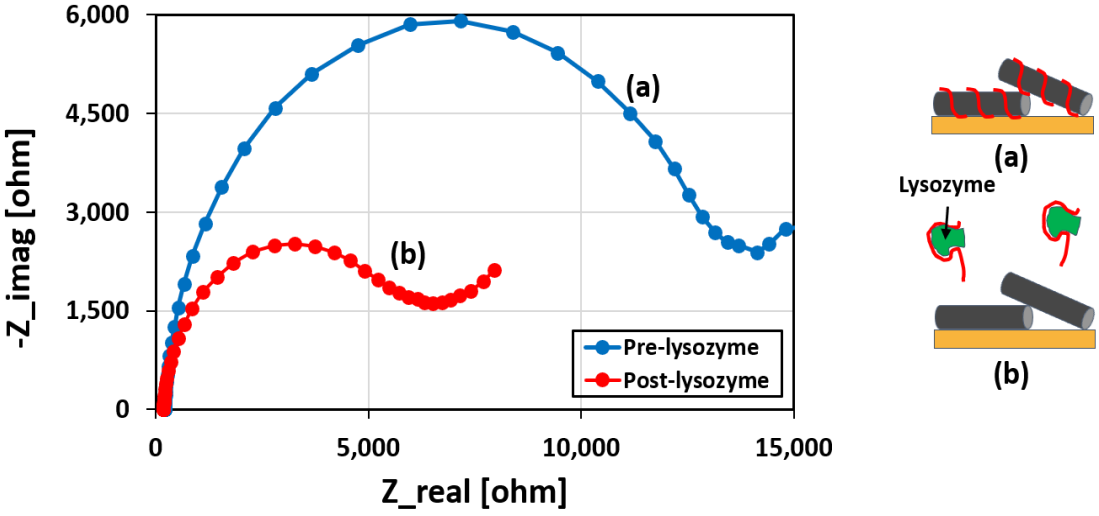

Figure 4.5. Effect of lysozyme exposure on the printed sensor. Nyquist curves for (a) pre- and (b) post-lysozyme conditions. It can be observed that lysozyme (1 µg/mL) exposure reduces the charge transfer resistance (Rct) because of the unwrapping of the anti-lysozyme aptamers from the CNTs to capture the lysozyme protein.

Lysozyme binding of the aptamers was further confirmed by comparing the responses of the printed devices with those of bare SPCEs. As summarized in Figure 4.6, the change in R_{ct} is much larger for the printed sensor than for the bare electrode. The R_{ct} changes in the bare electrodes are likely due to the non-specific adsorption of the target biomarker on the electrode surface.

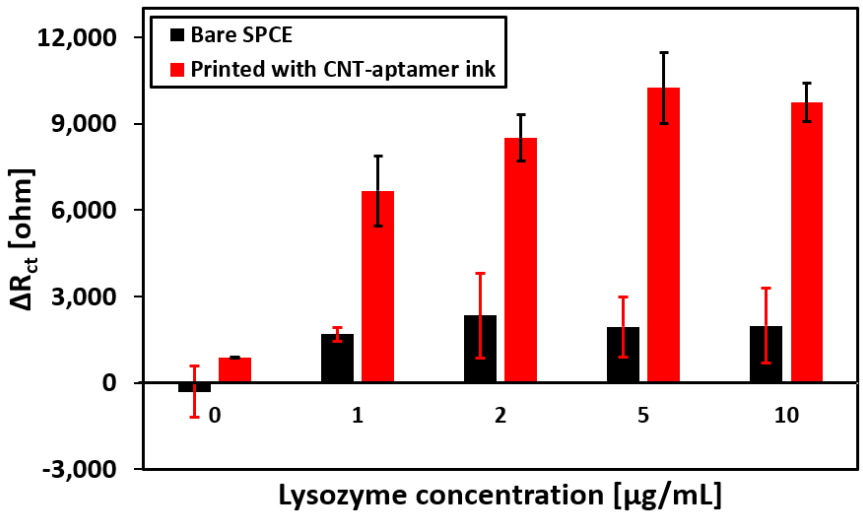

Figure 4.6. Change of charge transfer resistance (R_{ct}) due to lysozyme exposure to bare SPCE (black bars) and printed SPCE (red bars) for different lysozyme concentrations.

4.3.3. Packing Density of the Aptamer Probes

The theoretical number of aptamer probes printed on the working electrode can be calculated as follows:

$$n = M \times V \times (1 - \chi) \times 6.023 \times 10^{23} \qquad (2)$$

where *n* is the number of aptamer molecules, *M* is the molarity (=5 µM) of the aptamers in the ink, *V* is the volume (=1.575 µL) of ink printed (see Appendix A), and χ accounts for the fraction of aptamers not attached to the CNT during the sonication-assisted dispersion of the CNT-aptamer mixture and can be estimated from the experimentally calculated probe density as detailed below.

Experimentally, the probe packing density can be calculated by the integrated Cottrell equation [116]:

$$Q = \frac{2nFAD_0^{1/2}C_o}{\sqrt{\pi}} t^{1/2} + Q_{dl} + Q_{SE} \quad (3)$$

where *n* is the number of electrons per molecule for reduction, *F* is the Faraday constant (96485.33 C/mol), *A* is the electrode area (cm^2), D_o is the diffusion constant (cm^2/s), C_o is the bulk concentration (mol/cm^3), *t* is the time (s), Q_{dl} is the double layer capacitive charge (C/mol) and Q_{SE} is the surface excess charge (C/mol) from the reduction of the adsorbed redox marker. Q_{SE} is related to the density of the redox probe, Γ_0 (mol/cm^2) by the following equation [26]:

$$\Gamma_0 = \frac{Q_{SE}}{nFA} \quad (4)$$

The value for Q_{SE} can be calculated from chronocoulometry experiments. The chronocoulometric intercept at $t = 0$ is the sum of the double layer capacitive charge and the surface excess charge. The surface excess charge (Q_{SE}) is determined from the difference in chronocoulometric intercepts (at $t = 0$) in the presence and absence of the redox probes for the identical potential steps. The density of the aptamer (Γ_{DNA}) is given by the following equation [26]:

$$\Gamma_{DNA} = \Gamma_0 \frac{z}{m} N_A \quad (5)$$

where *z* is the charge of each redox molecule, *m* is the number of nucleotides in the aptamer base sequence, and N_A is Avogadro's number. Chronocoulometry was performed for different number of printed layers (see Appendix A). The experimentally calculated packing density for different number of layers is plotted in Figure 4.7. The graph shows that the packing density increases with increasing number of printed layers, and then saturates for further number of layers. This saturation effect can presumably be attributed to the steric and electrostatic repulsion among the negatively charged aptamers [117].

Now if equation (2) is used to linearly fit the experimental data points of Figure 4.7, the value of χ can be estimated as $\chi = 98.7\%$. Therefore, the number of aptamer molecules printed per layer on the WE (area: 0.12 cm^2) of the electrode can be estimated as 1.23×10^{10} molecules per layer. Hence, the aptamer density can be calculated as approximately 1.03×10^{12} molecules/cm^2 per

layer. Furthermore, using this value of χ, the final concentration of the aptamers present in the printed ink can be estimated as 65 nM.

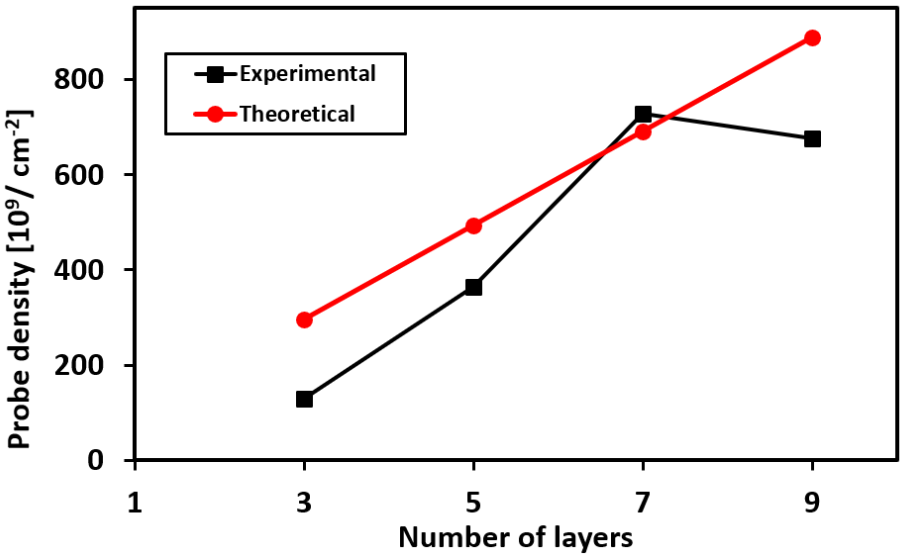

Figure 4.7. Packing density of aptamer probes as a function of number of printed layers.

The influence of the number of printed layers on the sensing performance was also characterized. As presented in Figure A4 in Appendix A, it was observed that the sensor response experiences a nearly linear increase (region 1) with increasing number of printed layers until it reaches a plateau and then decreases afterwards (region 2). This is because at lower number of printed layers (region 1), the sensitivity is proportional to the concentration of aptamer receptors, i.e., more aptamers lead to increasing binding. However, for increased number of layers (region 2), the aptamers that are buried deep in the printed ink are not able to bind with the protein and hence remain as electrical insulators, resulting in poor sensitivity. The plot in Appendix A illustrates the influence of the number of printed layers on the sensor's sensitivity. Also, the sensor's response time correlates with the thickness of the printed layers, in other words, the number of prints on the electrode. In our experiments, all devices were printed five times for lysozyme detection.

4.3.4. Performance of the Aptamer Sensor

The performance of the aptamer sensor has also been characterized by measuring the relative change in sensor response for different concentrations of lysozyme analyte. The results are presented in Figure 4.8, where each sensor contains five layers of printed CNT-aptamer ink.

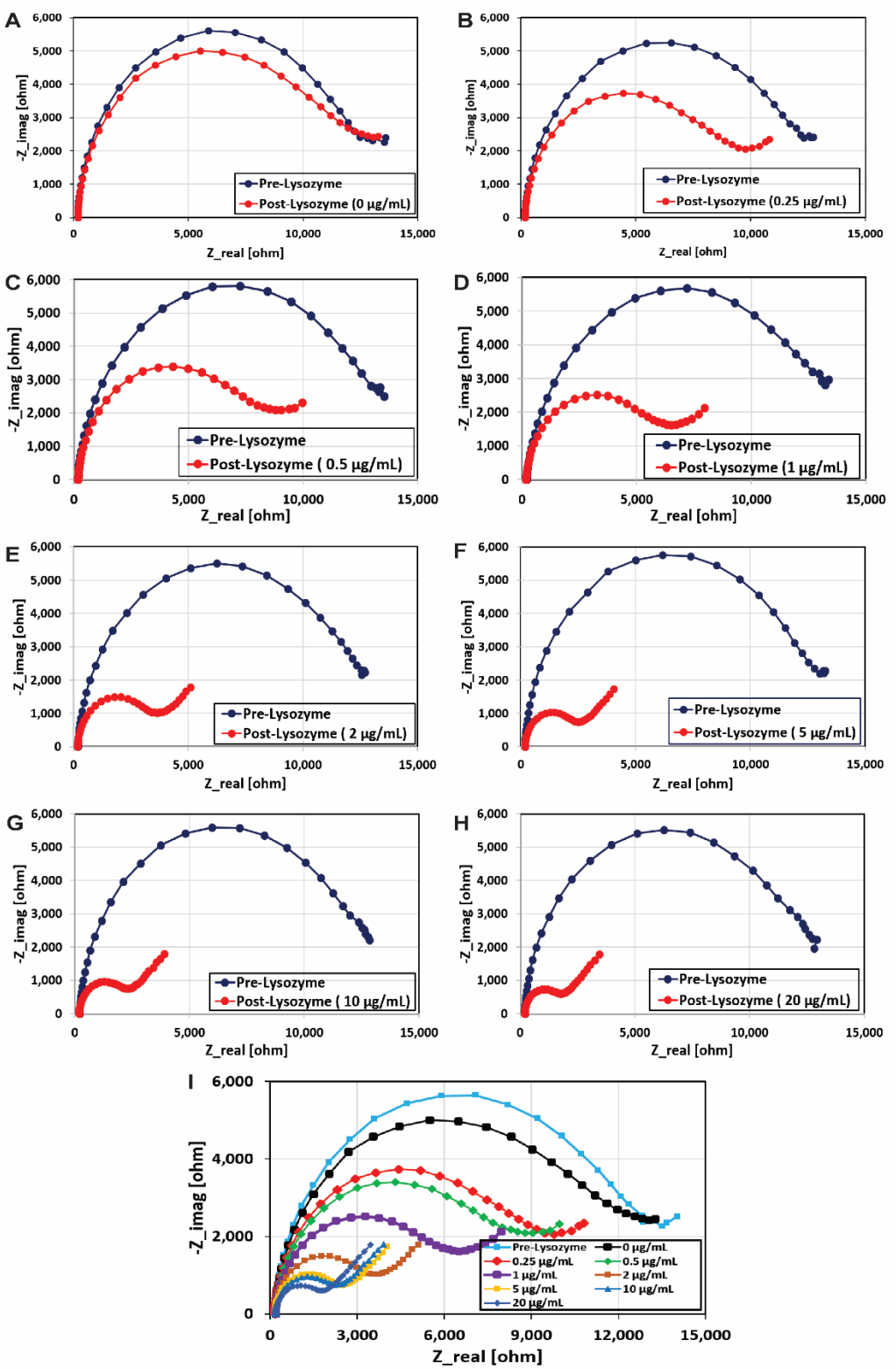

Figure 4.8. (a)–(h) Pre- and post-lysozyme Nyquist curves for different concentrations of lysozyme (0, 0.25, 0.5, 1, 2, 5, 10, 20 µg/mL, respectively) in 50 mM PBS as well as (i) post-lysozyme Nyquist curves for all the lysozyme concentrations.

4.3.5. Modelling of the Nyquist Curves

The pre- and post-lysozyme Nyquist curves can be modelled by the modified Randles circuit shown in Figure 4.9, where R_S is the solution resistance, R_{ct} is the electron transfer resistance, CPE (constant phase element) represents the double layer capacitance at the solution–electrode interface for a rough surface [118], and W_1 is the Warburg impedance.

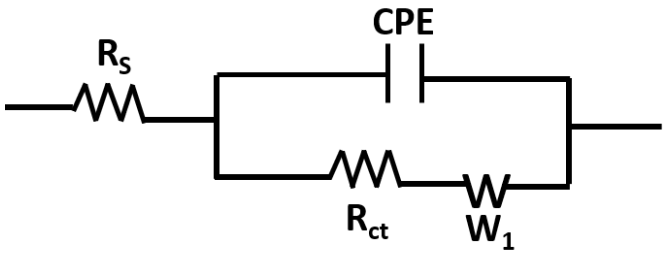

Figure 4.9. Modified Randles circuit representing the equivalent circuit model to fit the Nyquist curves of the EIS measurements.

The CPE accounts for the roughness of the electrode surface and, mathematically, its impedance is (Z_{CPE}) described by the following equation [119]:

$$Z_{CPE} = \frac{1}{Q_1 \times (j\omega)^{\alpha_1}} \quad (6)$$

where *j* is the imaginary unit, and α_1 and Q_1 are the characteristic parameters of the constant phase element. The introduction of the CPE instead of a simple capacitance is particularly important for the modelling of primary protein layers on the electrode surface, and the parameter α_1 was found to vary between 0.925–0.961 for our sensor devices. For α_1 = 1, the CPE turns into a simple capacitance. W_1 is the circuit element corresponding to Warburg impedance resulting from the semi-infinite diffusion of ions from the bulk electrolyte to the electrode interface and is mathematically given by [120]:

$$Z_{W1} = \frac{\sqrt{2}\,\delta_1}{\sqrt{j\omega}} \quad (7)$$

where δ_1 is the characteristic value of the Warburg element. Table 4.1 summarizes the modified Randles circuit parameters of the post-lysozyme Nyquist curves of Figure 4.8I.

Table 4.1. Randles circuit parameters for the post-lysozyme Nyquist curves in Figure 4.8I (Data extracted using Zfit program of Bio-Logic EC-Lab software).

Lys Concentration (µg/mL)	R_{ct} (ohms)	CPE ($\mu F \cdot s^{n-1}$)	α_1	R_s (ohms)	δ_1 ($ohm \cdot s^{1/2}$)
0	10511	4.734	0.962	186	2086
0.25	7850	4.567	0.963	172	2154
0.50	7251	6.158	0.944	178	1928
1	5359	5.313	0.943	185	1833
2	3028	4.917	0.968	175	1554
5	2064	4.449	0.970	178	1501
10	1869	5.518	0.969	189	1542
20	1435	5.526	0.961	192	1491

Figure 4.10 shows the theoretically fitted post-lysozyme Nyquist curves based on the modified Randles circuit (red solid lines). The dotted lines represent the experimental data. The graph shows good agreement between the experimentally obtained Nyquist curves and those obtained from the theoretical model.

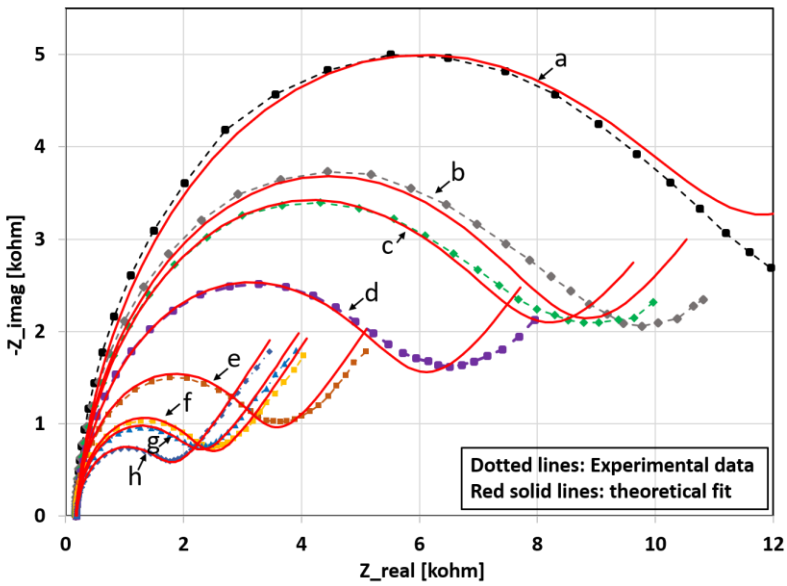

Figure 4.10. Post-lysozyme exposure Nyquist curves for different concentrations of lysozyme: (a) 0 µg/mL; (b) 0.25 µg/mL; (c) 0.50 µg/mL; (d) 1 µg/mL; (e) 2 µg/mL; (f) 5 µg/mL; (g) 10 µg/mL;

and (h) 20 µg/mL. The dotted lines are the experimental data and the solid lines in red are the theoretically fitted curves based on the modified Randles circuit.

The calibration curve for our aptamer-based sensor is presented in Figure 4.11. It shows that for low concentrations of lysozyme, the sensor exhibits high sensitivity and at higher concentrations (5 µg/mL and above) the sensor's response reaches a saturation. Based on this calibration curve, the detection limit was calculated to be 90 ng/mL. (See Appendix A for the formula used for calculation).

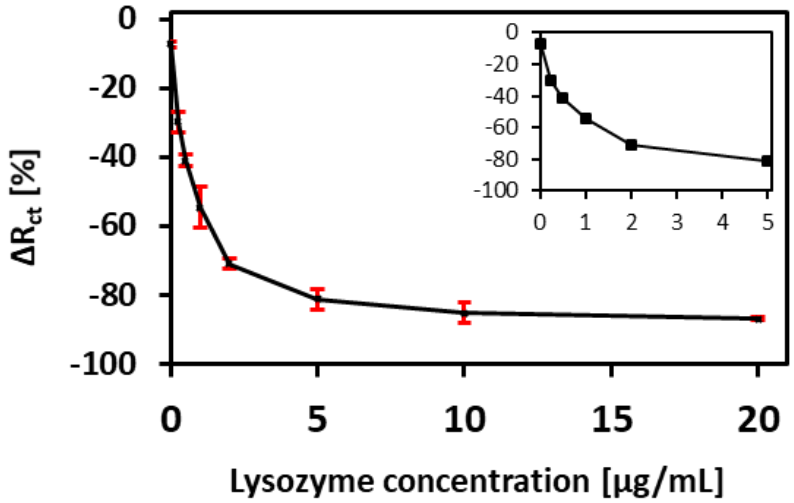

Figure 4.11. Relative change in charge transfer resistance (R_{ct}) after lysozyme exposure with varying concentrations (0, 0.25, 0.50, 1, 2, 5, 10, and 20 µg/mL). Error bar shows 1 standard deviation with n = 3. The inset graph shows the magnified plot for low concentration range from 0 to 5 µg/mL.

4.3.6. Selectivity of the Aptamer Sensor

The selectivity of our aptamer-based lysozyme sensor was investigated against two other proteins: thrombin (THR) and bovine serum albumin (BSA). It is clear from Figure 4.12 that our aptamer-based biosensor is highly selective toward lysozyme. The non-zero responses for THR and BSA can be attributed to the non-specific adsorption of the proteins on the sensor. Although the aptamers were designed to selectively bind with lysozyme, THR and BSA do have some level of affinity with the aptamers, resulting in a false recognition of the analyte. However, the non-specific binding efficiencies are significantly lower than that of lysozyme, hence the signal responses are

markedly smaller compared to the specific target recognition by lysozyme. Better optimization of the aptamer sequence is expected to further enhance the target selectivity. For instance, a 42-mer aptamer sequence (ATC TAC GAA TTC ATC AGG GCT AAA GAG TGC AGA GTT ACT TAG) is reported to have improved binding efficiency [121], which could further reduce the response from THR and BSA.

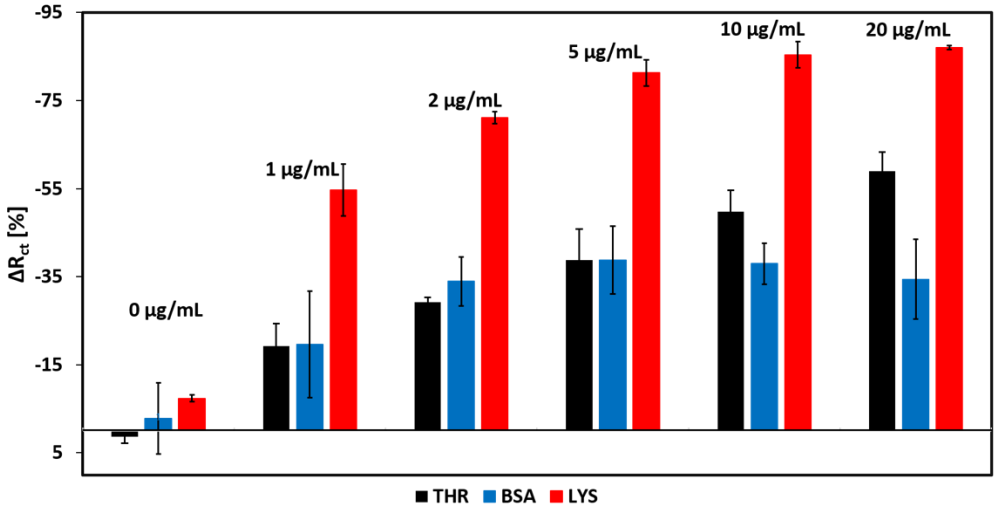

Figure 4.12. Selectivity of the aptamer biosensor to lysozyme against other proteins such as thrombin and bovine serum albumin for different concentrations.

4.3.7. Long-Term Stability (Shelf-Life) of the Aptamer-Printed Biosensor

The shelf-life or the long-term storage stability of the developed biosensor was investigated by storing the fabricated devices for a period of up to 35 days at room temperature. After the storage period, the sensor was tested by measuring the Nyquist curves for the pre-exposure and post-exposure measurements with the lysozyme concentration of 1 µg/mL. As can be seen from Figure 4.13, the sensor response is reasonably consistent (with a tolerance of ±1.73%) for the first 21 days, then experiences a drop in the resistance change afterwards. Hence, it can be concluded that our proposed sensor is stable for 21 days at room temperature. However, it is expected that the shelf-life would be further extended if the devices were stored in a cooler temperature, such as at 4 °C. Moreover, because we are utilizing an inkjet-printed sensor, one advantage is that the sensor can be printed on-demand so that the storage time can be minimized.

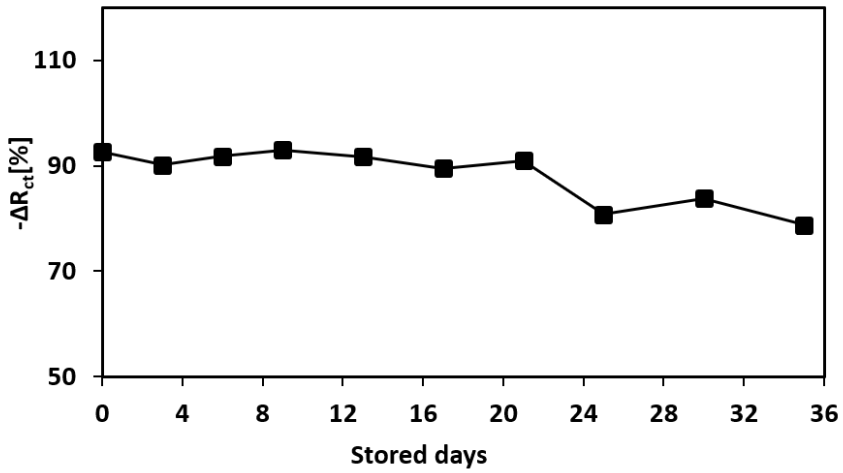

Figure 4.13. Shelf-life of the fabricated aptamer-based biosensor. The sensor response is plotted against the number of stored days at room temperature.

4.3.8. Comparison to Other Aptamer-Based Lysozyme Sensors

In order to compare the sensing performance presented in this work with other recently reported lysozyme sensors, Table 4.2 summarizes the detection limit (LOD), linear range, immobilization method, and detection mechanism of several recently published works. The table demonstrates that the sensor presented in this work shows comparable performances with other reported sensors. However, the main advantage and novelty of the proposed device is the convenience and the ease of immobilizing and patterning the aptamers on the electrode using the precision inkjet-printer for low-cost and disposable sensor development.

Table 4.2. Comparison of the sensing performances of recently published lysozyme sensors.

LOD	Linear Range	Immobilization Technique	Detection Mechanism	Ref.
12.09 µg/mL	0–200 µg/mL	Covalent	EIS	[54]
1.4 fg/mL	1.4 fg/mL–14 ng/mL	Thiol-Gold	SWV	[97]
7 ng/mL	14 ng/mL–1.12 µg/mL	Thiol-Gold	SPQC	[59]
0.14 fg/mL	1.4 fg/mL–6.96 pg/mL	Thiol-Gold	EIS	[26]
200 ng/mL	0–10 µg/mL	Biotin-Avidin	EIS	[108]
76.6 fg/mL	98.2 pg/mL–49.1 ng/mL	π–π stacking	DPV	[122]

0.4 pg/mL	1–50 pg/mL	Covalent	SWV	[123]
90 ng/mL	0–1.0 µg/mL	π–π stacking	EIS	This work

4.4. Conclusions

An inkjet-printed aptamer-based biosensor has been developed for the label-free selective detection of lysozyme biomarker. Electrochemical impedance spectroscopy was used as the interrogation method. The selectivity of the sensor was tested against BSA and thrombin and was shown to be selective towards lysozyme. The limit of detection was calculated to be 90 ng/mL. The sensor also demonstrates a reasonable shelf-life of around 21 days at room temperature. Although we have demonstrated the feasibility of inkjet printing-based sensor development for lysozyme detection, our next step in the future work is to further characterize this sensing platform with real physiological samples such as saliva or blood serum to ensure that the results can be replicated. The proposed inkjet-printed biosensor has potential applications in point-of-care diagnostics by enabling low-cost, label-free, fast detection, and on-demand printability so that patient-centered healthcare can be delivered through a disposable disease diagnostic and screening kits.

CHAPTER 5: GRAPHENE FET AS A SENSITIVE DETECTION PLATFORM FOR BIOSENSOR

5.1. Introduction

Lysozyme is a ubiquitous enzyme that is widely available in diverse organisms, such as bacteria, bacteriophages, fungi, plants, and mammals. Being an antimicrobial protein, lysozyme is often called the "body's own antibiotic" [59], [96]. The protein is also extensively exploited in food industries for several purposes such as preserving meat and dairy products, as well as fruits and vegetables. The molecular weight of lysozyme is 14,400 Da with a primary sequence containing 129 amino acids and it has an isoelectric point of 11.0 that causes lysozyme to behave as positively charged at neutral pH [96]. In addition to its extensive use in food industry, lysozyme also plays a vital role as a biomarker for diagnosing various diseases such as breast cancer [98], Alzheimer's [99] and rheumatoid arthritis [100].

In the past, several biosensing techniques have been deployed for effective detection of lysozyme molecules. Some of these methods include chromatographic or antibody-based techniques [124], sensitive colorimetric detection [125], surface plasmon resonance (SPR)-based approach [126] and electrochemical impedance spectroscopy (EIS) measurement [127], [128], to name a few. Among these sensing techniques, field-effect transistor (FET)-based sensing offers several advantages including miniaturization, low cost, and large-scale integration with other sensors as well as rapid detection and high sensitivity [129]–[131].

A typical FET biosensor is comprised of a semiconducting channel contacted between the source and the drain electrodes. Upon adsorption of the biomolecules on the semiconductor surface, a change in the electric field occurs which affects the gate potential of the device resulting in a change in the charge carrier density within the channel of the FET. Such change in the drain current can be conveniently measured and be utilized as an interrogation strategy to probe the adsorbed biomolecules. This type of sensing mechanism has been demonstrated in the past for detecting target analytes in gases, water as well as in human serum [28]–[31], [89]. Two-dimensional (2D) nanomaterials such as such as graphene, MoS_2, WS_2 etc. are particularly attractive as a channel

material for FET-based biosensors due to their planner structure, excellent electrical properties, and high surface area-to-volume ratio. Among several 2D materials graphene has been widely used as a promising FET channel material for various analyte detection due to its superior physical and chemical properties: namely high intrinsic carrier mobility, good biocompatibility, high stability, and flexibility, which are all desirable traits to have for biosensing applications. For example, chemical vapor deposition (CVD)-grown graphene-based FET (GFET) biosensors have been used to detect triphosphate [132] and binding kinetics of DNA hybridization [88]. Similarly, Huang et al. and Chen et al. have successfully demonstrated the detection of bacteria [133] and Ebola antigen [134] using graphene-based FETs. Nonetheless, the detection of protein molecules using FET biosensors is largely limited by the charge screening effects of the non-specifically adsorbed surface molecules from the buffer solution. To overcome this issue, the graphene channel surface is typically modified with target receptors which enable specific binding reaction with the charged target protein molecules in the solution. For example, Ohno et al. reported that in an aptamer-modified GFET, a non-specific binding of the non-target protein molecules was suppressed [135]. However, this technique is still limited for specific detection of small and weakly-charged analytes which do not directly induce detectable changes in surface charge after molecular binding. Moreover, the detection of lysozyme protein via a GFET-based biosensing platform has not yet been demonstrated so far. Therefore, in this work, we describe the selective detection of lysozyme molecules utilizing large area CVD-grown GFET devices prepared by a facile one step transfer process.

The fundamental operating principle of the GFET biosensor is illustrated in Figure 5.1. Figure 5.1(a) depicts the schematic of the liquid-gated GFET device. CVD-grown large area graphene is contacted with source and drain electrodes. Single-stranded probe DNAs (pDNA), which act as target-binding aptamers, are securely anchored onto the graphene surface, via the bifunctional linker 1-pyrenebutyric acid N-hydroxysuccinimide ester (PBASE). A sample ionic buffer solution is dropped on the surface of the GFET channel. Upon applying a gate voltage (V_{GS}), between the gate electrode in the solution and the source electrode of the GFET channel, the electrical double layer (EDL) is formed at the interface between the graphene channel and the electrolyte [136]. This formation of EDL induces image charges in the channel and provides high gate capacitance. This gating capacitance provides the source of electrostatic gating of the GFET. Figure 5.1(b)

demonstrates the I_{DS}-V_{GS} characteristics of the GFET. A typical ambipolar electric field-effect characteristics is expected for the top-gate operation with -1 V ≤ V_{GS} ≤ 1 V. The minimum I_{DS} occur at the charge neutrality point V_{CNP} also known as the Dirac voltage (V_{Dirac}), which signifies the demarcation between the p-type and the n-type conduction of the graphene channel. Therefore, the V_{CNP} represents the doping level in the graphene channel. Since the surface-analyte or analyte-analyte bindings occur in the proximity of the graphene surface, the analyte-analyte bindings can significantly change the doping level in the graphene channel. This change in the doping level results in a detectable shift in V_{CNP} as shown in Figure 5.1b.

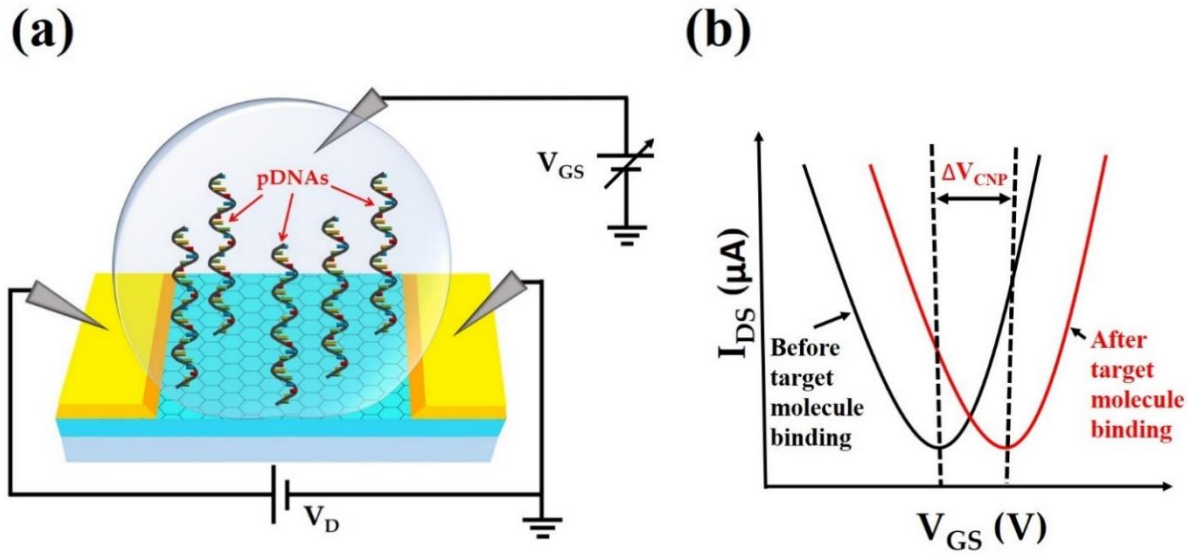

Figure 5.1. (a) Schematic representation of top liquid-gated graphene FET device with anchored pDNAs on the graphene channel surface. (b) I_{DS}-V_{GS} characteristics of graphene FET device before and after target molecule binding resulting in a detectable change in V_{CNP}.

5.2. Materials and Methods

5.2.1. Materials

The amino linker modified anti-lysozyme DNA oligonucleotide (sequence designed by Ellington and co-workers [113] was synthesized by Sigma-Aldrich. The sequence of the oligonucleotide is**:** 5′-amino-C6-ATC AGG GCT AAA GAG TGC AGA GTT ACT TAG-**3′.** Lysozyme protein from chicken egg white was also purchased from Sigma-Aldrich. Protein stock solutions were prepared by dissolving the lyophilites in fresh ultrapure triple-distilled deionized water and stored at -20˚C. The diluted solutions of proteins were prepared in 50 mM Phosphate buffer solution (PBS, pH

7.4). PBS was obtained from Sigma-Aldrich. Tween 20 and 1-pyrenebutyric acid N-hydroxysuccinimide ester (PBASE) were purchased from RPI Research Products International (IL, USA) and Santa Cruz Biotechnology (TX, USA), respectively.

5.2.2. Fabrication of GFET

Figure 5.2 shows the transfer process of large area CVD grown graphene from SiO_2/Si substrate onto the prefabricated 4 independently addressable gold electrodes. The CVD grown graphene sample was purchased from Graphene Supermarket (NY, USA). The transfer process begins with spin coating onto the graphene a support layer of poly (methyl methacrylate) (PMMA) at 3000 RPM followed by immersion into 6 M KOH solution for 30 min at 80^0C. This results in etching of the underlying SiO_2 layer and separation of the top PMMA/graphene bilayer from the substrate. The PMMA-protected graphene layer was then collected on top of the pre-fabricated gold electrodes and dried at room temperature. The electrodes were then immersed into acetone for 12 hours to dissolve the top PMMA layer followed by consecutive washing with ethanol and DI water. Finally, the devices were annealed at 250°C for 2 hr in an Argon-filled chamber to reduce any PMMA residues [137].

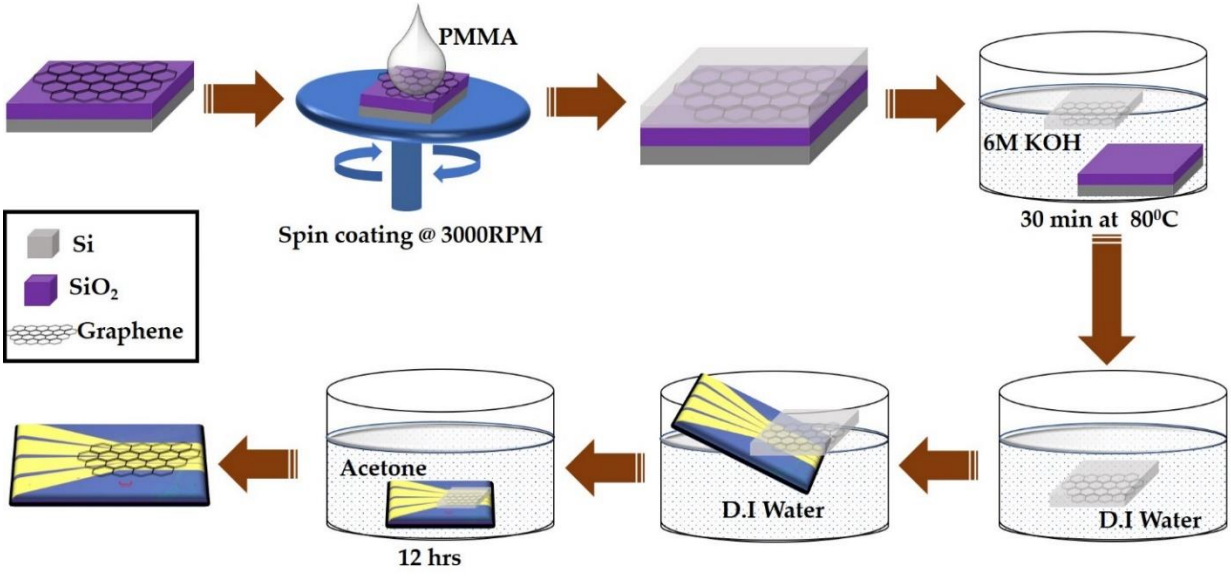

Figure 5.2. Schematic illustration of large area CVD-graphene FET device fabrication process.

5.2.3. Electrical FET measurements

All electrical measurements were carried out using the Keysight precision source/measure unit (B2902A) combined with a probe system (Micromanipulator: 450PM-B). For FET measurements, solution-gate experiments were performed. A constant bias voltage V_{DS} = 100 mV was applied across the drain and the source terminals by connecting the two manipulator needles to the source and the drain electrodes. The gate voltage V_{GS} (-1 V$\leq V_{GS} \leq$ +1 V) is applied by immersing the third manipulator needle into the sample droplet of 0.01× PBS buffer solution placed on top of the GFET devices.

5.2.4. Functionalization of GFET

Immobilization of the pDNAs onto the graphene surface was performed by incubating the graphene chip in the bifunctional linker 1-pyrenebutyric acid N-hydroxysuccinimide ester (PBASE) at 10 mM in dimethyl formamide (DMF) at room temperature for 20 hr. The aromatic pyrenyl group of PBASE binds to the basal plane of graphene through noncovalent $\pi - \pi$ interactions [138]. This was then followed by rinsing the chip sequentially in DMF, ethanol and DI water for 3 min each. In the final step, the chip was incubated with the aminated (5') probe-DNA at 5 µM in 0.01× PBS at room temperature for 12 hr to covalently link the pDNA to the PBASE via an N-hydroxysuccinimide (NHS) crosslinking reaction [139]. To remove the unanchored pDNAs, the chip was successively rinsed with 0.1× PBS and DI water. Following the probe attachment, the chip was treated with 0.1% Tween 20 followed by sequential rinsing in 0.05% Tween 20 and DI water. Finally, the chip was incubated in different concentrations of target proteins in 0.1× PBS for 30 min. This allows lysozyme binding due to the sequence-specific high affinity of the aptamers to lysozyme [23], [54]. Afterward, the chip was rinsed with 0.01× PBS buffer followed by DI water and dried with a compressed air gun before performing the electrical measurements.

5.3. Results and Discussion

5.3.1. The effects of functionalization and DNA immobilization on the FET measurements

For the selective protein detection, the graphene layer is successively functionalized by PBASE and the single-stranded probe DNAs (pDNAs) specifically designed for lysozyme binding [113]. The GFET devices were configured as electrolyte-gated FETs where the graphene is the

conducting channel formed between the source and the drain electrodes on the SiO2/Si substrate as schematically depicted in Figure 5.1(a). PBS solution (0.01×) was used as the top gating dielectric. The pyrene group terminated PBASE is coupled to the graphene surface via the π-π stacking forces [88]. The 5′- amino-modified pDNAs were attached to the amine-reactive succinimide group of PBASE by the conjugation reaction between the amine groups. The $I_{DS}-V_{GS}$ characteristics of the GFET devices were measured sequentially after each functionalization step and exposure to the target lysozyme molecules. The binding of the lysozyme molecules to the pDNAs induces changes in the charge carrier density in the graphene channel. This causes a detectable change in the Dirac voltage (V_{Dirac}) or the charge neutrality point (V_{CNP}) in the $I_{DS}-V_{GS}$ characteristics of the GFET.

Figure 5.3 shows the I_{DS}-V_{GS} characteristics of a GFET device at each stage during the surface modification process. The I_{DS}-V_{GS} characteristics exhibit ambipolar behavior as the gate voltage in the top-gate dielectric (0.01×PBS) changes from -1 V to +1 V similar to previously reported measurements [88]. The V_{CNP} for the unmodified GFET was found to be 203.96 mV. Since the graphene channel is sensitive to any surface adsorptions or modifications, the V_{CNP} was shifted left at 40.8 mV relative to the unmodified graphene channel after the PBASE linker modification. Previously, Wu et al. reported that PBASE modification of graphene causes n-doping in the graphene channel after long incubation in the DMF solvent [140]. Therefore, left shift of V_{CNP} in our experimental results suggests n-doping of the graphene channel. Figure 5.3(c) shows the I_{DS}-V_{GS} characteristics of the GFET after the pDNA attachment. Here, we note that the V_{CNP} further shifted left with respect to that after PBASE modification (Figure 5.3(b)) indicating further n-doping of the graphene channel. It has been widely observed and speculated that the presence of electron rich nucleotide bases in the DNA molecules can cause n-doping effects in carbon nanotubes and graphene [141], [142]. We have further treated the GFET devices with 0.1% Tween 20 solution in deionized water in order to minimize non-specific adsorption. Due to its high affinity with graphene, Tween 20 has been extensively used in the past to deter non-specific binding of proteins as well as to remove non-specifically adsorbed probe DNAs on the graphene [139]. However, the presence of the surfactant adsorbates can effectively dope the graphene channel. Among various surfactants, Tween 20 has been reported to cause n-doping effect on the graphene [143]. Further negative shift of V_{CNP} in the I_{DS}-V_{GS} curve after Tween 20 treatment thus is

consistent with an increased n-doping effect as indicated in Figure 5.3(d). We further notice a small change in the minimum current at V_{CNP} that after each step of functionalization. Due to atomically thin nature, the minimum conductance at the charge neutrality point V_{CNP} in GFET devices are extremely sensitive to several extrinsic factors such as charge impurities, doping density, external ions etc. [144], [145]. Previously it was also reported that the minimum conductance can also be affected by the presence of PBS buffer ions [141]. Thus, we believe that the small changes in the minimum current at V_{CNP} in our GFET devices are caused due to doping effect after surface modification and/or due to the ionic adsorption or desorption effects of the PBS buffer ions.

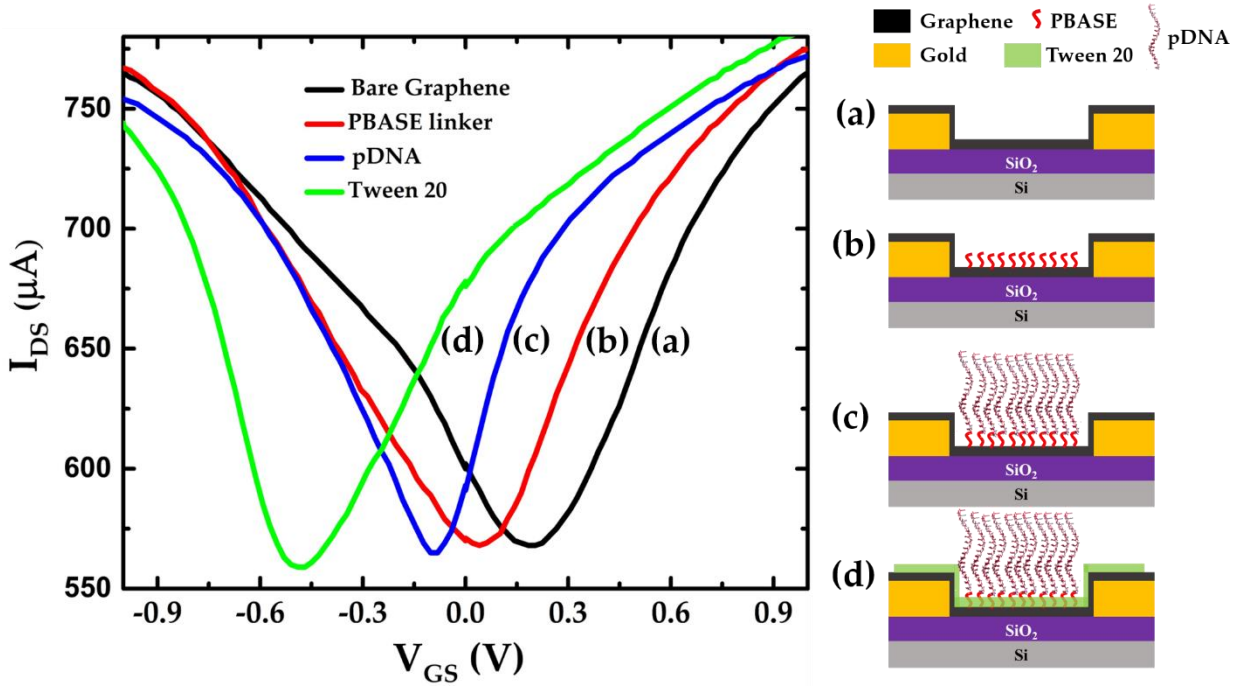

Figure 5.3. I_{DS}-V_{GS} characteristics of the graphene FET device (a) before any surface modification (unmodified graphene); (b) after PBASE functionalization; (c) after attaching single-strand pDNAs to the PBASE linker; and (d) after treating the graphene surface with 0.1% Tween 20.

5.3.2. Concentration Dependent Shift in the Charge Neutrality Point

Figure 5.4(a) shows the I_{DS}-V_{GS} characteristics of the GFET device when exposed to varying concentrations of lysozyme samples. The graphene devices were first incubated in 0.01× PBS buffer solution containing the lysozyme protein for 30 mins followed by a gentle wash in PBS and deionized water before the FET measurements were performed. We found that after exposure to

10 nM lysozyme solution, the V_{CNP} shifted to -449 mV. This results in a positive shift of V_{CNP} of 20.5 mV with respect to the V_{CNP} = -469.5 mV at 0 nM lysozyme. V_{CNP} shifts further right with the increasing lysozyme concentration. The lysozyme binding with the pDNA aptamer (5′-amino-C6-ATC AGG GCT AAA GAG TGC AGA GTT ACT TAG-3′) was previously confirmed by [96]. It was also found that at neutral pH, lysozyme is positively charged with net +8 charges [96], [146]. Therefore, the presence of lysozyme molecules in the proximity of the graphene nanosheet can induce a p-doping effect in the FET channel. Thus, the positive shift of the V_{CNP} can be attributed to the reduction of n-doping effects during the previous functionalization steps. Further, our results suggest a strong correlation between the lysozyme concentration and the degree of the V_{CNP} shift in the right direction: the higher the lysozyme concentration, the further the V_{CNP} shifts to the right. Figure 5.4(b) shows the relative shift of V_{CNP} (ΔV_{CNP}) (with respect to the position of V_{CNP} after exposure to 0 nM lysozyme concentration) after exposing the GFET devices to a series of lysozyme concentrations in the range from 10 nM to 10 µM. From the FET responses, we have found that ΔV_{CNP} increases sharply for the lower concentrations of lysozyme and then gradually reaches saturation at approximately 1µM and beyond.

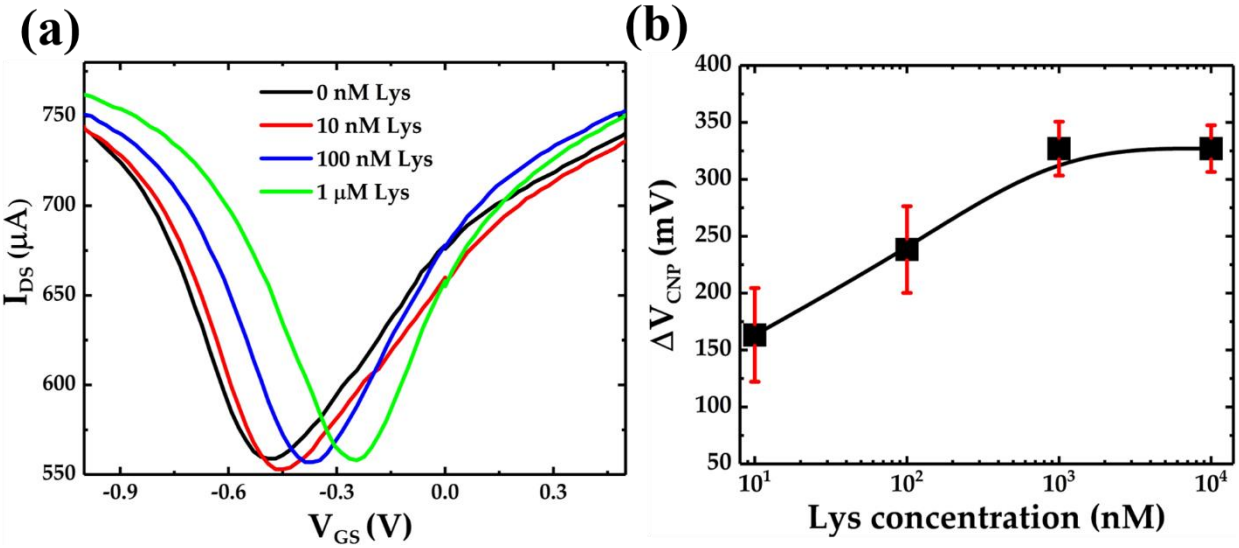

Figure 5.4. (a) I_{DS}-V_{GS} characteristics of the graphene FET-based biosensor device when it is exposed to varying concentrations of lysozyme protein; (b) the calibration curve for the GFET-based biosensor showing ΔVCNP as a function of different concentrations of lysozyme. The sample set is $\boldsymbol{n = 3}$, and the error bar represents 1 standard error.

To further verify the specific lysozyme binding with the pDNA aptamers and subsequently to characterize the selectivity of the GFET biosensor devices, we also prepared GFET devices but without the presence of pDNAs. After successive functionalization with PBASE linker and 0.1% Tween 20, the devices were exposed to 1 μM lysozyme solution. The I_{DS}-V_{GS} curves obtained from the GFET without pDNAs are shown in Figure 5.5(a). Here we found that, after exposure to the lysozyme molecules, there is only a very small shift in V_{CNP} (ΔV_{CNP} =10 mV). This slight change in V_{CNP} can be attributed to the small amounts of non-specific surface adsorptions of the lysozyme proteins on the surface of the graphene sheet. Similarly, we tested pDNA functionalized GFET devices against another non-specific target protein bovine serum albumin (BSA). As expected, due to the lower binding affinity of the pDNA aptamers with BSA, negligible changes in V_{CNP} were observed. Figure 5.5(b) compares the overall sensor responses of the three GFETs, two with the pDNA modification against lysozyme and BSA and one without the presence of pDNAs against the lysozyme (3 separate devices in each group). These results clearly indicate that our graphene-pDNA FET devices can selectively detect lysozyme molecules with significant changes in the charge neutrality point.

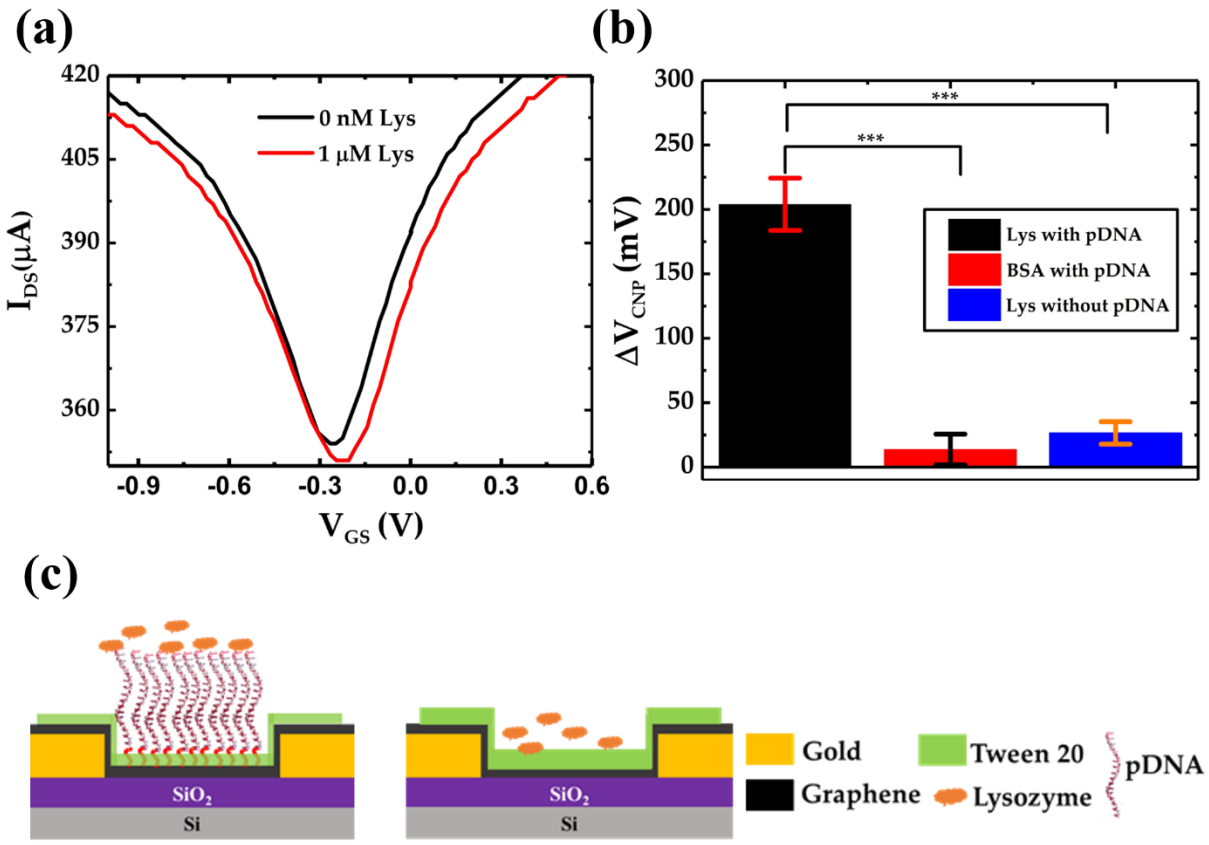

Figure 5.5. (a) I_{DS}-V_{GS} characteristics of graphene-PBASE FET (without pDNA) device before and after exposure to 1µM lysozyme; (b) Comparative bar-chart showing the ΔV_{CNP} of the graphene-PBASE FET devices with the pDNA functionalization after exposure to 1µM lysozyme and 1µM BSA and without pDNA functionalization (n = 3, error bar = 1 standard deviation, paired Student's t-test, ***p < 0.001).); (c) the schematic diagram of the GFET with pDNAs (left) and without pDNAs (right).

5.4. Conclusion

We have presented aptamer-modified large area CVD-grown graphene FET biosensor for the detection of lysozyme protein biomarker. The FET biosensor is sequentially functionalized with PBASE crosslinker, an aptamer specifically designed for the molecular recognition of lysozyme protein and Tween 20 as a blocking agent for minimizing non-specific adsorptions on the graphene channel surface. We have demonstrated that the lysozyme molecules have specifically bound to the surface immobilized aptamers causing a disruption in the charge carrier density. This resulted

in the shifting of the charge neutrality point. Consequently, this change in the charge neutrality point potential of the graphene-FET devices was utilized to quantify the bound lysozyme concentration. The graphene-FET biosensor devices were tested for the detection of the lysozyme biomarker with concentrations ranging from 10 nM to 1 μM in the PBS buffer, demonstrating its capability as a specific biomarker sensor. Furthermore, the dynamic drain-source current measurement with respect to varying lysozyme concentrations would be essential for the demonstration of real-time monitoring of lysozyme molecules. In terms of health diagnostics application, this technology can potentially be used for facile development of large-scale point-of-care testing kits for low-cost and fast-readout disease screening and diagnostics.

CHAPTER 6: GFET-MICROFLUIDICS AS AN INTEGRATED PLATFORM FOR REAL-TIME BIOSENSING

6.1. Introduction

Graphene, a 2D material of one atomic layer thickness, shows a plethora of interesting properties [147]–[154] such as high carrier mobility, large specific surface area, excellent electrical conductivity, planar structure, potential biocompatibility, high stability and flexibility. As a result, graphene materials have been used in many electronic applications including photodetectors [149], [150], capacitors [152] as well as biosensors [153]. Specifically, the utilization of graphene as a conduction channel in a field-effect transistor (FET) has been shown by us and others to have potential for sensitive biodetection [27], [154], [155][29]. To date, there exist many different detection principles in biosensors such as electrochemical impedance spectroscopy [23], [54], [106], high-performance liquid chromatography (HPLC), quartz crystal microbalance (QCM) [156], [157], surface plasmon resonance (SPR) [158] and fluorescence based optical detection [159], [160] to name a few. However, there are some limitations with these techniques such as tedious sample preparation as well as sophisticated and expensive instrumentation with consistent need for trained operators. By contrast, FET-based detection offers a variety of advantages such as high sensitivity, fast detection time, easy integration with the integrated circuit (IC) manufacturing process, miniaturization, low-cost, continuous real-time sensing and label-free detection [129]–[131].

A Graphene FET (GFET) biosensor works either by the electrostatic gating effect or direct charge transfer to graphene, also known as the doping effect, or a combination of both [79], [89]. In the case of electrostatic gating, any adsorption of charged biomolecules on the channel surface causes a change in the electric field that modulates the current through the channel between the source and the drain. By contrast, the doping effect changes the channel conductance as a result of direct charge transfer between graphene and the biomolecule in contact with the graphene surface [141], [161], [162]. The competition between the doping effect and the gating effect determines the

appropriate sensing response. For example, if the doping effect is dominant, the current increases in a p-type semiconducting channel, whereas if the gating effect is dominant, the conduction current decreases [89]. This change in the drain current can be utilized as an interrogation strategy to probe the adsorbed biomolecules. Moreover, the ambipolar transfer (drain current vs. gate voltage) curve of the GFET devices provides an additional sensing mechanism by measuring the surface charge-induced shift in the Dirac voltage (ΔV_{Dirac}) which is defined as the gate voltage at minimum drain current. Hence, the GFET as a biosensing platform has been applied for the detection of various target analytes including antigens, antibodies and charged molecules [27], [32], [79], [82], [83], [88], [163].

Thrombin is an important protein biomarker for a number of diseases as it plays a central role in several cardiovascular diseases and the regulation of tumor growth. It is also responsible for thrombosis and platelet activation and therefore, is involved in many processes such as inflammation and tissue repair at the blood vessel wall [164]. Hence, the selective and sensitive detection of thrombin will be useful in surgical procedures and cardiovascular disease therapy. Moreover, thrombin is positively charged [165], [166] at neutral pH enabling it to be detected on a graphene-based sensing platform. Existing thrombin biosensors commonly use either antibodies or aptamers as the target capture probe to enhance selectivity. Recently, aptamers have become a popular choice of target receptors due to a number of advantages they offer compared to antibodies including shorter length and simpler structure, lower cost, higher stability in harsh environmental conditions, longer shelf-life and mass-producibility. Moreover, they can be selected in-vitro with high affinity for a wide range of analytes ranging from proteins, peptides, amino acids, drugs, metal ions and to even whole cells [9].

Although GFET-based biosensors have been frequently reported [27], [167], [168], when it comes to analyte liquid control, a small volume of sample droplet is often placed over the graphene surface to form a liquid gate which is exposed to the open atmosphere. This type of sensing arrangement makes the sample loading and disposal difficult to control and also makes the device vulnerable to external disturbances such as evaporation. These factors could lead to inaccurate measurements and poor sensing performances. Furthermore, measurements taken during static flow (non-moving fluid) may lead to the mass-transfer limitation in the kinetic binding processes

[169]. Therefore, in efforts to address such challenges, the integration of the GFET device with a microfluidic system is implemented.

The integration of microfluidics to biosensors has emerged as a promising approach in biomedical applications as microfluidics offer numerous advantages over traditional assays. Conceptually, microfluidics is the manipulation of fluids in submillimeter length scale with technologies first developed by the semiconductor industry and later expanded by the micro-electromechanical systems (MEMS) field. Commonly known as miniaturized Total Analysis System (μTAS) or Lab-on-a-Chip (LoC) technologies, microfluidic technologies have been applied to biomedical research in order to (1) streamline complex assay protocols, (2) to reduce the sample volume and detection time substantially, (3) to reduce the cost of reagents while maximizing the information collected, (4) to enable automated measurement with high throughput, (5) to potentially enhance the sensitivity by increasing surface-to-volume ratio, and (6) to enable portability, disposability and real-time detection [170]–[172]. Moreover, integration to microfluidic channels improves the accuracy of measurements by preventing evaporation of buffer solution [173]. To exploit these advantages of the microfluidic technology, the integration of GFET biosensors and microfluidics has been proposed by several research groups. For example, Islam *et al*. have developed a microfluidic GFET biosensor for femtomolar detection of chlorpyrifos [163]. Yang *et al.* have built a microfluidic aptasensor that combines aptamer-based selective analyte enrichment, isocratic elution with GFET-based nanosensing for sensitive and label-free detection of small biomolecules [174]. Saltzgaber *et al.* have demonstrated a large-scale GFET fabrication using a CVD-grown graphene layer and the detection of thrombin biomarkers [175]. Therefore, GFET-based thrombin sensing has the potential to be used as a point-of-care diagnostic device. However, for this to be used reliably in a real-world setting, the GFET must achieve the limit of detection, sensitivity, and analyte selectivity required for clinical use. As an example, thrombin concentration in blood can change from picomolar to micromolar range depending on the health condition. Therefore, a thrombin biosensor must exhibit a limit of detection in the picomolar level as well as a detection range up to a micromolar concentration [176].

In this work, we demonstrate that the aptamer-modified microfluidic GFET platform can selectively detect the thrombin biomarker with a detection limit in the picomolar range. Detailed

analyses of the sensing performances as well as device characterization, including aptamer packing density and continuous real-time sensing, are presented. The GFET was fabricated using the CVD-grown graphene transferred on prefabricated gold electrodes. In contrast to the mechanical exfoliation technique which yields higher quality of graphene, the CVD-based graphene allows large-scale production of graphene with controllable sensing area [148], [177]. Then, the GFET module was integrated with a microfluidic chip to build a miniaturized and portable biosensing module. The detection was performed by measuring the change in the Dirac voltage (ΔV_{Dirac}). Our biosensor was able to detect thrombin with a concentration as low as 2.6 pM (~260 NIH microunits/mL), which is significantly lower than previously reported values [107], [178]. The binding affinity between the aptamer and the thrombin was quantified by calculating the dissociation constant which was confirmed by transient measurements in real-time.

6.2. The Principle of Operation of the Microfluidic GFET-Based Biosensor Platform

The working principle of the microfluidic thrombin biosensor is illustrated in Figure 6.1. Figure 6.1A shows the schematic view of the integrated GFET device where a microfluidic channel with an inlet and an outlet traverses the source, drain and an in-plane gate electrode. Figure 6.1B depicts the three-electrode transistor device setup where the FET measurements were performed by applying a constant drain voltage (V_{DS}) between the source and the drain, whereas a varying voltage (V_{GS}) was applied on the gate. Figure 6.1C shows the mechanism by which target binding and detection is achieved. The Dirac voltage shifts either to the left or right depending on the type and concentration of the adsorbed charged species. If the adsorbed species are at low concentration or weekly charged, doping effect dominates while gating effect becomes dominant at high concentration or strongly charged species [79], [89]. In our experiments, while thrombin, which has an isoelectric point of around 9.5, was weekly and positively charged at pH 7.4 [165], [166], p-type doping was generated in graphene upon binding to the thrombin aptamer. This p-type doping causes the Dirac voltage to shift in the positive direction [88]. By monitoring the shift in the Dirac voltage, the presence of thrombin can be measured quantitatively.

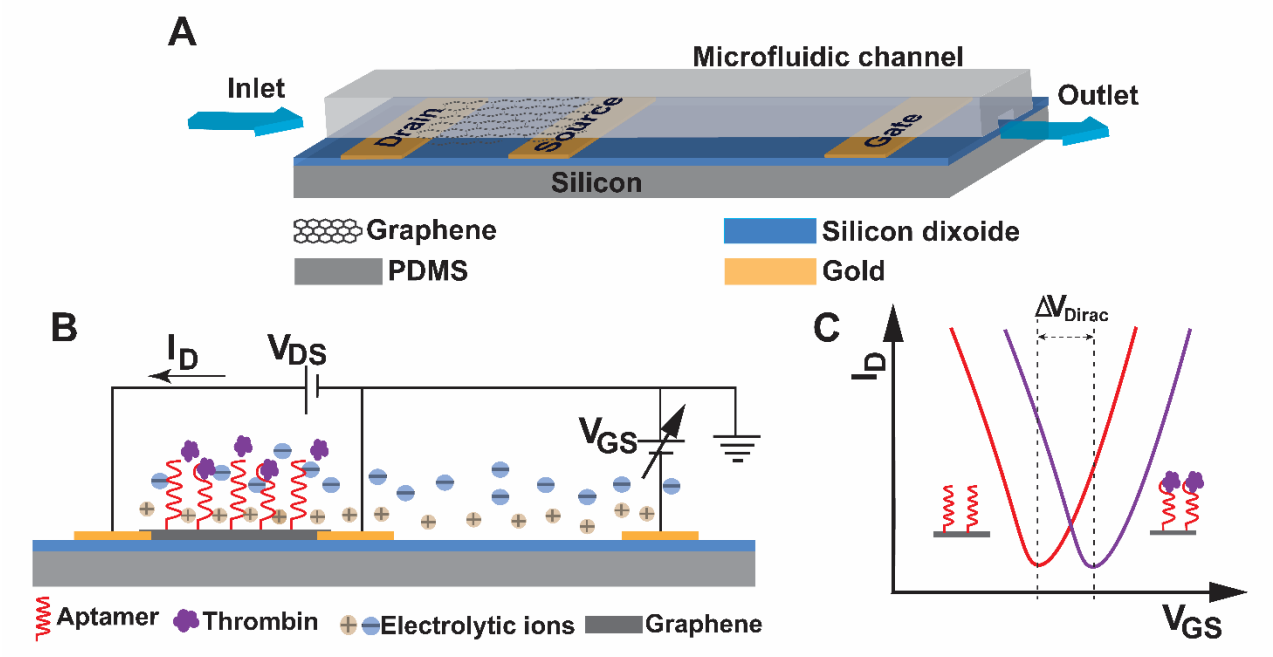

Figure 6.1.Conceptual illustration of the microfluidic GFET biosensor: (A) Schematic illustration of the integrated device; (B) GFET device setup with drain, source, and gate electrodes; and (C) The sensing mechanism based on surface charge-induced Dirac voltage shift (ΔV_{Dirac}) in the FET I_D-V_{GS} transfer characteristics curve.

6.3. Materials and Methods

6.3.1. Materials

The aminated anti-thrombin DNA aptamers and the aminated anti-lysozyme aptamers (for control experiments in Appendix C) were purchased from Sigma-Aldrich. The aptamers were amine-terminated with the following sequence:

Anti-thrombin: 5′–NH_2–$(CH_2)_6$–CCA TCT CCA CTT GGT TGG TGT GGT TGG-3′ [107].

Anti-lysozyme: 5′–NH_2–$(CH_2)_6$–ATC AGG GCT AAA GAG TGC AGA GTT ACT TAG-3′ [113].

Thrombin from human plasma was also purchased from Sigma-Aldrich. The protein stock solutions were prepared by dissolving the lyophilites in deionized water to achieve the different molar concentrations needed for the experiment and were stored at 4ºC. The diluted solutions for sensing experiments were prepared by adding 0.01×PBS (pH: 7.4) to the stock solution. Since GFETs can only observe changes in the charge density that occurs within the distance similar to

the Debye length from the graphene surface, it is critical to ensure that the Debye length be sufficiently large. For an effective GFET-based sensing, the Debye length should theoretically be comparable to the aptamer length [88]. In this work, the estimated length of the anti-thrombin aptamer is approximately 9.1 nm. While 1× PBS has a Debye length of 0.7 nm, the Debye length for 0.01× PBS is 7.3 nm [88], [179]. For this reason, 0.01× PBS was chosen as a running buffer for the electrical measurements. The CVD-grown graphene sheets were purchased from Graphenea Inc. as Easy Transfer Monolayer Graphene on a polymer film.

6.3.2. Device Fabrication, Surface Functionalization, and Measurement Methods

6.3.2.1. Device Fabrication

For the fabrication of the FET devices, gold electrodes for the source, drain and gate contacts were patterned on a SiO_2/Si substrate using conventional microfabrication techniques. Briefly, chromium (Cr, 5 nm) and gold (Au, 60 nm) films were thermally evaporated onto the substrate. Then the source, drain and gate contact regions were formed by standard photolithography, followed by wet chemical etching of Cr/Au layers. The Cr layer was used as an adhesion promoter between Au and SiO_2. After the electrode fabrication, a 5 mm × 5 mm graphene film was transferred onto the electrodes (See Appendix C for details).

The microfluidic channel with a dimension of 30 mm × 600 µm × 100 µm was fabricated with a polydimethylsiloxane (PDMS) block using the cast molding technique [180]. The inlet and the outlet of the channel were formed with metal tubing and the PDMS block was securely clamped to the GFET device. A photograph of the final integrated GFET module is shown in Figure 6.2A. The inlet and outlet of the device were connected with silicone tubes for analyte injection and removal. A motorized syringe pump (Harvard Apparatus) was used for driving the analyte solutions from syringes. Such a setup enables stable flow of the analyte solution and minimizes noise induced by liquid loading processes, as required for real-time, precise measurement of kinetic processes for aptamer-protein binding interaction.

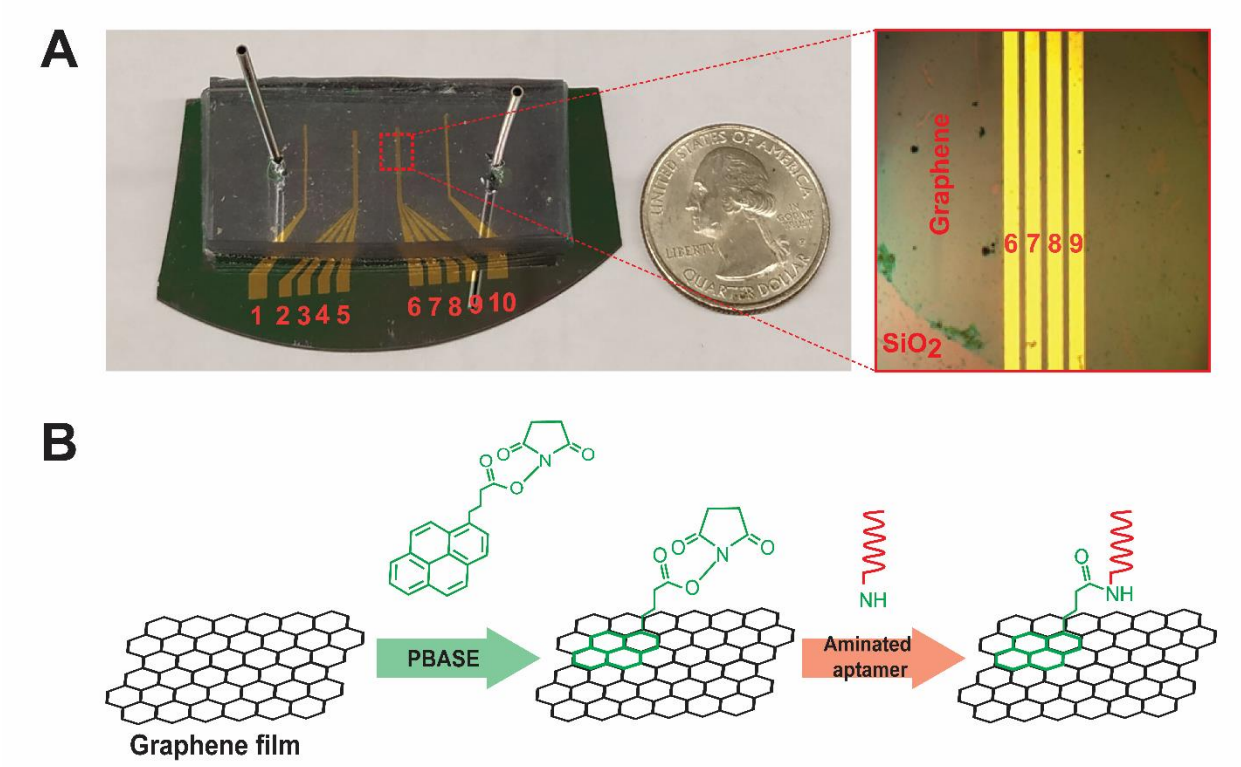

Figure 6.2. Device fabrication and graphene functionalization steps: (A) Photograph of the microfluidic-integrated GFET module (left) and the enlarged view of the source-drain electrodes of the right GFET array (right); and (B) Schematic illustration of the surface functional steps applied to the GFET devices before using it as sensors.

The module consists of two GFET arrays, each array containing 3 GFET devices formed by 4 equally spaced (50 µm gap) gold electrodes (100 µm wide) with two adjacent electrodes acting as the source and the drain. For the 3 GFET devices in each array, one in-plane gold electrode (approximately 6.0 mm spaced apart from the 4 electrodes) serves as the gate. Table C1 summarizes the labeling of the 6 GFET devices in the module.

6.3.2.2. Surface Functionalization

Prior to using the GFET devices as biosensors, the graphene surface was functionalized in several steps as shown in Figure 6.2B. First, the graphene was treated with 10 mM 1-pyrene butyric acid N-hydroxysuccinimide ester (PBASE) solution in dimethyl formamide (DMF) delivered via the microfluidic flow system for 12 hours. The PBASE molecules were non-covalently coupled to the graphene surface by π-π stacking interactions between complementary aromatic rings in the

graphene and the pyrene functional group of PBASE [138]. The fluidic channel was then rinsed by flowing DMF, ethanol and DI water sequentially to remove any unbound PBASE. Next, aptamers were introduced into the channel by flowing a 2 μM aminated (at the 5′-end) target specific aptamer solution and 0.1% (v/v) triethylamine (TEA) for a duration of 12 hours. The aptamers were covalently grafted to the surface bound PBASE molecules via amide bond formation resulting from reaction with the primary amine on the probe aptamer [173], [181]. Successful coupling of PBASE to graphene and aptamer to PBASE was confirmed by Raman, FTIR and UV-Vis analyses.

6.3.2.3. Electrical Measurements

All electrical measurements were performed on a Micromanipulator (450 PM-B) probe station using a PC-based LabVIEW program. A Keysight precision source/measure unit (B2902A) was used for biasing as well as for supplying input voltages and measuring the output currents. The drain-source voltage was maintained at 250 mV for all I_D-V_{GS} transfer curve measurements. The liquid-gate voltage was linearly scanned from 0 V to 2.5 V with a voltage step of 12.5 mV using the gate electrode. During each step, the V_{GS} value was maintained for 1 second to stabilize I_D to ensure reliability of I_D-V_{GS} transfer curves resulting a scan rate of 12.5 mV/s. All the measurements were performed with a fluid flow rate of 20 μl/min. To evaluate the electrochemical effects on the GFET devices, the leakage current at the gate electrode was also measured. The leakage current I_{GS} remained less than 1 μA and thus was considered negligible, as the magnitude of the I_D was in the range of 800 μA.

For the transient measurements of real-time monitoring of the aptamer-protein association and dissociation, I_D was measured by keeping V_{DS} = 0.1 V. The gate source voltage (V_{GS}) was also fixed at a voltage near the charge neutrality point (i.e. V_{Dirac}) such that it locates in the linear region of the I_D-V_{GS} transfer curve yielding a high value of transconductance, g_m (See Figure C2 in Appendix C). Here, the data points were collected once per second. Various concentrations of thrombin were injected at a flow rate of 20 μl/min for 1 hour. Afterward, a 0.01×PBS buffer was flowed for another hour to dissociate and remove the bound protein biomarkers. Since GFETs can only observe changes in the charge density that occurs within the distance similar to the Debye length from the graphene surface, it is critical to ensure that the Debye length be sufficiently large.

6.4. Experimental Results and Discussion

6.4.1. Characterization of the surface functionalization

The interaction between PBASE and graphene via π-π stacking was characterized by Raman spectroscopy. For the sample preparation, the GFET device was functionalized with 10 mM PBASE in dimethyl formamide (DMF) for 2 hours followed by washing with DMF, ethanol and DI water. The Raman spectra for both the bare graphene and the PBASE-treated graphene are presented in Figure 6.3A. The G- and 2D- bands in the spectra indicate the presence of graphene [182]. Moreover, the peak at 1618 cm^{-1} which is attributed to the pyrene group resonance peak due to the π-π stacking interaction [79], [88] between the aromatic rings of the pyrene group of PBASE and the basal plane of graphene which confirms the coupling of PBASE to graphene.

To characterize the crosslinking of aminated aptamers with PBASE, both the aptamers and PBASE were reacted in a 3:2 mixture of tetrahydrofuran (THF) and PBS buffer. The aptamer-grafted PBASE was purified by column chromatography and was allowed to dry an oven at 45ºC for 8 h. The FTIR spectra of both dried PBASE-aptamer and pure PBASE powder are presented in Figure 6.3B where the presence of a strong peak at 1653 cm^{-1} (C=O stretching in the amide I) and the broad stretching vibration peak around 3300 – 3550 cm^{-1} (N-H from the amide, O-H solely on the DNA) confirm the amide bond formation [183]. By contrast, the corresponding peak for C=O in PBASE appears at 1725 cm^{-1} and the absorption peaks at 1785 cm^{-1} and 1816 cm^{-1} are related to the symmetric and asymmetric stretching vibration of the two C=O groups in the imide, while the stretching peak for C-N in the imide appears at 1375 cm^{-1} .

After the PBASE and aptamer crosslinking was confirmed, the PBASE functionalized GFET device was exposed to a 2 μM aminated (at the 5′end) target specific aptamer solution for 12 hours. The sample was then washed with DI water and dried followed by UV-Vis spectroscopy measurements. The UV-Vis absorption spectroscopy is shown in Figure 6.3C where the absorption peak at around λ = 260 nm is a characteristic peak of the DNA oligonucleotides. This proves successful immobilization of the aptamer receptor in the graphene channel.

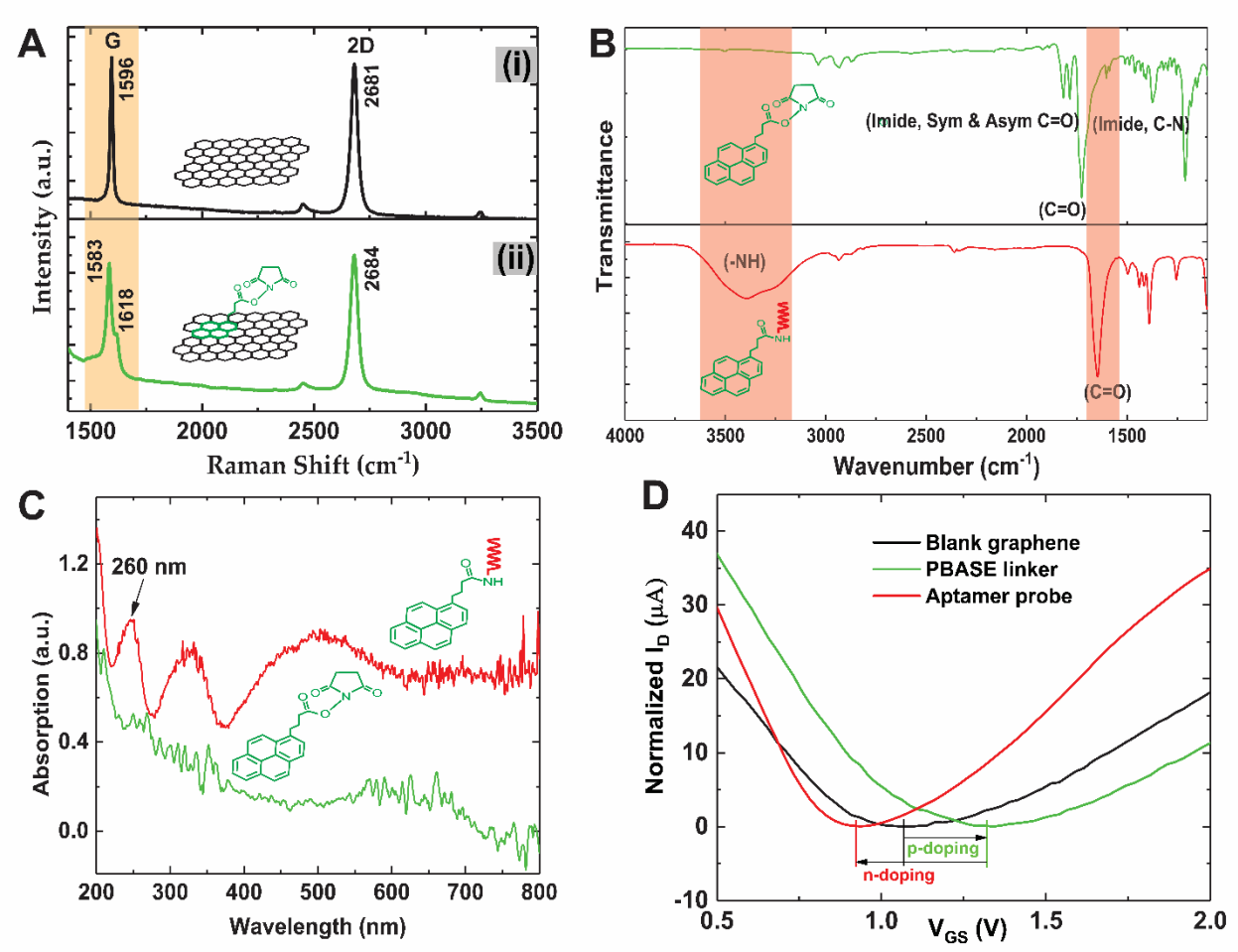

Figure 6.3. Characterization of linking of aptamer to GFET: (A) Raman spectrum (excitation by 532 nm) showing the coupling of PBASE to graphene; (B) FTIR spectrum showing the covalent binding of aminated aptamer with PBASE; (C) UV-visible spectrum showing the final aptamer crosslinking to PBASE/graphene; and (D) I_D-V_{GS} transfer characteristics showing the effects of surface functionalization of the graphene.

We further investigated the functionalization-induced doping by measuring the I_D-V_{GS} transfer curves of the microfluidic-GFET device before and after PBASE coupling. As can be seen from Figure 6.3D, immobilizing PBASE linker to graphene causes the Dirac voltage to shift right. This shift in the positive direction can be explained by the p-type doping effect due to the charge transfer between PBASE and graphene [79], [88]. It is important to note that while the pyrene group of PBASE is electron-rich and not expected to induce p-type doping to the graphene, the carbonyl group of PBASE is an electron-withdrawing group that can cause electron transfer from graphene

to the linker molecule [173], [184]. After PBASE functionalization, the devices were further modified with DNA-based aptamer which caused the Dirac voltage to shift left with respect to the position after the PBASE modification step. This is due to the n-type doping of graphene channel by the electron rich nucleotide bases of the DNA aptamers acting as electron donors when interacting with graphene [141], [142]. Using the shift in Dirac voltage, the aptamer density was estimated to be 1.427×10^{11} /cm^2 which is equivalent to 23.2 nm aptamer probe spacing (See the Supplementary Information for the detailed calculation).

6.4.2. The FET-Based Sensing Experiments

6.4.2.1. Control Experiments

To examine the inertness of the bare graphene to thrombin, a set of control experiments were performed by exposing bare graphene to thrombin solution of various concentrations. As shown in Figure C1(A) in Appendix C, no significant shift in the Dirac voltage is observed indicating a non-responsive behavior of bare unmodified graphene to thrombin. We also performed another set of control experiments to examine the adsorption behavior of thrombin on GFET device modified with a different aptamer sequence. In this case, the graphene was modified with anti-lysozyme aptamers and were exposed to different concentrations of thrombin solutions. The measured transfer curves are presented in Figure C1 (B) which shows that there is no significant shift in the Dirac voltage, indicating negligible non-specific adsorption of thrombin protein during the sample flow.

6.4.2.2. The Effects of Analyte Concentration on the Dirac Voltage Shift

Following the functionalization and aptamer immobilization, the GFET devices were exposed to different concentrations of thrombin by delivering them through the microfluidic channel at 20 µl/min for 45 minutes each. Each sample exposure was followed by a washing step with 0.01×PBS buffer for another 45 minutes for sensor regeneration. Figure 6.4A shows the I_D-V_{GS} characteristics of the developed biosensor after exposure to different concentrations of thrombin protein. Exposure to 1 pM of thrombin caused a Dirac voltage shift (ΔV_{Dirac}) of 101 mV in the positive direction with respect to V_{Dirac} = 934.4 mV at 0 pM thrombin. With increasing concentrations of the thrombin biomarker, V_{Dirac} continues to shift further to the right until it begins to saturate at approximately 100 nM. This result is consistent with the cationic nature of thrombin protein at

neutral pH [165], [166]. Upon binding of the thrombin to the anti-thrombin aptamer, the net positive charge of the protein causes p-type doping of the graphene which explains the right-shift of the Dirac voltage [27]. Figure 6.4B depicts the concentration dependent calibration curve obtained by plotting the Dirac voltage shift (ΔV_{Dirac}) relative to the zero concentration of the analyte (0 pM Thr). As indicated by the error bars in Figure 6.4B, fabricating reproducible GFET devices is a challenge. This is primarily due to the variations in the graphene sheet in terms of the graphene channel area as well as the defects and grain boundaries which can all have a significant impact on the electronic properties of the film. However, the device reproducibility can be improved by directly growing and patterning the graphene on the substrate rather than transferring the film manually.

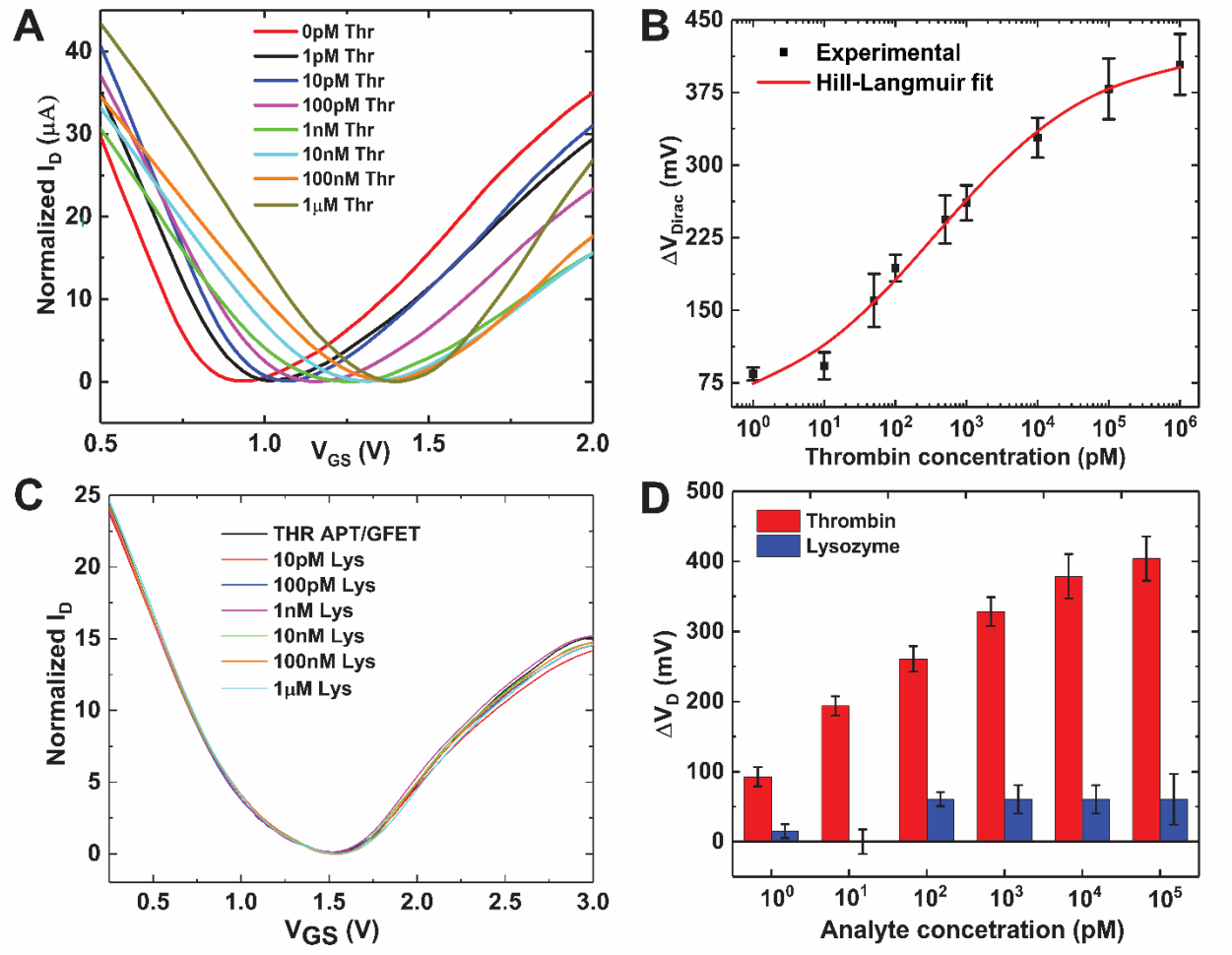

Figure 6.4. Performance of the microfluidic-integrated GFET biosensor: (A) I_D-V_{GS} transfer characteristics of the GFET biosensor after exposure to different concentrations of thrombin protein; (B) Concentration dependent calibration curve of the biosensor and its Hill-Langmuir fit

(R^2=99.25%). The sample set is $n = 3$ and the error bar represents 1 standard error; (C) I_D-V_{GS} transfer characteristics of the GFET thrombin biosensor after exposure to different concentrations of lysozyme protein; and (D) Comparative bar chart showing the ΔV_{Dirac} of the GFET thrombin sensor after exposure to different concentration of thrombin and lysozyme protein.

The calibration curve profile is best fitted by a model adapted from the Hill-Langmuir equation that describes the equilibrium binding of a ligand by a receptor [137], [185], [186]:

$$\Delta V_{Dirac} = \frac{V_0 + V_m \left(\frac{x}{K_D}\right)^n}{1 + \left(\frac{x}{K_D}\right)^n}$$

where V_0 is the estimated minimum response with all binding sites empty, V_m is the estimated maximum response with all the binding sites occupied, x is the target concentration, K_D is the effective dissociation constant that represents the concentration at which half of the available binding sites are occupied, and n represents the Hill coefficient.

The best fit (R^2 = 0.9925) values are summarized in Table 6.1, where the Hill coefficient value of n = 0.386 being less than 1 indicates a negative cooperativity in the binding of thrombin to the GFET biosensor that may be due to the protein-protein interactions upon binding or increased charge carrier scattering with increased ligand binding [137], [154]. The best fit value of K_D = 375.8 $\pm$ 165.6 pM is in the similar range as reported previously [175], [187]. Based on the obtained calibration curve, the calculated limit of detection (LOD) of our sensor is 2.6 pM (See Appendix C for details).

Table 6.1. Summary of the Hill-Langmuir fitting parameters of the voltage calibration curve.

Hill-Langmuir parameters	**Value**	**Error**
$\boldsymbol{V_0}$	39.2 mV	±30.6 mV
$\boldsymbol{V_m}$	418.2 mV	±20.8mV
$\boldsymbol{K_D}$	375.8 pM	±165.6 pM
$\boldsymbol{n}$	0.386	±0.081

6.4.2.3. Selectivity of the GFET Biosensor

The selectivity of the biosensor was tested against another common protein biomarker lysozyme. For this experiment, the GFET device functionalized with thrombin-binding aptamer was exposed to various concentrations (1, 10, 100, and 1000 nM) of lysozyme in 0.01× PBS buffer through the microchannel and incubated for 45 minutes. The measured I_D-V_{GS} characteristic curves are presented in Figure 6.4C. A comparative bar chart showing the Dirac voltage shift for both thrombin and lysozyme is shown in Figure 6.4D. Exposure to high concentrations of lysozyme does cause some degree of Dirac voltage shift possibly due to the protein either nonspecifically binding to the anti-thrombin aptamer or directly adsorbing to the graphene surface. In either case, the positively charged lysozyme [96] affects the doping level of the GFET (i.e. p-type doping) in the same way the thrombin does to the device. However, its effect is relatively small compared to that of thrombin of the same concentration, as shown in the chart.

6.4.2.4. Real-Time and Transient Measurements

The transient FET measurements were performed on the device to monitor the protein-aptamer interaction in real-time. Various concentrations (0 pM – 1 µM) of thrombin in 0.01× PBS were added to the sensor for 1 hour. To check the selectivity of the sensor, the GFET was also tested against a high concentration (1µM) of lysozyme for the same amount of time period. The signal I_D (t) was recorded while keeping V_{GS} and V_{DS} constant. The time-dependent measurements are shown in Figure 6.5A. A gradually drifting background signal has been subtracted from I_D (t). It can be seen that for each concentration of thrombin exposure, I_D (t) follows an exponentially decreasing profile until PBS washing buffer was introduced to dissociate and remove the bound thrombin. The figure also shows that there is minimal change in I_D when exposed to lysozyme. Figure 6.5B shows the enlarged view of the association and dissociation curves for the 1µM thrombin concentration. After analyte injection into the microfluidic device, it took approximately 15 minutes for I_D (t) to respond due to the time required for the liquid to reach the GFET. As soon as the analyte reaches the sensor, target binding occurs and the signal drops exponentially until it reaches a steady-state approximately after 35 minutes. The amount of drop (ΔI_D) in the drain-source current is plotted against the thrombin concentrations that result in the current calibration curve in Figure C3 in the Appendix C. Table C2 in Appendix C summarizes the best fit (R^2 = 0.9778) values of the Hill-Langmuir fitting parameters of the current calibration curve. The

corresponding dissociation constant is found to be K_D = 731.7 pM which is comparable to the value obtained from the voltage calibration curve.

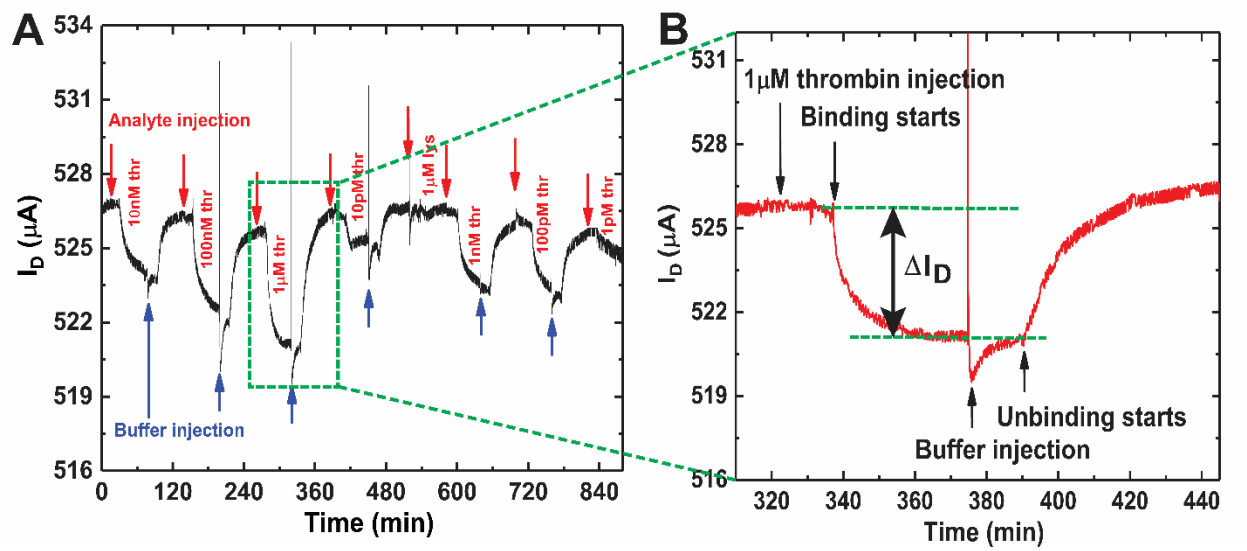

Figure 6.5. (A) The continuous real-time measurements of the GFET biosensor. The plot depicts the transient measurement of the microfluidic-integrated GFET module biosensor. The liquid gate was fixed at V_{GS} = 0.75 V while the drain-source voltage was maintained at V_{DS} = 100 mV. A constant flow rate of 20 µl/min was maintained throughout the experiment. Data points were collected every 1 second. A baseline drift of 9.378 nA/min has been subtracted from the curve. Sharp spikes around the introduction of thrombin and the PBS buffer are noises associated with switching of the syringes; and (B) Binding and unbinding process for the thrombin with concentration of 1µM.

The selectivity of the sensor towards thrombin was again confirmed from this experiment as introducing 1 µM lysozyme did not cause any significant change to the I_D (t) signal. The sensor can also be regenerated by simply rinsing with PBS buffer which has been confirmed by the unbinding process and the baseline curve returning to the initial value to approximately 525 µA shown in Figure 6.5B.

When recording the I_D (t) measurement, the raw data exhibits a gradual upward drift over time. This slow increase in the baseline current can be explained by the possible dissociation of pyrene anchors from the graphene surface resulting in a loss of aptamers from the GFET [175]. This loss of aptamers, although small in quantity, could shift the Dirac point in a positive direction causing

I_D (t) to rise (decrease of n-type doping) over time. However, this drift can be modeled using the formula: $g_m = \frac{\Delta I_D}{\Delta V_{GS}}$. In our devices, the measured baseline drift was $\Delta I_D = 9.378$ nA/min which corresponds to a ΔV_{GS} changing at a rate of 202 μV/min. At this rate, 50% of the aptamer coating would dissociate after approximately 10 hours (i.e. the time to shift $\Delta V_{GS} = 117$ mV) which is similar to the previously reported value [175]. The measurements in Figure 5 are the result after baseline correction by subtracting the current drift.

6.5. Conclusion

In conclusion, in this work, we have developed a microfluidic-integrated miniaturized GFET biosensor module for selective detection of thrombin biomarker. Thrombin is often used as a model protein in protein biosensing. It is also known for its several biomedical significances such as its critical role in hemostasis and thrombosis, involvement in several cardiovascular diseases and regulation of tumor growth. The binding affinity of the protein-aptamer interaction was quantified with a dissociation constant value of 375.8 pM which was further confirmed by real-time thrombin detection measurements. We also characterized the functionalization of aptamers on the GFET surface by Raman, UV-Vis and FTIR spectroscopy techniques. The sensor is able to detect thrombin as low as 2.6 pM.

CHAPTER 7: A FLEXIBLE PRINTED GFET FOR REAL-TIME MONITORING OF IL-6 PROTEIN

7.1. Introduction

Graphene FET-based devices have proven to be very convenient for highly sensitive detection of biomarkers as described in Chapter 5 and 6. Moreover, due to the planar structure with flexibility, GFETs are highly suitable for flexible biosensors. In this chapter, I will describe how GFETs can be fabricated on polymer based flexible substrates and demonstrate real-time detection of IL-6 protein, a well-known cytokine and a biomarker for immune responses, as a representative target analyte [188], [189].

7.2. Flexible GFETs in wearable electronics

Wearable electronics are usually flexible devices that can be worn or mated with human skin to continuously and closely monitor an individual's activities, without interrupting or limiting the user's daily routine. Therefore, wearable biosensors could enable real-time continuous monitoring of an individual's physiological biomarkers, that are essential to the realization of personalized medicine for a variety of chronic and acute diseases [190], [191]. Essentially, wearable biosensors should be designed in a manner so that it avoids the painful and risky blood sampling procedures and can easily blend in with the user's daily routine. This can be accomplished by providing a direct contact between the biosensing platform and the biofluids (sweat, tears, saliva and interstitial fluid) without inducing discomfort to the users [192].

Wearable biosensors have garnered substantial interest over the past decade, mainly concentrated in the healthcare industry and are only capable of tracking an individual's physical activities and

vital signs (such as heart rate, blood pressure, skin temperature, etc.) and fail to provide insight into the user's health state at molecular levels. However, chemical analysis of biofluids could enable such insight because it contains physiologically and metabolically rich information that can be retrieved non-invasively. Sweat analysis is currently used for applications such as disease diagnosis, drug abuse detection, and athletic performance optimization [190], [191]. It is the most easily accessible biofluid for chemical sensing applications since sweat glands are distributed across the entire body, with more than 100 glands/cm^2 [192]. It is rich in physiological data, containing electrolytes (such as sodium and potassium ions) and metabolites (such as lactate and glucose). Under most climate conditions, an average adult human secretes between 500 to 700 ml of sweat per day [193]. Therefore, sweat-based sensors can be applied in a variety of biomedical and fitness applications.

Wang et al. from the Lin group of Columbia University developed an ultra-flexible and stretchable GFET-based aptasensor for sensitive detection of TNF-α biomarker [194]. Presented in Figure 7.1, this flexible GFET biosensor, which was built on Mylar substrate, demonstrated a high level of mechanical flexibility and durability, as well as highly consistent electrical properties and biomarker responses. However, the electrodes were deposited with metal evaporation and patterned with conventional photolithography, thus making the fabrication process expensive and complex. Moreover, sophisticated cleanroom environment and trained personnel are required for the microfabrication of the GFET devices. All these issues can be addressed by printing the electrodes using commercially available silver ink. Printing offers numerous advantages compared to the microfabrication, such as flexibility and versatility in patterning, low-cost, rapid and mass producibility as well as less wastage. Therefore, in this work, a benchtop PCB printer will be used

to print commercially available conductive silver ink on a flexible substrate and transfer graphene on this printed electrode resulting in a printed flexible GFET. With this printed flexible GFET, real-time detection of IL-6 protein biomarker will be demonstrated.

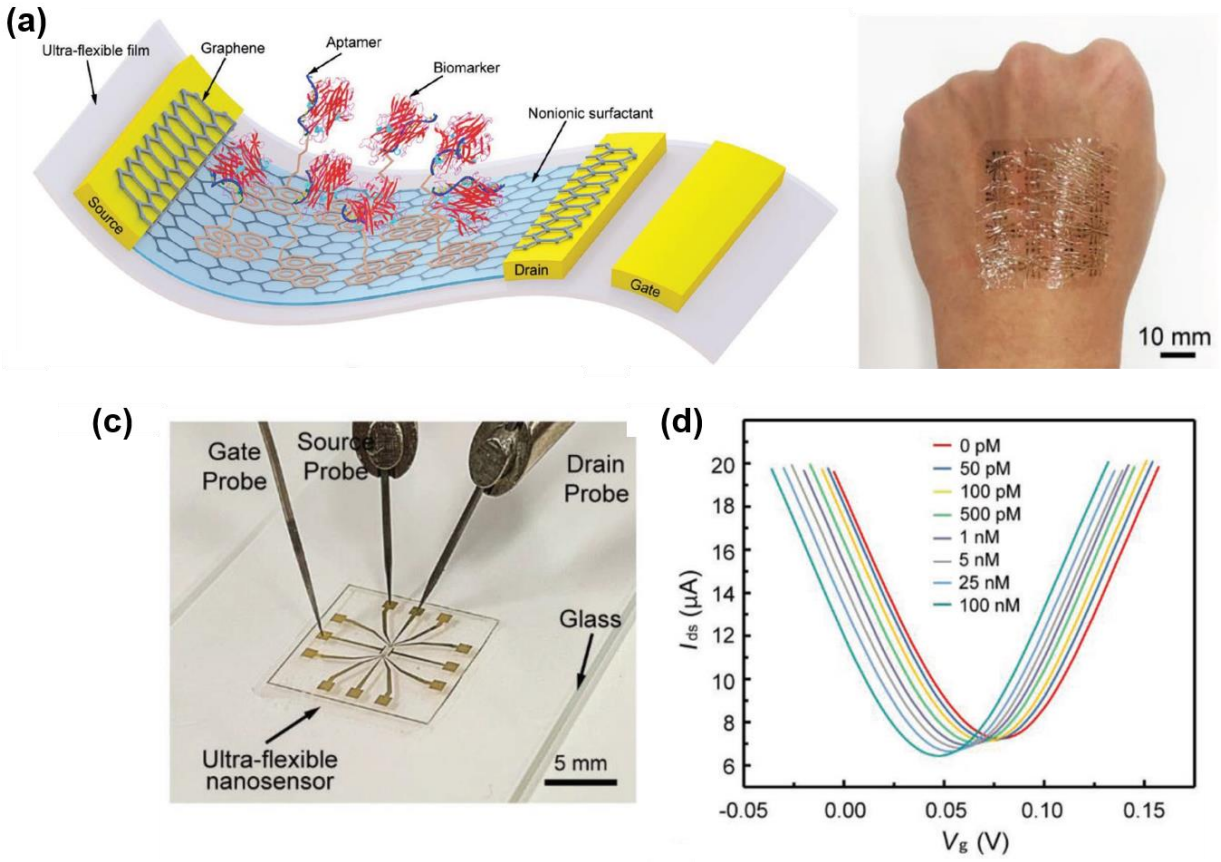

Figure 7.1. Ultra-flexible and stretchable GFET biosensor on flexible substrate. (a) Schematic of the flexible device; (b) photographs of the ultra-flexible sensor conformably mounted on human hand; (c) photograph of the nanosensor placed on a glass slide for biomarker detection; and (d) Transfer characteristic curves measured when the nanosensor was exposed to TNF-α solution with different concentrations. Reprinted from [194].

7.3. Kapton® as flexible substrate for GFETs

Materials properties that are critical for a substrate in MEMS-based applications are the chemical and thermal stability, flexibility, as well as vacuum compatibility [195], [196]. Device fabrication

processes, such as physical deposition and etching require flexible substrate to experience high temperature stress and vacuum. Cleaning agents such as acetone, isopropyl alcohol, or organic solvents such as dimethyl formamide (DMF) are often used in photolithography and surface functionalization of graphene FET based devices. Commonly used polymers used as flexible substrates, such as poly(dimethylsiloxane) (PDMS), polyethylene terephthalate (PET) or polyethylene naphthalate (PEN) can be vulnerable to these solvents. Polyimides can address these issues due to their superior properties [196] as described below:

- High thermal stability (up to 300ºC)
- Highly chemical stability against commonly used solvents in the device processing
- Low outgassing under high vacuum
- Young's modulus of 4GPa

Among other polyimides, Kapton® is selected as the flexible substrate because of its wide availability. It is commercially available both in roll and in sheet format with standard thickness of 0.0254 to 0.127 mm as seen in Figure 7.2.

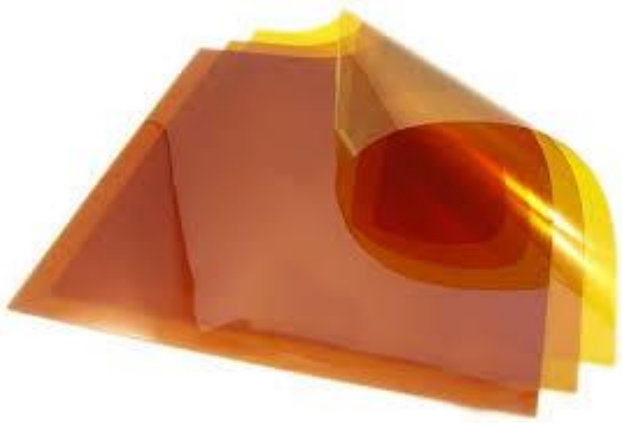

Figure 7.2. Kapton® as a flexible substrate.

7.4. Materials and Methods

7.4.1. Materials

The aminated aptamers having the specific affinity to mouse IL-6 (#ATW0077, K_D=5.4 nM) and the resuspension buffer were purchased from Base Pair Biotechnologies, Inc. (TX, USA). The aptamer's affinity has been thoroughly characterized by the manufacturer and is shown to be

specific toward IL-6 proteins. IL-6 recombinant mouse protein was purchased from BioLegend (San Diego, CA). PBASE (1-pyrenebutyric acid N-hydroxysuccinimide ester) was purchased from Santa Cruz Biotechnology (TX, USA). Kapton® film (size: 12 inches × 12 inches, thickness: 1 mil) was purchased from Amazon.com, Inc.

7.4.2. Manufacturing of the printed GFET

The manufacturing of the printed GFET is presented in Figure 7.3. the manufacturing of the printed GFET starts with designing the electrode pattern in an open-source CAD software KiCAD and then printing it on a Kapton® film using Voltera V-One printer. Conductive silver ink was used for printing the electrodes. Following printing, the printed film was sintered on a hotplate in order to improve the adhesion between the ink and the film. Once the printed electrodes are sintered,

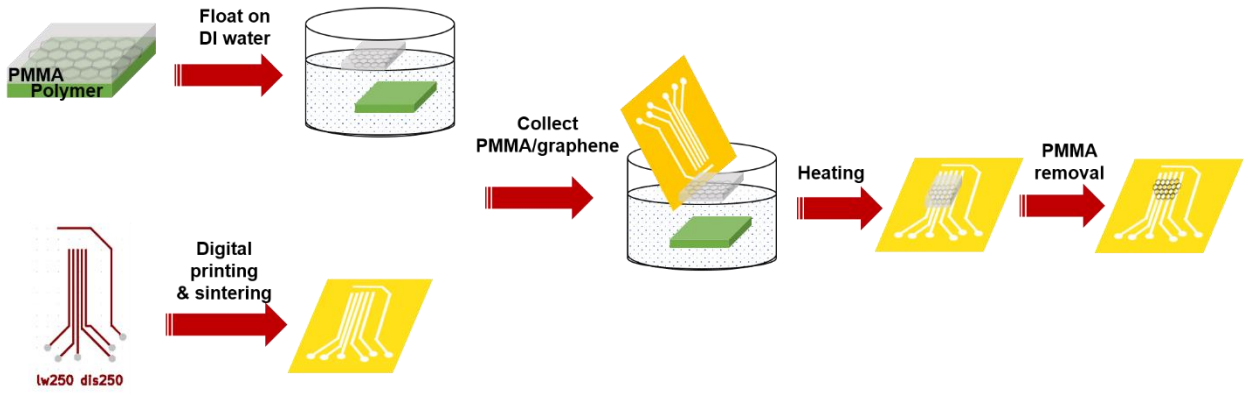

Figure 7.3. Manufacturing of printed GFET on Kapton® substrate.

a monolayer graphene film was transferred on the electrodes using a method known as “fishing.” The transfer method was described in Figure 5.2 of Chapter 5. After the transfer, the protective PMMA layer on top of graphene was removed by acetone and ethanol. The printed GFET device on Kapton film with graphene transferred on it is shown in Figure 7.4. A PDMS microfluidic channel was then integrated on the printed GFET for enabling real-time sensing.

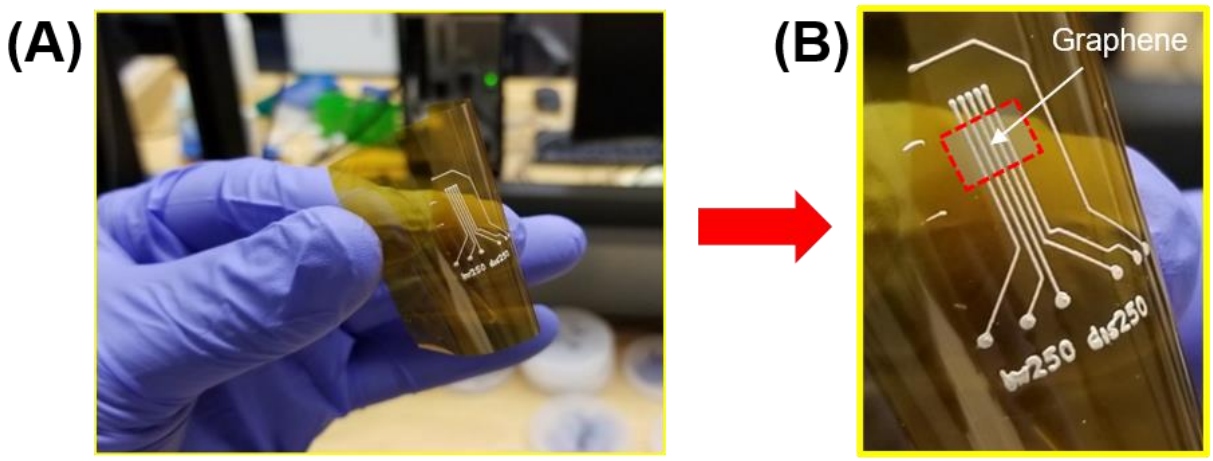

Figure 7.4. Printed GFET on Kapton®: (A) photograph showing the flexibility of the printed GFET, and (B) enlarged view particularly showing the graphene monolayer transferred on the electrodes.

7.4.3. Functionalization of the printed GFET

After manufacturing, the printed GFETs were functionalized with target (IL-6) specific aptamers for using them as sensors. The functionalization process is schematically illustrated in Figure 7.5 where amine-linked aptamers are anchored on GFET using the PBASE linker via the well-known NHS crosslinking reaction. The details have been described in Chapter 6.

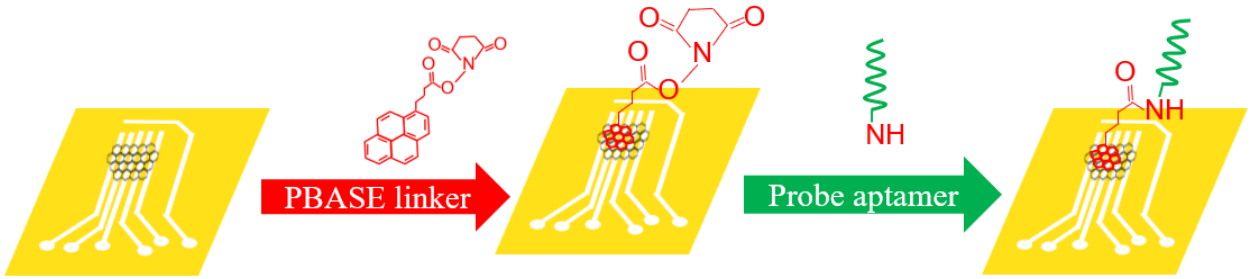

Figure 7.5. Schematic showing the functionalization steps of the printed GFET.

7.5. Experimental Results and Discussion

7.5.1. Characterization of the surface functionalization

The functionalization steps were characterized electrically using the GFET measurements. The results are presented in Figure 7.6, where the relative shift of the Dirac voltage follows the same

trend as our previous GFET devices on solid (SiO_2/Si) substrate described in Chapter 6. This demonstrates a successful functionalization of aptamers on the printed GFET on Kapton®.

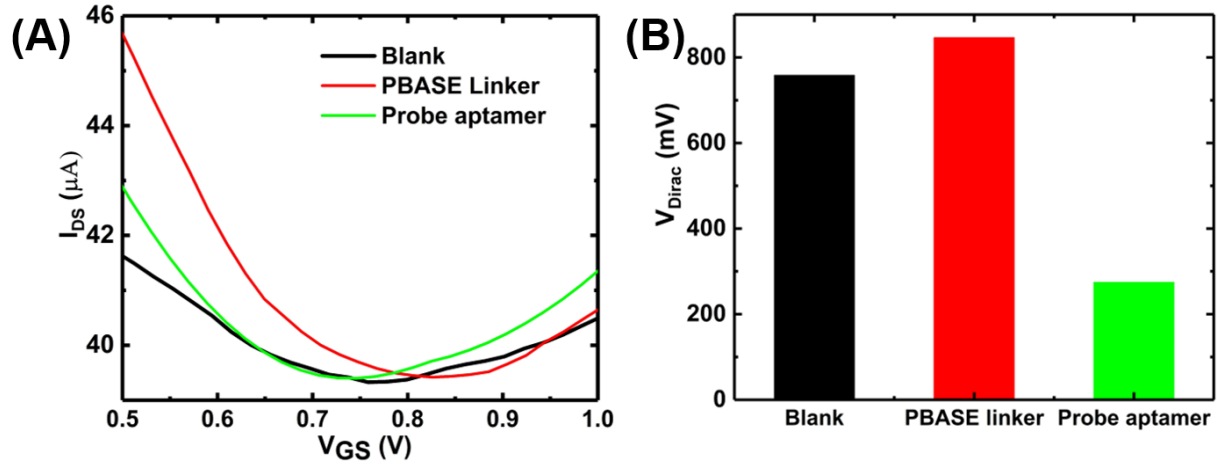

Figure 7.6. Electrical characterization of the GFET functionalization: (A) I_D-V_{GS} transfer characteristics curve at each functionalization strep, and (B) the bar graph showing the values of V_{Dirac} for each functionalization step.

7.5.2. Real-time sensing of IL-6 using printed GFET

After successful functionalization of the printed Kapton GFETs (k-GFETs), they were utilized for real-time sensing of IL-6 protein. For the real-time measurement, the GFET was biased at V_{GS} = 100 mV and V_{DS} = 750 mV. The binding between the aptamers and the proteins was monitored by recording the changes in I_{DS} while different concentrations (1, 10, 100 nM) of IL-6 protein in 0.01x PBS+1mM $MgCl_2$ were added to the sensor for 10 min each followed by a buffer incubation step for sensor regeneration. The real-time measurements are presented in Figure 7.7. It can be seen from Figure 7.7 that upon exposure of IL-6 protein, I_{DS} decreases due to the association of the aptamers and the target proteins. Moreover, when the buffer is introduced, I_{DS} returns close to its initial level due to the dissociation of the aptamer-protein complex.

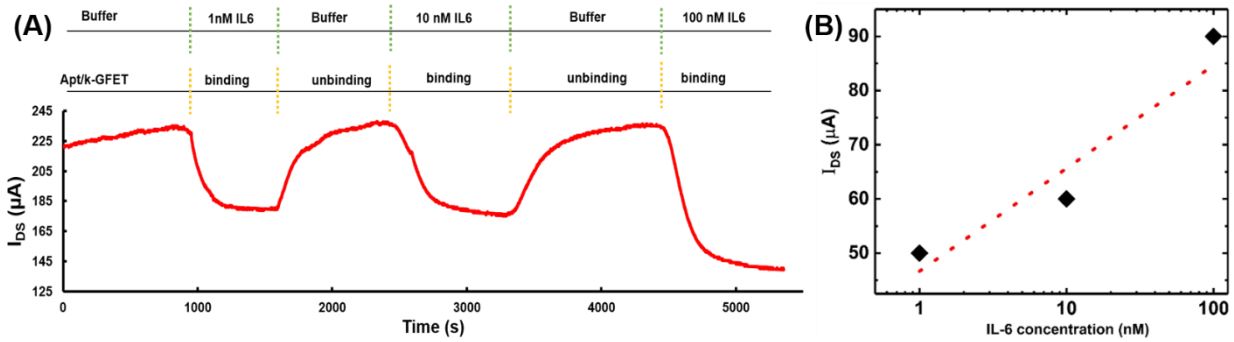

Figure 7.7. Real-time monitoring of IL-6 buffer: (A) transient measurements showing binding and unbinding of aptamer-target, and (B) concentration dependent calibration curve.

7.6. Conclusion

In this chapter, the feasibility of using Kapton® substrate based printed GFET for sensing of protein biomarkers has been demonstrated. The electrodes were printed using a benchtop PCB printer which makes the production easy, rapid, and low-cost enabling their use in point-of-care or low-resources setting. Moreover, the use of Kapton® makes it compatible with wearable electronics applications where flexibility is a critical component in the device design.

CHAPTER 8: AN ORGANIC SOLVENT-FREE APTAMER IMMOBLIZATION METHOD ON GFET PLATFORM

8.1. Introduction

In recent years, graphene-based field-effect transistors (GFETs) and their uses as sensing platforms have been greatly successful in developing various microfluidic and lab-on-a-chip-based biosensors [197], [198]. Their effectiveness as a biosensing platform can be attributed to their high carrier mobility, sensitivity to molecules, and 2-dimensional geometry resulting in ultra-sensitivity and easy integration capability [199]–[201]. A GFET works based on the modulation of the graphene channel conductance (i.e., the channel current) between the source and the drain upon the application of an external electric field through the gate electrode. This principle can be exploited as a method for sensing of biomolecules since charged molecules that are in close contact with graphene (within the Debye length) will cause a change in the electric field leading to a modulation in the drain-source current (I_{DS}) of the GFET. A significant difference between GFETs and other conventional FETs is their ambipolar transfer ($I_{DS} - V_{GS}$) curve which causes a minimum channel current at the Dirac voltage also known as the charged neutrality point (V_{CNP}). Any change in the electric field induced by the adsorption of the charged molecules at the graphene surface essentially causes a shift in the charge neutrality point enabling GFETs to be used for ultra-sensitive detection of the target biomolecules [200], [202].

To enhance selectivity in analyte detection, GFETs are commonly integrated with bioreceptors such as aptamers, antibodies and so forth. In this work, aptamers are used as the representative target recognition probes. A major part of the implementation of such aptameric GFET devices is the reliable immobilization of aptamer probes onto the graphene channel of the device. In general, there are two main strategies for functionalizing aptamers on graphene, namely, the covalent and the non-covalent immobilization approaches. While the covalent approaches offer certain advantages over non-covalent methods in terms of stability and functionality, they unavoidably

altar the physical properties of graphene. Hence, non-covalent modifications have been frequently used in order to maintain the inherent properties of pristine graphene [203]. A typical non-covalent attachment of aptamers on graphene involves a two-step method as shown in Figure 8.1A. In the first step, a pyrene is anchored on the graphene via the π-π stacking interaction and in the second step, the amine-terminated aptamers are attached to the pyrene via the EDC/NHS (1-ethyl-3-(3-dimethylaminopropyl) carbodiimide hydrochloride/N-hydroxysuccinimide) crosslinking chemistry [204].

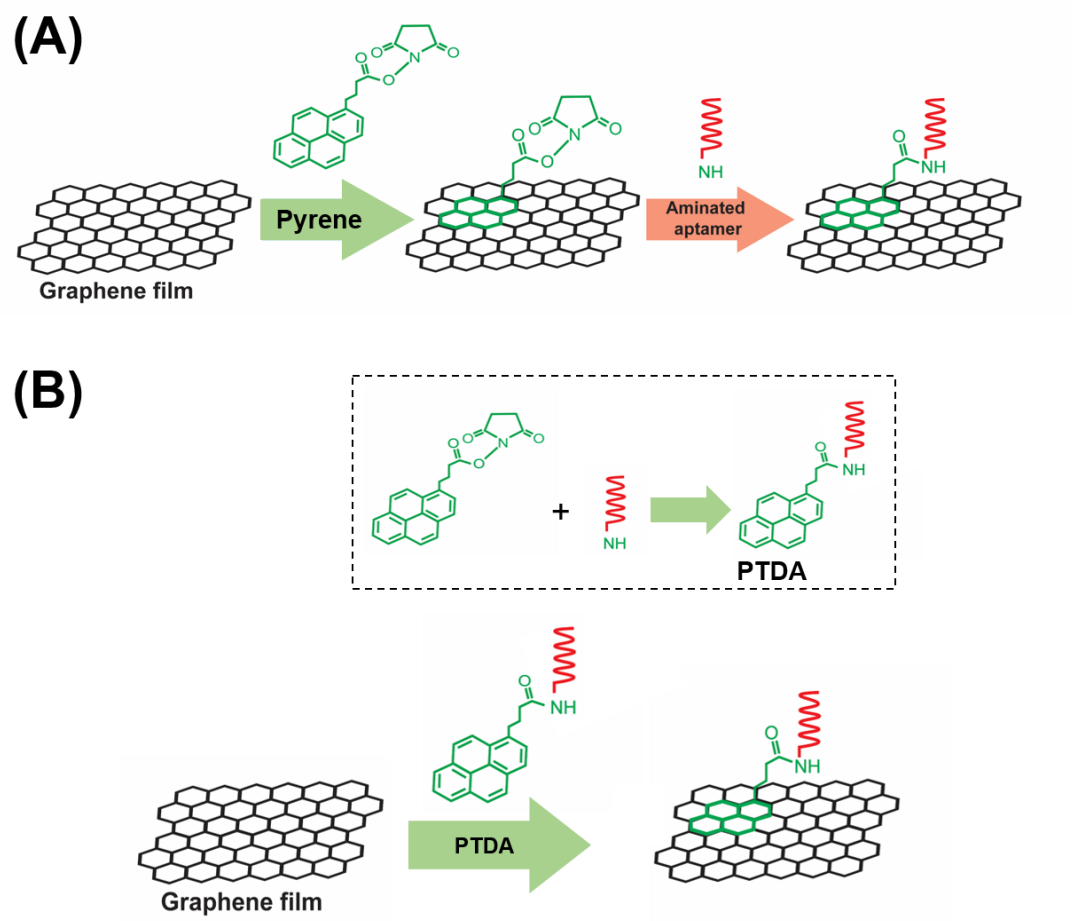

Figure 8.1. A schematic illustration of (A) a two-step aptamer functionalization on graphene requiring the use of organic solvents to dissolve and disperse PBASE (1-pyrenebutyric acid N-hydroxysuccinimide ester), and (B) the proposed one-step modification process of aptamer probes on GFET (Inset: the crosslinking of PBASE with an aminated aptamer to form a pyrene-tagged DNA aptamer (PTDA) probe.

A commonly used pyrene-based crosslinker, such as PBASE (1-pyrene butyric acid N-hydroxysuccinimide ester) as shown in Figure 8.1, requires organic solvents such as Dimethyl formamide (DMF) or Dimethyl sulfoxide (DMSO) in order for it to be well-dispersed in a solution. However, such solutions, being strong polar aprotic solvents, can dissolve most organic compounds [205] and can become an issue for a number of applications especially in lab-on-a-chip and point-of-care diagnostic platforms [206]–[208]. Such devices often utilize thermo plastics, flexible polymers, and passivation layers that are vulnerable to organic solvents resulting in fluid leakage and other irreversible damages. Therefore, to circumvent these challenges, an organic solvent-free aptamer immobilization method would be highly desirable and would also allow more flexibility in choosing the materials in device fabrication. In this chapter, I explore the feasibility of using an organic solvent-free aptamer functionalization technique where the amine-linked DNA aptamers are pre-tagged with pyrene groups. These pyrene-tagged DNA aptamers (PTDA) are easily soluble in an aqueous buffer and can be anchored onto graphene surfaces (Figure 1B) without the need of organic solvents. Wu et el. reported a GFET-based biosensor for selective detection of *E. Coli* with the aid of pyrene-tagged DNA aptamers [83]. In their work, the pyrene was incorporated during the synthesis process of the aptamers and the purification of the aptamers was also conducted using column chromatography. Another GFET-based biosensor was developed by Farid et al. for the detection of tuberculosis biomarker IFN-γ using pyrene tagged aptamers [209]. However, the aptamers were dissolved in DMF for diluting and immobilization on GFET surface. Inspired by the previous developments, I propose in this work a cheaper and simpler method to pyrene conjugation of the aptamers. Although pyrene conjugation on the terminal of oligonucleotides has been well-established [210], the main novelty of this work is in the use of such pyrene-tagged aptamers in the development of GFET-based protein biosensor. Here, I demonstrate that GFET-based biosensors developed using aptamers pre-conjugated with pyrenes are also effective in protein biomarker (IL-6) detection. In our approach, the PTDAs are formed by crosslinking the pyrene groups to the commercially available amine-terminated aptamers. Furthermore, to separate out the unreacted pyrenes, a simple purification is performed by precipitation with the help of a centrifuge. Following the synthesis, the pyrene-tagged aptamers are anchored onto the graphene surface. Moreover, the efficiency of the immobilization is enhanced by applying an external electric field (E-field) to the GFET through the gate electrode immersed in a PTDA solution (Figure 8.2). Generally, in the absence of an external electric field,

the amount of the PTDAs anchored on the graphene surface is limited by the rates of diffusion and mass transfer (Figure 8.2A (left)). However, by applying a negative electric field, the PTDA molecules, which are negatively charged due to the combined effects of the electron-rich pyrenyl groups and the negatively charged DNA strands, are pushed towards the graphene surface where they interact with the graphene through the formation of π-π stacking interaction thereby enhancing the immobilization rate and the surface coverage (Figure 8.2A (right)). This one-step functionalization method also eliminates the need for additional washing steps and thus reduces the time required for device fabrication. To demonstrate the effectiveness of our new technique in GFET-based biosensor implementation, the developed platform is used to detect interleukin-6 (IL-6) protein, a well-known cytokine and biomarker for immune responses, as a representative target analyte [188], [189].

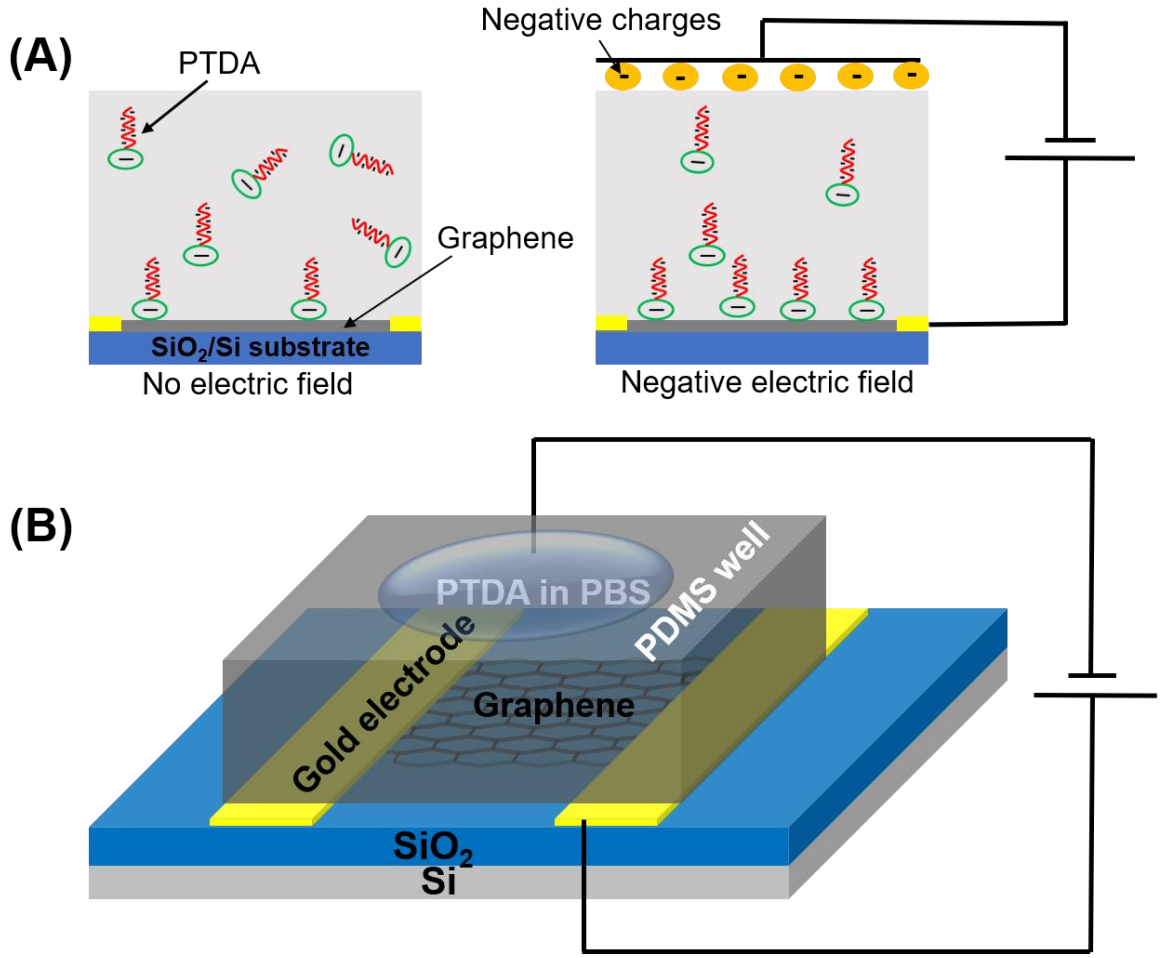

Figure 8.2. Schematic illustration showing the effect of applying an external electric field during the functionalization of PTDA. (A) The distribution of PTDAs in the incubation buffer without

and with the external electric field, and (B) device setup for applying the external E-field during the PTDA functionalization on GFET.

8.2. Materials and Methods

8.2.1. Materials

The aminated aptamers having the specific affinity to mouse IL-6 (#ATW0077, K_D=5.4 nM) and the resuspension buffer were purchased from Base Pair Biotechnologies, Inc. (TX, USA). The aptamer's affinity has been thoroughly characterized by the manufacturer and is shown to be specific toward IL-6 proteins. The predicted secondary structure of the aptamer sequence is presented in Figure 8.3A. PBASE (1-pyrene butyric acid N-hydroxysuccinimide ester) was purchased from Santa Cruz Biotechnology (TX, USA). The GFET chip (GFET-S20) fabricated on SiO_2/Si was purchased from Graphenea, Inc. (San Sebastian, Spain). The gold electrodes (source/drain) were passivated with insulating layers consisting of Al_2O_3 (50 nm)/Si_3N_4 (100 nm) surrounding the electrode/graphene interface. A polydimethylsiloxane (PDMS) well (3 mm diameter) was then integrated in-house to contain the liquid gate on the passivated area of the electrode as well as to reduce liquid evaporation during measurements and incubation steps. Figure 8.3B, C shows the image of the GFET chip consisting of 12 individual GFET devices with a PDMS well placed over the sensing area.

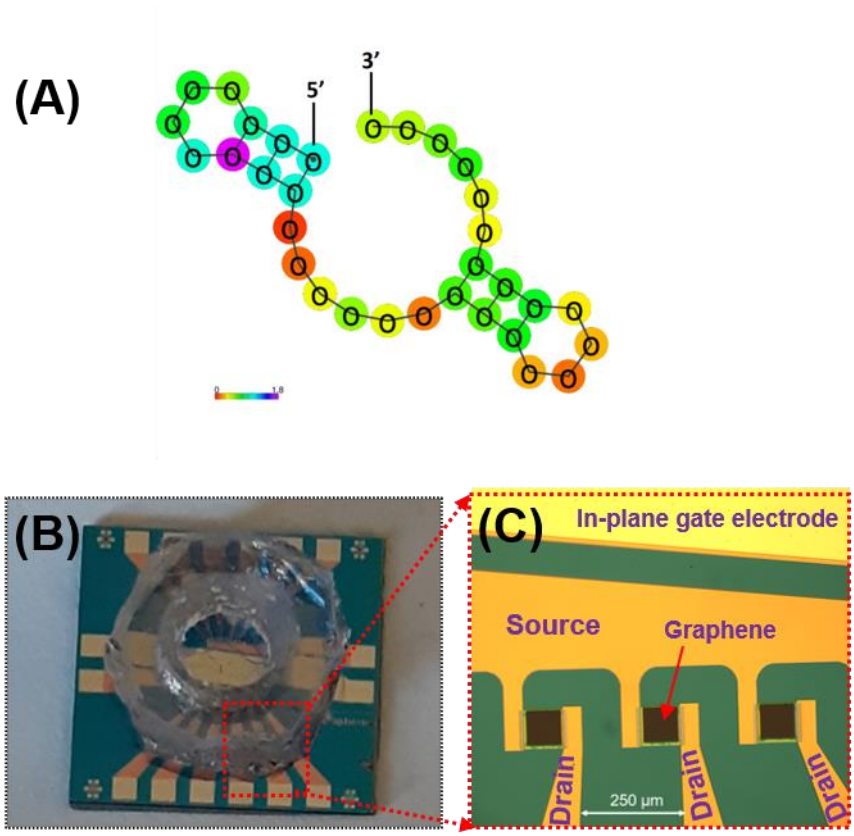

Figure 8.3. (A) Predicted secondary structure of the aptamer sequence purchased from Base Pair Biotechnologies, Inc. (Product # ATW0077) and the photographs of (B) the GFET chip (12 individual GFETs per chip) with PDMS well on top; and (B) the enlarged view of the 3 GFET devices of the chip (without the PDMS well). The source and drain electrodes are passivated with an insulating layer while the in-plane gate electrode is fully exposed.

8.2.2. Formation of pyrene-tagged DNA aptamer (PTDA) probes

The crosslinking of the pyrene groups to the aptamers to form PTDAs is achieved by incubating the aminated aptamers with PBASE dissolved in DMF following the protocol provided by the aptamer manufacturer [211]. Briefly, 50 µL of 100 µM IL-6 binding amine-linked (at the 5′ end) aptamer in amine resuspension buffer is mixed with 1.26 µL of 10 mg/mL PBASE for 1 hour in the dark. Then, 5 µL of 3 M sodium acetate is added to the aptamer/PBASE mixture followed by the addition of 125 µL cold ethanol (100%). The mixture is then placed in the freezer for 25 minutes followed by centrifugation at 13000 RPM for 15 minutes causing a pellet formation as a precipitate. The precipitate is collected by decanting the supernatant and then washed with 70% ethanol followed by resuspension in 0.01X phosphate buffer saline (PBS). As per the manufacturer

datasheet, the conjugation efficiency of the protocol varies from 50%–90%. Although the pellet is expected to contain a very high yield of conjugated PTDAs, it also includes some unconjugated aptamers or PBASE which can negatively impact the sensor performances. Also, there is the possibility of multi-conjugated aptamers due to the interaction with amine groups in the nucleobases. To obtain a precise yield of successful conjugation between aptamers and PBASE, a more time-consuming analytical tools such as high-performance liquid chromatography (HPLC) could be used to experimentally investigate the conjugation efficiency.

The concentration was determined by obtaining UV-Vis spectra measured with a Nanodrop spectrophotometer. Figure D1 (Appendix D) shows the UV-Visible spectrum of the resuspended PTDA. The peak at 260 nm corresponds to the presence of DNA nucleobases in the solution [212]. Although the UV-Vis spectrum is not able to provide the qualitative information about the aptamers (i.e., whether it is denatured or intact) we anticipated that the majority of the aptamers are in the properly functioning condition as evidenced by our GFET measurement results. Afterwards, the PTDA solution was stored at 4 °C.

8.2.3. Immobilization of PTDA on graphene

For GFET functionalization and measurements, a PDMS well was constructed over graphene to avoid evaporation of liquid. The solution containing PTDAs (2 µM in 0.01x PBS) was loaded into the well and a negative electric field (-400 mV) was applied to the solution using a wire inserted into the PTDA solution for 4 hours as shown in Figure 8.2B. Then, the GFET device was rinsed with DI water to remove any unbound PTDA probes.

8.2.4. Selective detection of IL-6 protein

After functionalizing the GFETs with IL-6 binding aptamers, various concentrations (0.1, 1, 10, and 100 nM) of IL-6 protein in 0.01x PBS with 2 mM $MgCl_2$ was exposed to the sensing area for 10 minutes. To investigate the selectivity and specificity, 100 nM of lysozyme (Lys) protein was also exposed to the IL-6 aptamer modified GFET in the same buffer.

8.2.5. Electrical measurements

For electrical measurements, the devices are placed on a probe station (Micromanipulator, 450

PM-B) and a Keysight B2902A source/measure unit (SMU) is used to measure the I_D–V_{GS} transfer characteristics. Voltage control and data acquisition are performed using a LabVIEW program. During the measurement, the drain–source voltage (V_{DS}) is biased at 100 mV and the drain current (I_D) was read while the liquid–gate voltage (V_{GS}) was linearly scanned from 0 V to 1 V with a voltage step of 12.5 mV using the in-plane gold gate electrode. A scan rate of 12.5 mV/s was maintained so that I_D is stabilized to ensure reliable measurements of the I_D–V_{GS} transfer curves.

8.3. Results and Discussion

8.3.1. Characterization of device performance and effect of gate materials

8.3.1.1. Mobility calculation of the GFET devices

The transfer characteristics of a transistor in a linear region can be described as follows [213]:

$$\boldsymbol{I_{DS} = \frac{W}{L}.C_{TG}.\mu.(V_{GS} - V_{CNP}).V_{DS}}$$

Where, $\frac{W}{L}$ is the width-to-length ratio of the GFET channel, $\boldsymbol{C_{TG}}$ is the total gate capacitance of the liquid gate, $\boldsymbol{\mu}$ is the carrier mobility. Figure 8.4A shows the ambipolar transfer characteristics of a GFET resulting in a V-shaped curve where the left branch represents the increasing density of positive charge carriers (holes) and the right branch represents the increasing density of negative charge carriers (electrons) [214]. The critical transition voltage between the two regions where the current reaches a minimum is called the charge neutrality point (V_{CNP}) or the Dirac voltage (V_D) [215]. The slope of the transfer curve ($\frac{dI_{DS}}{dV_{GS}}$) in each region indicates the transconductance ($\boldsymbol{g_m}$) for the hole and the electron, respectively and can be calculated by measuring the slopes of each branch of Figure 8.4A. Mathematically, $\boldsymbol{g_m}$ can be expressed as [216]:

$$\boldsymbol{g_m = \frac{dI_{DS}}{dV_{GS}} = \frac{W}{L}.C_{TG}.\mu.V_{DS}}$$

Which leads to the following expression for mobility:

$$\boldsymbol{\mu = \frac{L}{W}.\frac{g_m}{C_{TG}.V_{DS}}}$$

Therefore, the average carrier mobilities for holes and electrons were calculated to be: $\boldsymbol{\mu_h = 1920 \pm 61}$ cm^2/V/s and $\boldsymbol{\mu_e = 2475 \pm 163}$ cm^2/V/s, where $\boldsymbol{V_{DS} = 100}$ mV and the value of $\boldsymbol{C_{TG}}$

was taken to be 1.65 μF/cm^2 [217]. This high values of the carrier mobilities indicate the suitability of the GFETs for sensing applications.

Another important parameter that affects the sensitivity of the GFET devices is the on-off ratio (I_{ON}/I_{OFF}) of the drain-source current. The larger the value of the on-off ratio, the better the sensitivity of the GFGET since the device will exhibit better immunity to noises. An on-off ratio value of ~8 is calculated for the used devices which is above average for GFET devices grown by a CVD technique [215].

7.3.1.2. Effect of gate materials on device characteristics

I also investigate the effect of different gate materials (Pt, Au, and Ag/AgCl) on the GFET transfer characteristics illustrated in Figure 8.4B, C, D. Figure 8.4B shows the effects of the three gates on the Dirac voltage or the charge neutrality point (V_{CNP}) for the 6 GFET devices on a single chip. As seen in the figure, Ag/AgCl gate electrode gives the lowest V_{CNP} among the three gate electrodes. However, the gold electrode provides the lowest device-to-device variations among the devices on a single chip.

Figure 8.4C shows the effect of gate materials on gate leakage current where each bar represents the RMS value of the leakage current (I_{GS}) calculated from the I_{GS}-V_{GS} curves (See Appendix D). The RMS value is calculated using the following equation:

$$\boldsymbol{I_{GS}} = \sqrt{\frac{\mathbf{1}}{\boldsymbol{n}}\sum_{\boldsymbol{i}} \boldsymbol{i_{GS}^2}}$$

Where, $\boldsymbol{n}$ is the number of measurement points, and $\boldsymbol{i_{GS}}$ is the leakage current for each individual gate voltage.

Gate leakage has been a very common phenomenon in liquid-gate GFETs and is primarily caused by the electrochemical redox reaction at the graphene/liquid interface resulting in an increased current flow that negatively impacts the sensing performances of a sensor. Though passivation of exposed electrodes can reduce the leakage current, carbon clusters and photoresist residues during the wet transfer of CVD-graphene act as a source of carbon leading to redox current during IV

scans [218], [219]. Among the three gate materials tested, Ag/AgCl results in the lowest gate leakage.

Figure 8.4D shows the effect of gate materials on the hysteresis of GFET transfer characteristics. Gate hysteresis or simply, hysteresis in GFET is the deviation of drain-source current upon reversal of the gate voltage sweep direction [220]–[222]. This causes a shift in the charge neutrality points in the forward and backward scans (See Appendix B). This shift ($\Delta V_{CNP,h}$) has been plotted in Figure 8.4D for the three gate materials. It can be seen that Ag/AgCl gives the lowest hysteresis.

Though Ag/AgCl demonstrates the best performance in terms of operating voltage, gate leakage and gate hysteresis, in-plane gold electrode is used throughout the experiments as it gives the highest uniformity of the charge neutrality point among the devices on a single chip. Moreover, the in-plane configuration of the gold electrode which can be fabricated at the same lithography step as the golden source and drain electrodes enhance the compactness of the setup and allows potential integration with the microfluidics platform [204].

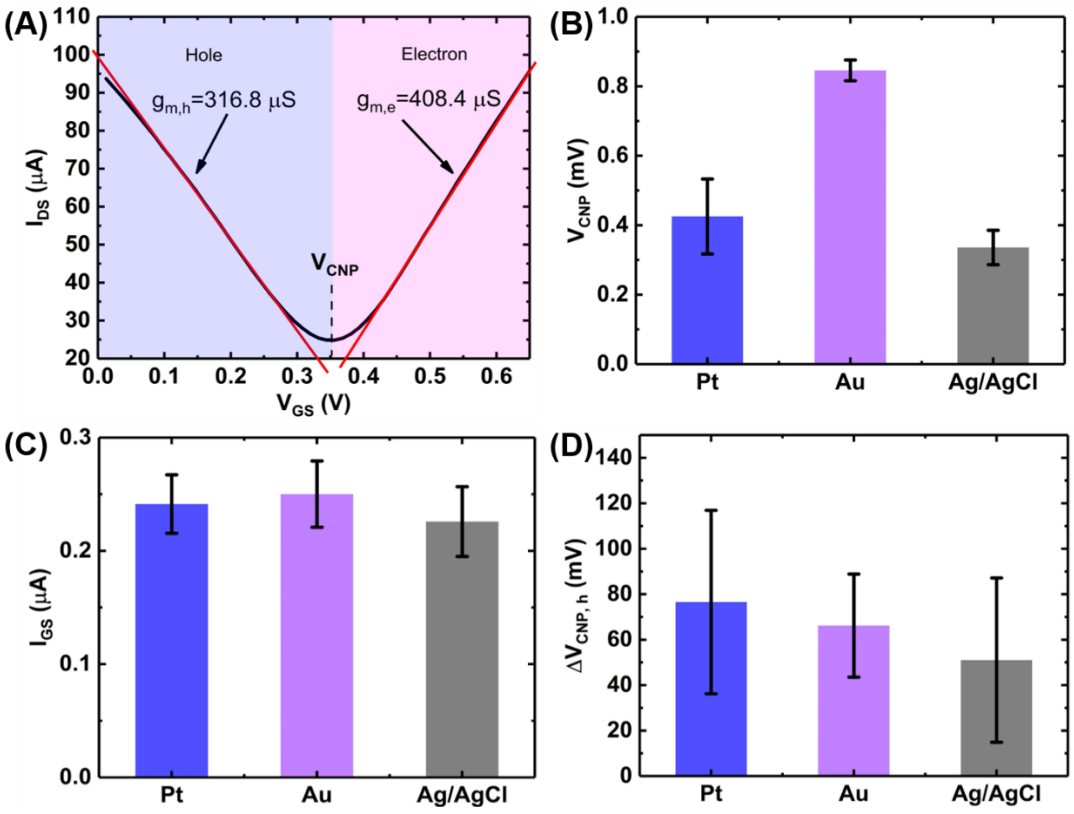

Figure 8.4. Characterization of GFET device performances and effect of gate materials. (A) GFET transfer curve showing the calculation of transconductance, and bar charts showing the effect of gate materials on (B) V_{CNP}, (C) leakage current (rms value), and (D) gate hysteresis.

8.3.1.3. Characterization of successful functionalization of GFETs

The synthesized PTDAs were first characterized to verify the presence of an amide bond between the PBASE and the aminated aptamer. The amide bond was characterized using the Fourier-transform infrared (FTIR) spectroscopy as presented in Figure 8.5A, where the presence of a strong peak at 1653 cm^{-1} (C=O stretching in the amide I) and the broad stretching vibration peak around 3300–3550 cm^{-1} (N–H from the amide, –OH group at the 3′ end of the DNA) confirm the amide bond formation [204]. Although amine groups from adenine, cytosine, guanine can also react with the NHS ester of the PBASE linker resulting in amide bond, this efficiency of these reactions are quite low compared with that with the primary amine group connected at the 5′ end of the DNA aptamer. Hence, it is expected that the amide peak at the FTIR is primarily attributed to the amide bond at the 5′ end of the aptamer.

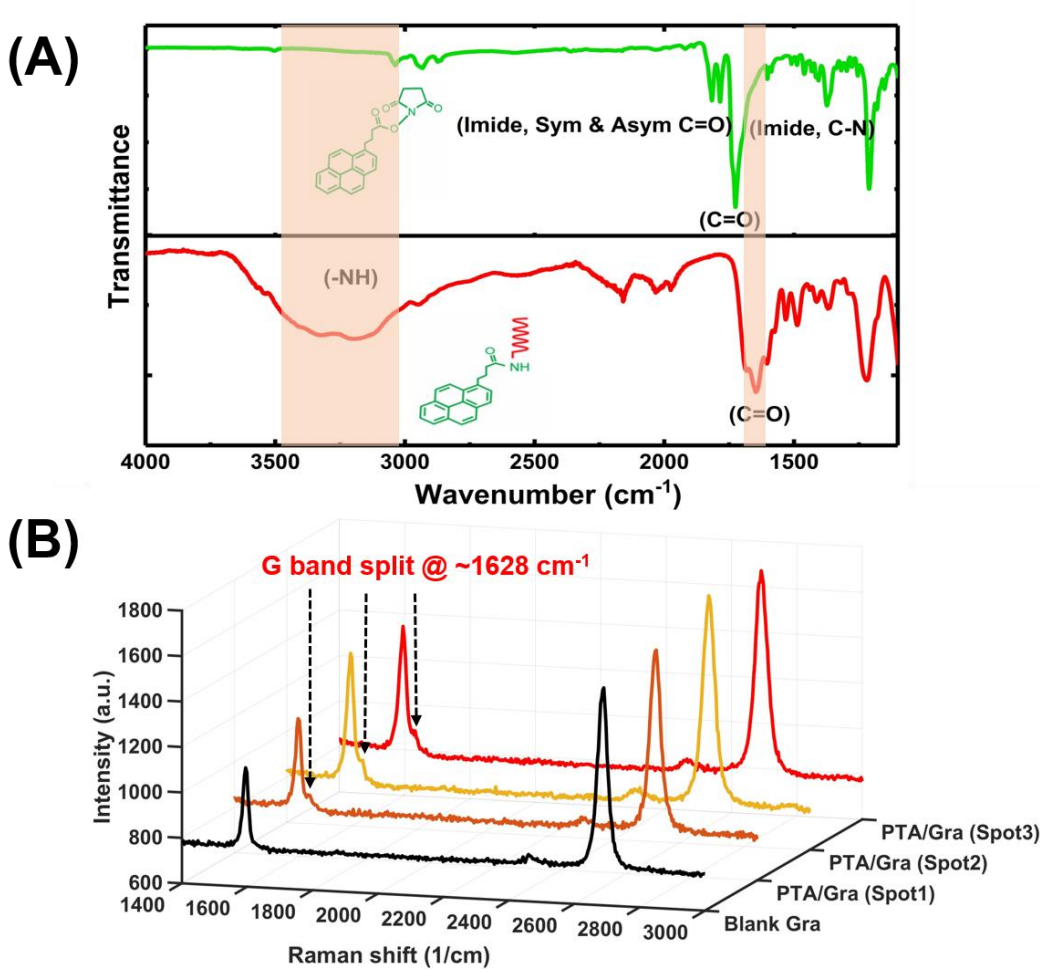

Figure 8.5. Optical characterization of the one-step functionalization of aptamer probes on graphene. (A) FTIR characterization of the amide bond of PTDA in dry state, and (B) Raman spectrum (excitation by 532 nm) of three spots of PTDA functionalized graphene along with that of a blank graphene (Gra).

After the amide bond was confirmed by the FTIR spectroscopy, the PTDAs were immobilized on a bare graphene. The presence of the PTDAs on graphene was confirmed by Raman spectroscopy. For Raman measurements, two samples were prepared, a blank graphene and a graphene functionalized with PTDAs. The Raman spectra for the PTDA-modified graphene was taken at 3 different spots on the surface. Figure 8.5B shows the Raman spectra of the blank and the PTDA-functionalized graphene where the G-band split at around 1628 cm^{-1} indicates the anchoring of the PTDAs by π-π stacking interaction between the pyrene ring of the PTDA and the basal plane of graphene [204].

The anchoring of the PTDAs on graphene surface is also verified electrically by measuring the GFET transfer curves before and after the probe attachment. As shown in Figure 8.6A, the charge neutrality point shifts left upon PTDA immobilization on graphene. This negative shift is in accordance with the negative charges on the DNA backbone and the electron-rich pyrene group of the PTDA and is also consistent with the previous work by Wu et al [217]. Furthermore, the effects of an external electric field can also be characterized using the I_{DS}-V_{GS} curves. Figure 8.6A further shows that when a negative potential is applied at the gate, the PTDA immobilization efficiency is enhanced which is reflected by the increased amount of the negative shift in the charge neutrality point (V_{CNP}) compared to the case without the external electric field. With a negative potential at the gate, the negatively charged single-stranded PTDAs tend to migrate towards graphene surface due to the electrostatic repulsion resulting in an increased density of the immobilized PTDA probes [223]. Figure 8.6B shows the bar graph indicating the amount of shift in the V_{CNP} with respect to the blank GFET device for the two cases. With the electric field applied, the negative shift in the charge neutrality point was measured to be 123.53 mV which is approximately 2.5 times larger than that without the electric field.

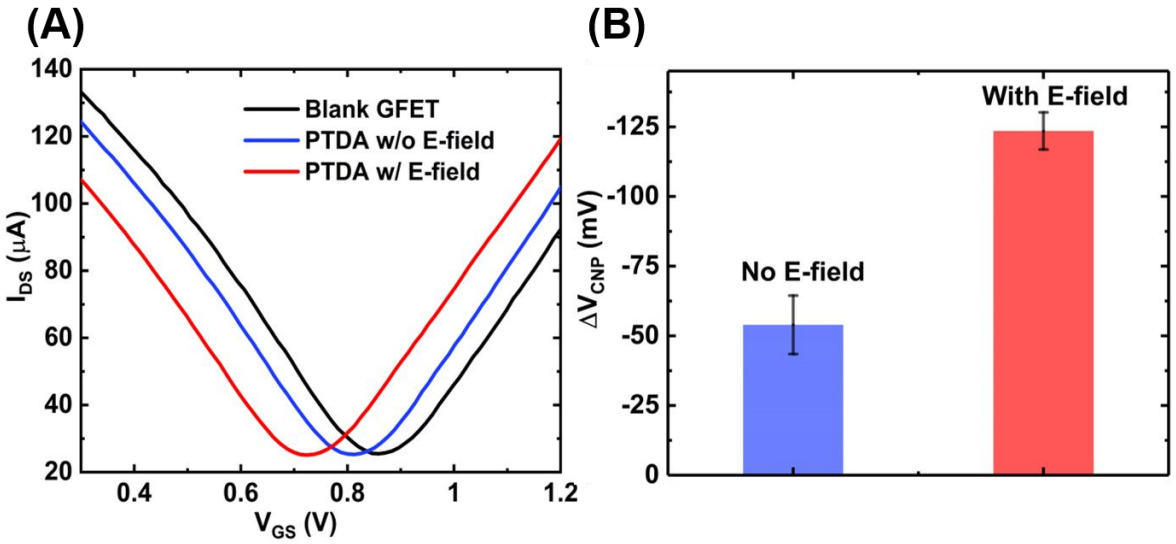

Figure 8.6. GFET transfer curves showing the effect of external electric field on functionalization of PTDA on GFET devices. (A) GFET transfer curves, and (B) the corresponding shift in V_{CNP} (n=5).

8.3.1.4. Sensitivity and selectivity study of the sensor

After the successful functionalization of the GFET with the PTDAs, the device was exposed to IL-6 proteins to characterize its sensing performances. Prior to IL-6 exposure, in order to test the sensor's selectivity to its target, the GFET-based IL-6 sensor was exposed to 100 nM of lysozyme protein (a model interfering species) in 0.01X PBS with 2 mM $MgCl_2$ for 10 minutes. Once the selectivity of the IL-6 binding aptamers was confirmed, the sensor was then exposed to various concentrations (100 pM, 1 nM, 10 nM, and 100 nM) of the target protein (IL-6) in the same buffer and for the same exposure time. Figure 8.7A, B show the transfer curves and the bar graph, respectively, for each sample exposure. These results indicate that our sensor platform is minimally responsive to a non-target protein (lysozyme) even when a relatively large concentration (100 nM) is exposed. By contrast, upon introducing 100 pM of the target biomarker IL-6 to the GFET sensing area, the charge neutrality point shifts to the negative direction by a significant amount indicating the specific analyte recognition by the aptamers as well as the target selectivity of the developed IL-6 biosensor. The charge neutrality point continues to shift to the left with increasing concentrations of IL-6 (Figure 8.7C). This consistent negative shift can be attributed to the n-type doping of the graphene channel by the bound IL-6 proteins which have an isoelectric point of 4 ~ 5.3 and therefore, is negatively charged under the buffer (pH=7.4) used in the experiment [224], [225]. The basis of this target-induced doping of graphene is the target-induced conformational change of the aptamers. In the absence of the target analytes, the aptamers anchored on the graphene surface are in an unfolded, loop and flexible state. Upon exposure of the IL-6 targets, target-induced conformational change of aptamers leads to a compact and stable state. These structural changes of aptamers brings the negatively charged IL-6 protein to the close proximity of the graphene surface, possibly resulting in a direct transfer (doping) of electrons from IL-6 to graphene due to the π-π stacking interactions between the aromatic amino acids in IL-6 and the basal plane of graphene [224].

Also, the specificity of sensor was examined by functionalizing the GFET with a random sequence aptamer using the same protocol as the IL-6 aptamer and exposing different concentrations of IL-6 protein. The results are presented in Figure D3 (Appendix D) which shows negligible shift in the charge neutrality point after exposure to IL-6 protein. This further verifies that the IL-6 binding

aptamer used in our sensor development exhibits specific target binding toward the IL-6 biomarker.

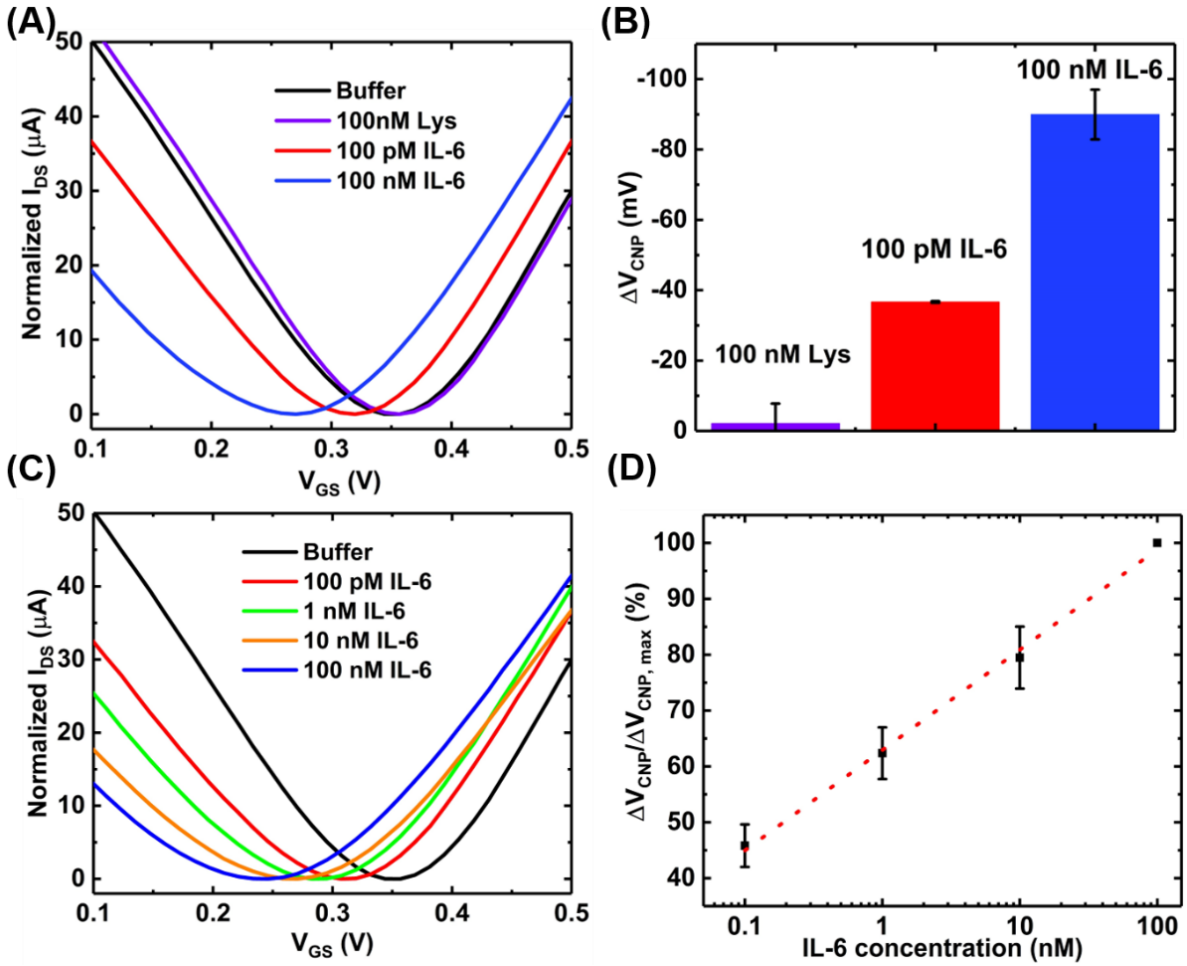

Figure 8.7. Sensing experiments with the GFET-based aptasensor: (A) the transfer curves, (B) the bar chart showing the selectivity of the sensor (error bar with n=3); (C) transfer curves of the GFET sensor when exposed to varying concentrations of IL-6; and (D) the concentration-dependent calibration curve (n=3).

Figure 8.7D shows the calibration curve for a range of IL-6 concentrations obtained with a sample size of n = 3. The device-to-device variations were addressed by normalizing the sensor response (ΔVCNP) using the formula ΔVCNP/ΔVCNP,max, where VCNP,max is the charge neutrality point corresponding to the maximum IL-6 concentration tested. The lowest concentration of 100 pM was detected with this method. However, increasing the number of washings steps (with 70% ethanol) in the purification stage of the synthesis process and optimizing the incubation time may

lead to increased sensitivity. Moreover, adjusting the buffer pH to make IL-6 positively charged will increase the affinity between the positively charged IL-6 and negatively charged aptamer, possibly leading to enhanced sensitivity. As an example, Figure 8.8 shows the IL-6 sensing result and the corresponding calibration curve of the GFET-based biosensor in the same buffer (0.01x PBS + 2 mM $MgCl_2$) but with the pH adjusted to ~3.64.

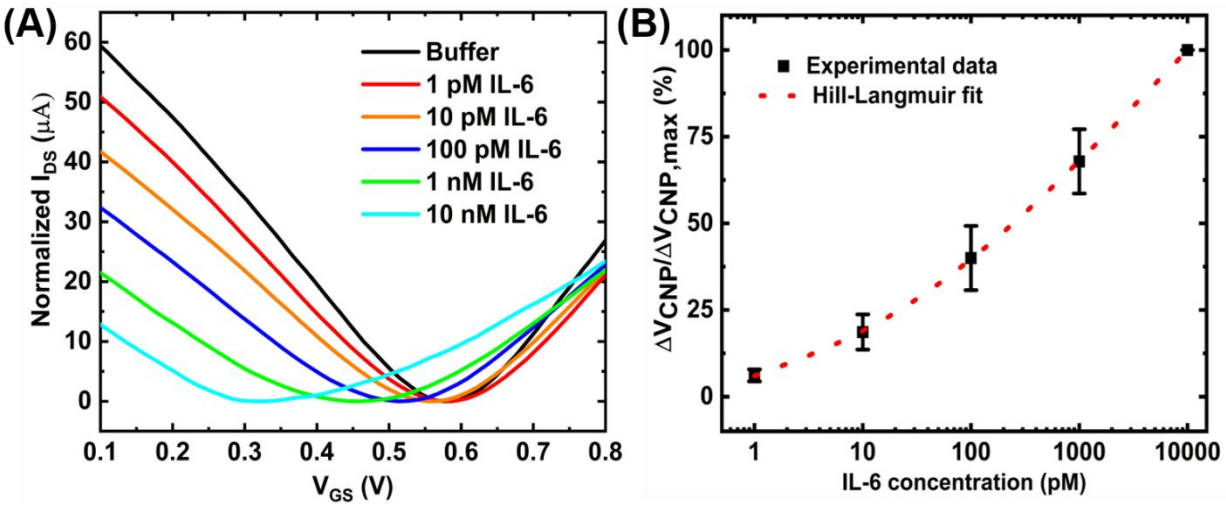

Figure 8.8. Detection of IL-6 with the GFET-based biosensor under the pH of ~3.64: (A) I_{DS}-V_{GS} transfer curves for different concentrations of IL-6 protein and (B) the corresponding concentration-dependent calibration curve. The sample set is n = 3 and error bar represents 1 standard error.

The limit of detection (LOD) of the GFET-based IL-6 sensor under this pH environment was calculated to be ~8 pM which is an order of magnitude larger than that under the physiological pH (pH ~7.4). Figure 8.8B also shows the Hill-Langmuir fit (See Appendix C) of the experimental data. The sensing performances of the proposed sensor are comparable to other results published in the literature. For example, Hao et al. have achieved a detection limit of 1.22 pM and a detection range of 1 pM–1 nM using conventional aptamer immobilization methods [223]. From the Hill-Langmuir equation, the dissociation constant K_D is estimated to be 3.4 nM, similar to the value (5.4 nM) reported by the manufacturer for the aptamer-target pair.

8.4. Testing in Artificial Sweat

To verify the applicability of the sensors in real samples, the sensors must be tested in real samples. As an initial step, the sensor was tested in diluted artificial perspiration (pH=7.4) purchased from Pickering Solutions. As the perspiration is highly viscous, it was first diluted 10 times using 0.01x PBS in 1mM $MgCl_2$ and this diluted perspiration was spiked with different concentrations of IL-6 protein which was exposed to the GFET sensor. The results are presented in Figure 8.9. With the Dirac voltage shifted consistently with increased concentration of IL-6 spiked in artificial perspiration, it is clear that the sensor is able to detect IL-6 in artificial sweat referring to its potential applicability in real human sweat.

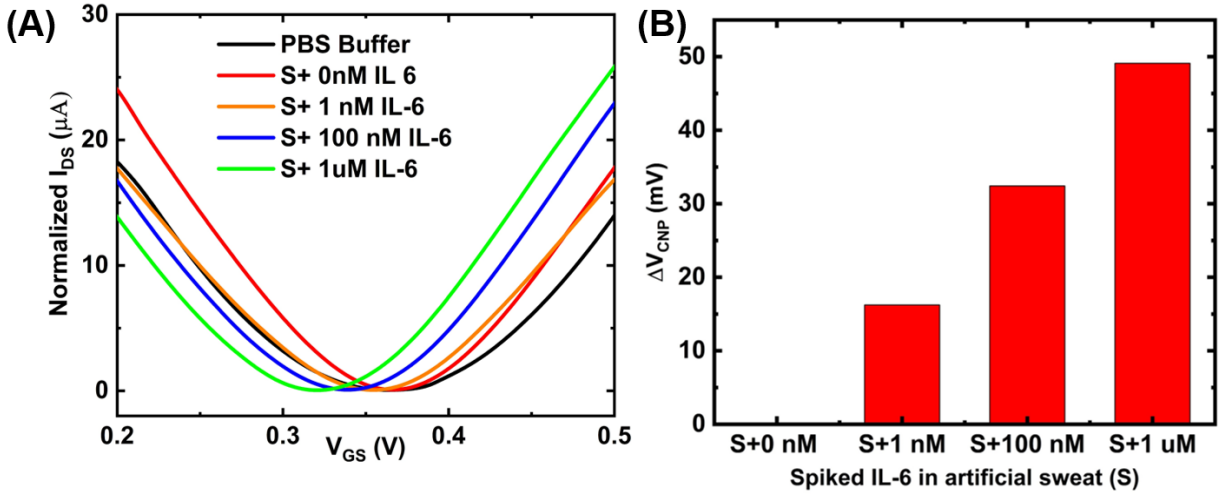

Figure 8.9. Detection of IL-6 in artificial perspiration. (A) GFET measurements showing relative shift for different concentrations of IL-6 spiked in diluted artificial perspiration, and (B) corresponding bar chart showing the shift of the Dirac voltage.

8.5. Conclusion

In this chapter, I develop a facile and rapid immobilization technique to attach target recognition probes on the GFET-based biosensing platform. The developed sensor is able to selectively measure IL-6 protein biomarker with the detection limit in the picomolar range. The sensitivity can be further improved by increasing the incubation time, purification steps as well as by adjusting the buffer pH to an acidic region. The proposed organic solvent-free aptamer immobilization technique is not only polymer friendly (and therefore allows more flexibility in device design and fabrication) but also simplifies and shortens the graphene modification process by eliminating the

extra step needed for anchoring the linker molecules and the subsequent washing steps. I also demonstrate that an external electric field can be used to enhance the efficiency (~2.5 times) of the aptamer immobilization on the graphene surface. My proposed technology has the potential to be used in monitoring IL-6 from real physiologically relevant fluid samples such as sweat, serum and cerebrospinal fluid.

CHAPTER 9: CONCLUSION AND FUTURE WORK

8.1. Summary of Contributions

The main contributions of this dissertation in the field of nanoelectronic device-based biosensors are briefly described as follows:

A. The use of inkjet-printing in manufacturing low-cost electrochemical biosensors was presented (Chapter 4). Inkjet-printable ink based on CNT and aptamer mixture was prepared and printed on disposable screen-printed carbon electrode using drop-on-demand inkjet printer. We have shown that printing of CNT-based ink can be used as a means for immobilizing aptamers on the electrode contrary to the commonly used chemistries which are often time consuming, lacks control on packing density, as well require laboratory settings with trained personnel. The inkjet-printed biosensor not only addresses the issues in the conventional aptamer immobilization methods, but also demonstrates comparable performances with the conventional electrochemical biosensors in terms of sensitivity, selectivity, and shelf-life.

B. A protein biomarker Lysozyme was detected using a CVD grown graphene FET for the first time (Chapter 5). The liquid-gated GFET device was able to selectively detect lysozyme with nanomolar limit of detection.

C. An integrated GFET platform was developed to detect another protein biomarker Thrombin with picomolar limit of detection (Chapter 6). This was done by integrating the GFET device with microfluidic channel which eliminates the measurement inaccuracy introduced by evaporation and thus improves the sensitivity. Moreover, the compactness of the platform was enhanced by replacing the conventionally suspended gate electrode with an in-plane photolithographically-patterned gate electrode. Also, real-time continuous detection of Thrombin was demonstrated and verified with discreate measurements.

D. A flexible GFET platform was developed using a PCB printed electrode on flexible polyimide (Kapton®) substrate. Graphene transfer protocol for the rigid SiO_2/Si substrate was tailored considering the thermal and chemical stability of the flexible substrate. Real-time detection of a sweat-based protein interleukin-6 (IL-6) was also demonstrated using this flexible printed GFET device (Chapter 7).

E. The limitations of the conventionally manufactured electrode design were addressed by adopting a printing-based electrode fabrication method (Chapter 7). Conventionally, electrodes are manufactured using microfabrication techniques which require costly microfabrication setup, sophisticated cleanroom environment as well as trained personnel limiting the affordability of the sensors in point-of-care applications. However, the proposed device electrodes printed with a benchtop PCB printer not only addresses the above-mentioned issues but is also compatible with applications requiring flexible substrates. This enables the development of a wearable biosensor for real-time continuous monitoring of individual's health.

F. A facile and rapid aptamer-immobilization method was developed for functionalizing GFET devices without the need of any organic solvents such as dimethyl formamide (DMF) or Dimethyl siloxane (DMSO). These organic solvents often used in the conventional aptamer immobilization method on GFET are generally not compatible with the polymer-based substrates as well as the fluidic tubings and channels for flexible and lab-on-a-chip based sensing devices. Therefore, this organic solvent-free immobilization method can address these challenges by eliminating the use of such organic solvents (Chapter 8).

G. The effects of various gate materials (Pt, Au, Ag/AgCl) on the GFET measurements were investigated. It is found that among the three gates, Ag/AgCl demonstrates the best performance in terms of operating voltage, gate leakage and gate hysteresis, while in-plane gold electrode results in the most stable charge neutrality point (Chapter 8).

8.2. Future Work

The sensors developed in this work has great potentials for health care monitoring, especially for point-of-care diagnostics and personalized medicine. However, before field deployment of these devices can become a reality, certain challenges still remain to be addressed. The following are the future research directions needed in order to render these sensing platforms field deployable.

8.2.1. Real-sample analysis

Though novel contributions have been made towards developing nanoelectronic device-based biosensing platforms, real physiological samples have not been used to evaluate the sensors.

Though the sensors passed the selectivity test performed by adding a limited number of interferants into the buffer, real-sample analysis is of paramount importance to make sure that the developed sensors function properly with human samples such as serum, saliva, etc. as real human samples contain thousands of interferants that could reduce the signal-to-noise ratio (SNR). The sensors should be equipped with interferant-rejecting mechanisms such as coating materials or blocking agents [226] that could prevent non-specific adsorption (NSA) leading to an increase in the sensor's inertness to non-target interferants. For example, Wang et al. employed a polymer coating, namely polyethylene glycol (PEG), to functionalize GFET surface for preventing NSA for aptamer-based detection of IgE protein in human serum [91]. However, the PEG modified GFETs experienced significant reduction in the transconductance [227], thus negatively affecting the sensitivity. Therefore, novel NSA reduction methods without affecting sensing performances should be developed.

8.2.2. Flexible printed GFET

Though printed Kapton® GFET has been shown to be effective for real-time sensing of IL-6 biomarkers. Possible modifications for improving the performance of the printed GFET are discussed in this section.

Choosing the right flexible substrate could be one future direction of research for improving the performance of the flexible GFET. Though Kapton® stands out as one of the best flexible substrate in terms of their chemical and thermal stability to tolerate the heating steps in the manufacturing processes, there are a few drawbacks associated with this material. One of them is the poor adhesion of the printed electrodes that causes the electrodes to peel off from the substrate. Though high temperature sintering can address the issue to some extent, it might affect the substrate's thermal stability. Therefore, other polymer materials should be investigated to solve this issue. For example, Liang et al. used polyethylene naphthalate (PEN) substrate (Teonex® Q65 film) for developing a flexible GFET [228]. In another example, Mylar was used for developing a flexible and stretchable GFET for detection of TNF-α [194]. The decreased carrier mobility due to the unwanted doping induced in graphene by the flexible substrates should also be considered. This could be solved using an additional coating of dielectric like SiO_2 over the flexible substrate [229].

Another area for improvement in the printed GFET of this work is the lack of stretchability due to the cracking of the printed electrodes. Therefore, development of a highly conductive and stretchable ink is needed.

References

[1] A. P. F. Turner, “Biosensors: sense and sensibility,” *Chem. Soc. Rev.*, vol. 42, no. 8, pp. 3184–3196, Feb. 2013.

[2] G. Luka *et al.*, “Microfluidics Integrated Biosensors: A Leading Technology towards Lab-on-a-Chip and Sensing Applications,” *Sensors*, vol. 15, no. 12, pp. 30011–30031, Dec. 2015.

[3] M. A. Morales and J. Mark Halpern, “Guide to Selecting a Biorecognition Element for Biosensors,” *Bioconjug. Chem.*, vol. 29, no. 10, pp. 3231–3239, Oct. 2018.

[4] L. C. J. Qlark, “Monitor and control of blood and tissue oxygen tensions,” *ASAIO J.*, vol. 2, no. 1, p. 41, Apr. 1956.

[5] L. C. Clark and C. Lyons, “Electrode systems for continuous monitoring in cardiovascular surgery,” *Ann. N. Y. Acad. Sci.*, vol. 102, pp. 29–45, Oct. 1962.

[6] G. G. Guilbault and J. G. Montalvo, “Urea-specific enzyme electrode,” *J. Am. Chem. Soc.*, vol. 91, no. 8, pp. 2164–2165, Apr. 1969.

[7] C.-M. Tîlmaciu and M. C. Morris, “Carbon nanotube biosensors,” *Front. Chem.*, vol. 3, Oct. 2015.

[8] N. Bhalla, P. Jolly, N. Formisano, and P. Estrela, “Introduction to biosensors,” *Essays Biochem.*, vol. 60, no. 1, pp. 1–8, Jun. 2016.

[9] S. Song, L. Wang, J. Li, C. Fan, and J. Zhao, “Aptamer-based biosensors,” *TrAC Trends Anal. Chem.*, vol. 27, no. 2, pp. 108–117, Feb. 2008.

[10] S. Dehghani *et al.*, “Aptamer-based biosensors and nanosensors for the detection of vascular endothelial growth factor (VEGF): A review,” *Biosens. Bioelectron.*, vol. 110, pp. 23–37, Jul. 2018.

[11] Biomarkers Definitions Working Group., “Biomarkers and surrogate endpoints: preferred definitions and conceptual framework,” *Clin. Pharmacol. Ther.*, vol. 69, no. 3, pp. 89–95, Mar. 2001.

[12] H. Mischak *et al.*, “Recommendations for biomarker identification and qualification in clinical proteomics,” *Sci. Transl. Med.*, vol. 2, no. 46, p. 46ps42, Aug. 2010.

[13] A. Ravalli, D. Voccia, I. Palchetti, and G. Marrazza, “Electrochemical, Electrochemiluminescence, and Photoelectrochemical Aptamer-Based Nanostructured Sensors for Biomarker Analysis,” *Biosensors*, vol. 6, no. 3, p. 39, Sep. 2016.

[14] N. Rifai, M. A. Gillette, and S. A. Carr, “Protein biomarker discovery and validation: the long and uncertain path to clinical utility,” *Nat. Biotechnol.*, vol. 24, no. 8, pp. 971–983, Aug. 2006.

[15] B. Strehlitz, N. Nikolaus, and R. Stoltenburg, “Protein Detection with Aptamer Biosensors,” *Sensors*, vol. 8, no. 7, pp. 4296–4307, Jul. 2008.

[16] X. Weng and S. Neethirajan, “A microfluidic biosensor using graphene oxide and aptamer-functionalized quantum dots for peanut allergen detection,” *Biosens. Bioelectron.*, vol. 85, pp. 649–656, Nov. 2016.

[17] L. Farzin, M. Shamsipur, L. Samandari, and S. Sheibani, “Recent advances in designing nanomaterial based biointerfaces for electrochemical biosensing cardiovascular biomarkers,” *J. Pharm. Biomed. Anal.*, vol. 161, pp. 344–376, Nov. 2018.

[18] Y. Xiao, A. A. Lubin, A. J. Heeger, and K. W. Plaxco, “Label-Free Electronic Detection of Thrombin in Blood Serum by Using an Aptamer-Based Sensor,” *Angew. Chem. Int. Ed.*, vol. 44, no. 34, pp. 5456–5459, Aug. 2005.

[19] A. Gencoglu and A. R. Minerick, “Electrochemical detection techniques in micro- and nanofluidic devices,” *Microfluid. Nanofluidics*, vol. 17, no. 5, pp. 781–807, Nov. 2014.

[20] J. L. Hammond, N. Formisano, P. Estrela, S. Carrara, and J. Tkac, “Electrochemical biosensors and nanobiosensors,” *Essays Biochem.*, vol. 60, no. 1, pp. 69–80, Jun. 2016.

[21] A. Chen and B. Shah, “Electrochemical sensing and biosensing based on square wave voltammetry,” *Anal. Methods*, vol. 5, no. 9, pp. 2158–2173, Apr. 2013.

[22] S. Chen and M. H. Shamsi, “Biosensors-on-chip: a topical review,” *J. Micromechanics Microengineering*, vol. 27, no. 8, p. 083001, Jul. 2017.

[23] N. I. Khan, A. G. Maddaus, and E. Song, “A Low-Cost Inkjet-Printed Aptamer-Based Electrochemical Biosensor for the Selective Detection of Lysozyme,” *Biosensors*, vol. 8, no. 1, p. 7, Mar. 2018.

[24] J. G. Guan, Y. Q. Miao, and Q. J. Zhang, “Impedimetric biosensors,” *J. Biosci. Bioeng.*, vol. 97, no. 4, pp. 219–226, Jan. 2004.

[25] S. Brosel-Oliu, N. Uria, N. Abramova, and A. Bratov, “Impedimetric Sensors for Bacteria Detection,” *Biosens. - Micro Nanoscale Appl.*, Sep. 2015.

[26] Z. Chen, L. Li, H. Zhao, L. Guo, and X. Mu, “Electrochemical impedance spectroscopy detection of lysozyme based on electrodeposited gold nanoparticles,” *Talanta*, vol. 83, no. 5, pp. 1501–1506, Feb. 2011.

[27] S. Ghosh, N. I. Khan, J. G. Tsavalas, and E. Song, “Selective Detection of Lysozyme Biomarker Utilizing Large Area Chemical Vapor Deposition-Grown Graphene-Based Field-Effect Transistor,” *Front. Bioeng. Biotechnol.*, vol. 6, Mar. 2018.

[28] G. Lu, L. E. Ocola, and J. Chen, “Reduced graphene oxide for room-temperature gas sensors,” *Nanotechnology*, vol. 20, no. 44, p. 445502, Oct. 2009.

[29] Y. W. Huang *et al.*, “Real-Time and Label-Free Detection of the Prostate-Specific Antigen in Human Serum by a Polycrystalline Silicon Nanowire Field-Effect Transistor Biosensor,” *Anal. Chem.*, vol. 85, no. 16, pp. 7912–7918, Aug. 2013.

[30] G. Zhou, J. Chang, S. Cui, H. Pu, Z. Wen, and J. Chen, “Real-Time, Selective Detection of Pb2+ in Water Using a Reduced Graphene Oxide/Gold Nanoparticle Field-Effect Transistor Device,” *ACS Appl. Mater. Interfaces*, vol. 6, no. 21, pp. 19235–19241, Nov. 2014.

[31] S. Mao and J. Chen, “Graphene-based electronic biosensors,” *J. Mater. Res.*, vol. 32, no. 15, pp. 2954–2965, Aug. 2017.

[32] Y. Ohno, K. Maehashi, and K. Matsumoto, “Label-Free Biosensors Based on Aptamer-Modified Graphene Field-Effect Transistors,” *J. Am. Chem. Soc.*, vol. 132, no. 51, pp. 18012–18013, Dec. 2010.

[33] Z. Fu, Y. C. Lu, and J. J. Lai, “Recent Advances in Biosensors for Nucleic Acid and Exosome Detection,” *Chonnam Med. J.*, vol. 55, no. 2, pp. 86–98, May 2019.

[34] V. C. Ozalp, G. Bayramoglu, Z. Erdem, and M. Y. Arica, “Pathogen detection in complex samples by quartz crystal microbalance sensor coupled to aptamer functionalized core-shell type magnetic separation,” *Anal. Chim. Acta*, vol. 853, pp. 533–540, Jan. 2015.

[35] S. Neethirajan, V. Ragavan, X. Weng, and R. Chand, “Biosensors for Sustainable Food Engineering: Challenges and Perspectives,” *Biosensors*, vol. 8, no. 1, Mar. 2018.

[36] A. Afzal, A. Mujahid, R. Schirhagl, S. Z. Bajwa, U. Latif, and S. Feroz, “Gravimetric Viral Diagnostics: QCM Based Biosensors for Early Detection of Viruses,” *Chemosensors*, vol. 5, no. 1, p. 7, Mar. 2017.

[37] O. Aydin and O. Uçar, “Design for Smaller, Lighter and Faster ICT Products: Technical Expertise, Infrastructures and Processes,” Adv. Sci. Technol. Eng. Syst. J. vol. 2, no. 3, pp. 1114-1128 , Jun. 2017

[38] S. C. B. Gopinath, T. Lakshmipriya, M. K. Md Arshad, M. N. A. Uda, and Y. Al-Douri, “9 - Nanoelectronics in Biosensing Applications,” in *Nanobiosensors for Biomolecular Targeting*, S. C. B. Gopinath and T. Lakshmipriya, Eds. Elsevier, pp. 211–224, Sep. 2019.

[39] “Nanotechnology,” Available: https://chembam.com/definitions/nanotechnology/ (accessed Dec. 05, 2019).

[40] W. Yang, K. R. Ratinac, S. P. Ringer, P. Thordarson, J. J. Gooding, and F. Braet, “Carbon Nanomaterials in Biosensors: Should You Use Nanotubes or Graphene?,” *Angew. Chem. Int. Ed.*, vol. 49, no. 12, pp. 2114–2138, Mar. 2010.

[41] D. Iglesias, S. Bosi, M. Melchionna, T. Da Ros, and S. Marchesan, “The Glitter of Carbon Nanostructures in Hybrid/Composite Hydrogels for Medicinal Use,” *Curr. Top. Med. Chem.*, vol. 16, no. 18, pp. 1976–1989, Feb. 2016.

[42] “Carbon Nanoelectronics | Electronics Science and Technology Division.” Available: https://www.nrl.navy.mil/estd/branches/6810/factsheets/carbon-nanoelectronics (accessed Oct. 08, 2019).

[43] C. D. Cress, “Carbon Nanoelectronics,” *Electronics*, vol. 3, no. 1, pp. 22–25, Mar. 2014.

[44] “Multi-Walled Carbon Nanotubes: Production, Analysis, and Application,” *AZoNano.com*, May 23, 2013. Available: https://www.azonano.com/article.aspx?ArticleID=3469 (accessed Oct. 09, 2019).

[45] “Chirality of single-walled carbon nanotubes | Research | Kato Group at RIKEN.” Available: http://katogroup.riken.jp/en/nanotubechirality.html (accessed Oct. 09, 2019).

[46] M. Endo, T. Hayashi, and Y.A. Kim, “Large-scale production of carbon nanotubes and their applications,” *Pure Appl. Chem.*, vol. 78, no. 9, pp. 1703–1713, Jan. 2006.

[47] T. Kurkina, “Label-free electrical biosensing based on electrochemically functionalized carbon nanostructures,” PhD Dissertation, Institute of Inorganic and Analytical Chemistry, University of Giessen (accessed Oct. 09, 2019).

[48] J. J. Gooding, “Nanostructuring electrodes with carbon nanotubes: A review on electrochemistry and applications for sensing,” *Electrochimica Acta*, vol. 50, no. 15, pp. 3049–3060, May 2005.

[49] A. Chou, T. Böcking, N. K. Singh, and J. J. Gooding, “Demonstration of the importance of oxygenated species at the ends of carbon nanotubes for their favourable electrochemical properties,” *Chem. Commun.*, no. 7, pp. 842–844, Feb. 2005.

[50] C. E. Banks, X. Ji, A. Crossley, and R. G. Compton, “Understanding the Electrochemical Reactivity of Bamboo Multiwalled Carbon Nanotubes: the Presence of Oxygenated Species at Tube Ends May not Increase Electron Transfer Kinetics,” *Electroanalysis*, vol. 18, no. 21, pp. 2137–2140, Nov. 2006.

[51] M. Pumera, “Electrochemical properties of double wall carbon nanotube electrodes,” *Nanoscale Res. Lett.*, vol. 2, no. 2, p. 87, Jan. 2007.

[52] M. Pumera, T. Sasaki, and H. Iwai, “Relationship between Carbon Nanotube Structure and Electrochemical Behavior: Heterogeneous Electron Transfer at Electrochemically Activated Carbon Nanotubes,” *Chem. – Asian J.*, vol. 3, no. 12, pp. 2046–2055, Dec. 2008.

[53] P. Kara, A. de la Escosura-Muñiz, M. Maltez-da Costa, M. Guix, M. Ozsoz, and A. Merkoçi, “Aptamers based electrochemical biosensor for protein detection using carbon nanotubes platforms,” *Biosens. Bioelectron.*, vol. 26, no. 4, pp. 1715–1718, Dec. 2010.

[54] F. Rohrbach, H. Karadeniz, A. Erdem, M. Famulok, and G. Mayer, “Label-free impedimetric aptasensor for lysozyme detection based on carbon nanotube-modified screen-printed electrodes,” *Anal. Biochem.*, vol. 421, no. 2, pp. 454–459, Feb. 2012.

[55] S. Mallakpour and S. Soltanian, “Surface functionalization of carbon nanotubes: fabrication and applications,” *RSC Adv.*, vol. 6, no. 111, pp. 109916–109935, Nov. 2016.

[56] R. P. Tortorich and J. W. Choi, “Inkjet Printing of Carbon Nanotubes,” *Nanomaterials*, vol. 3, no. 3, pp. 453–468, Jul. 2013.

[57] M. Zheng *et al.*, “DNA-assisted dispersion and separation of carbon nanotubes,” *Nat. Mater.*, vol. 2, no. 5, pp. 338–342, May 2003.

[58] K. Guo *et al.*, “An aptamer–SWNT biosensor for sensitive detection of protein via mediated signal transduction,” *Electrochem. Commun.*, vol. 13, no. 7, pp. 707–710, Jul. 2011.

[59] Y. Lian, F. He, X. Mi, F. Tong, and X. Shi, “Lysozyme aptamer biosensor based on electron transfer from SWCNTs to SPQC-IDE,” *Sens. Actuators B Chem.*, vol. 199, pp. 377–383, Aug. 2014.

[60] M. H. Andrew Ng, L. T. Hartadi, H. Tan, and C. H. Patrick Poa, “Efficient coating of transparent and conductive carbon nanotube thin films on plastic substrates,” *Nanotechnology*, vol. 19, no. 20, p. 205703, May 2008.

[61] E. Artukovic, M. Kaempgen, D. S. Hecht, S. Roth, and G. Grüner, “Transparent and Flexible Carbon Nanotube Transistors,” *Nano Lett.*, vol. 5, no. 4, pp. 757–760, Apr. 2005.

[62] V. Scardaci, R. Coull, J. N. Coleman, L. Byrne, and G. Scott, “Carbon Nanotube network based sensors,” in *2012 12th IEEE International Conference on Nanotechnology (IEEE-NANO)*, pp. 1–3, Aug. 2012.

[63] H. Z. Geng, K. K. Kim, K. P. So, Y. S. Lee, Y. Chang, and Y. H. Lee, “Effect of Acid Treatment on Carbon Nanotube-Based Flexible Transparent Conducting Films,” *J. Am. Chem. Soc.*, vol. 129, no. 25, pp. 7758–7759, Jun. 2007.

[64] A. Sarkar and T. Daniels-Race, “Electrophoretic Deposition of Carbon Nanotubes on 3-Amino-Propyl-Triethoxysilane (APTES) Surface Functionalized Silicon Substrates,” *Nanomater. Basel Switz.*, vol. 3, no. 2, pp. 272–288, May 2013.

[65] J. Li *et al.*, “Field emission characteristic of screen-printed carbon nanotube cathode,” *Appl. Surf. Sci.*, vol. 220, no. 1, pp. 96–104, Dec. 2003.

[66] C. S. Jones, X. Lu, M. Renn, M. Stroder, and W. S. Shih, “Aerosol-jet-printed, high-speed, flexible thin-film transistor made using single-walled carbon nanotube solution,” *Microelectron. Eng.*, vol. 87, no. 3, pp. 434–437, Mar. 2010.

[67] J. Vaillancourt *et al.*, “All ink-jet-printed carbon nanotube thin-film transistor on a polyimide substrate with an ultrahigh operating frequency of over 5 GHz,” *Appl. Phys. Lett.*, vol. 93, no. 24, p. 243301, Dec. 2008.

[68] Y. Zhou, L. Hu, and G. Grüner, “A method of printing carbon nanotube thin films,” *Appl. Phys. Lett.*, vol. 88, no. 12, p. 123109, Mar. 2006.

[69] P. Bollella *et al.*, “Beyond graphene: Electrochemical sensors and biosensors for biomarkers detection,” *Biosens. Bioelectron.*, vol. 89, pp. 152–166, Mar. 2017.

[70] N. Chauhan, T. Maekawa, and D. N. S. Kumar, “Graphene based biosensors—Accelerating medical diagnostics to new-dimensions,” *J. Mater. Res.*, vol. 32, no. 15, pp. 2860–2882, Aug. 2017.

[71] K. S. Novoselov *et al.*, “Two-dimensional atomic crystals,” *Proc. Natl. Acad. Sci.*, vol. 102, no. 30, pp. 10451–10453, Jul. 2005.

[72] Y. Song, Y. Luo, C. Zhu, H. Li, D. Du, and Y. Lin, “Recent advances in electrochemical biosensors based on graphene two-dimensional nanomaterials,” *Biosens. Bioelectron.*, vol. 76, pp. 195–212, Feb. 2016.

[73] H. Gao and H. Duan, “2D and 3D graphene materials: Preparation and bioelectrochemical applications,” *Biosens. Bioelectron.*, vol. 65, pp. 404–419, Mar. 2015.

[74] Y. Zhu *et al.*, “Graphene and Graphene Oxide: Synthesis, Properties, and Applications,” *Adv. Mater.*, vol. 22, no. 35, pp. 3906–3924, Jun. 2010.

[75] A. Peigney, Ch. Laurent, E. Flahaut, R. R. Bacsa, and A. Rousset, “Specific surface area of carbon nanotubes and bundles of carbon nanotubes,” *Carbon*, vol. 39, no. 4, pp. 507–514, Apr. 2001.

[76] P. Avouris, “Graphene: Electronic and Photonic Properties and Devices,” *Nano Lett.*, vol. 10, no. 11, pp. 4285–4294, Nov. 2010.

[77] C.H. Lu, H.H. Yang, C.L. Zhu, X. Chen, and G.N. Chen, “A graphene platform for sensing biomolecules,” *Angew. Chem. Int. Ed Engl.*, vol. 48, no. 26, pp. 4785–4787, Jun. 2009.

[78] H. Chang, L. Tang, Y. Wang, J. Jiang, and J. Li, “Graphene Fluorescence Resonance Energy Transfer Aptasensor for the Thrombin Detection,” *Anal. Chem.*, vol. 82, no. 6, pp. 2341–2346, Mar. 2010.

[79] Z. Hao *et al.*, “Real-Time Monitoring of Insulin Using a Graphene Field-Effect Transistor Aptameric Nanosensor,” *ACS Appl. Mater. Interfaces*, vol. 9, no. 33, pp. 27504–27511, Aug. 2017.

[80] Y. Ohno, K. Maehashi, Y. Yamashiro, and K. Matsumoto, “Electrolyte-Gated Graphene Field-Effect Transistors for Detecting pH and Protein Adsorption,” *Nano Lett.*, vol. 9, no. 9, pp. 3318–3322, Sep. 2009.

[81] Y. Ohno, K. Maehashi, and K. Matsumoto, “Chemical and biological sensing applications based on graphene field-effect transistors,” *Biosens. Bioelectron.*, vol. 26, no. 4, pp. 1727–1730, Dec. 2010.

[82] X. Chen *et al.*, "Ultratrace antibiotic sensing using aptamer/graphene-based field-effect transistors," *Biosens. Bioelectron.*, vol. 126, pp. 664–671, Feb. 2019.

[83] G. Wu *et al.*, "Graphene Field-Effect Transistors for the Sensitive and Selective Detection of Escherichia coli Using Pyrene-Tagged DNA Aptamer," *Adv. Healthc. Mater.*, vol. 6, no. 19, Oct. 2017.

[84] D. Reddy, L. F. Register, G. D. Carpenter, and S. K. Banerjee, "Graphene field-effect transistors," *J. Phys. Appl. Phys.*, vol. 44, no. 31, p. 313001, Jul. 2011.

[85] C. Andronescu and W. Schuhmann, "Graphene-based field effect transistors as biosensors," *Curr. Opin. Electrochem.*, vol. 3, no. 1, pp. 11–17, Jun. 2017.

[86] R. X. He *et al.*, "Solution-Gated Graphene Field Effect Transistors Integrated in Microfluidic Systems and Used for Flow Velocity Detection," *Nano Lett.*, vol. 12, no. 3, pp. 1404–1409, Mar. 2012.

[87] T. Y. Chen *et al.*, "Label-free detection of DNA hybridization using transistors based on CVD grown graphene," *Biosens. Bioelectron.*, vol. 41, pp. 103–109, Mar. 2013.

[88] S. Xu *et al.*, "Real-time reliable determination of binding kinetics of DNA hybridization using a multi-channel graphene biosensor," *Nat. Commun.*, vol. 8, p. 14902, Mar. 2017.

[89] S. Mao *et al.*, "Two-dimensional nanomaterial-based field-effect transistors for chemical and biological sensing," *Chem. Soc. Rev.*, vol. 46, no. 22, pp. 6872–6904, Nov. 2017.

[90] J. Lin *et al.*, "Gating of single-layer graphene with single-stranded deoxyribonucleic acids," *Small Weinh. Bergstr. Ger.*, vol. 6, no. 10, pp. 1150–1155, May 2010.

[91] X. Wang *et al.*, "A graphene aptasensor for biomarker detection in human serum," *Electrochimica Acta*, vol. 290, pp. 356–363, Nov. 2018.

[92] Z. Zheng, H. Zhang, T. Zhai, and F. Xia, "Overcome Debye Length Limitations for Biomolecule Sensing based on Field Effective Transistors," *Chin. J. Chem.*, vol. 39, issue. 4, pp. 999–1008, Apr. 2021.

[93] N. Kumar *et al.*, "Detection of a multi-disease biomarker in saliva with graphene field effect transistors," *Med. Devices Sens.*, vol. 3, no. 6, p. e10121, Sep. 2020.

[94] A. Vasilescu, Q. Wang, M. Li, R. Boukherroub, and S. Szunerits, "Aptamer-Based Electrochemical Sensing of Lysozyme," *Chemosensors*, vol. 4, no. 2, Art. no. 2, Jun. 2016.

[95] J. S. Prakash and K. Rajamanickam, "Aptamers and Their Significant Role in Cancer Therapy and Diagnosis," *Biomedicines*, vol. 3, no. 3, pp. 248–269, Sep. 2015.

[96] A. K. H. Cheng, B. Ge, and H.Z. Yu, “Aptamer-Based Biosensors for Label-Free Voltammetric Detection of Lysozyme,” *Anal. Chem.*, vol. 79, no. 14, pp. 5158–5164, Jul. 2007.

[97] L. D. Li, Z. B. Chen, H. T. Zhao, L. Guo, and X. Mu, “An aptamer-based biosensor for the detection of lysozyme with gold nanoparticles amplification,” *Sens. Actuators B Chem.*, vol. 149, no. 1, pp. 110–115, Aug. 2010.

[98] C. Serra *et al.*, “Expression and prognostic significance of lysozyme in male breast cancer,” *Breast Cancer Res.*, vol. 4, no. 6, p. R16, Aug. 2002.

[99] L. Sandin *et al.*, “Beneficial effects of increased lysozyme levels in Alzheimer’s disease modelled in Drosophila melanogaster,” *Febs J.*, vol. 283, no. 19, pp. 3508–3522, Oct. 2016.

[100] I. Torsteinsdóttir, L. Hâkansson, R. Hällgren, B. Gudbjörnsson, N. G. Arvidson, and P. Venge, “Serum lysozyme: a potential marker of monocyte/macrophage activity in rheumatoid arthritis,” *Rheumatol. Oxf. Engl.*, vol. 38, no. 12, pp. 1249–1254, Dec. 1999.

[101] M. Prato, M. Polimeni, and V. Tullio, “Human Lysozyme in Malaria Patients: Possible Role as Biomarker for Disease Severity,” in *Human and Mosquito Lysozymes: Old Molecules for New Approaches Against Malaria*, M. Prato, Ed. Cham: Springer International Publishing, 2015, pp. 83–90.

[102] M. H. Grieco, M. M. Reddy, H. B. Kothari, M. Lange, E. Buimovici-Klein, and D. William, “Elevated beta 2-microglobulin and lysozyme levels in patients with acquired immune deficiency syndrome,” *Clin. Immunol. Immunopathol.*, vol. 32, no. 2, pp. 174–184, Aug. 1984.

[103] K. A. Near and M. J. Lefford, “Use of serum antibody and lysozyme levels for diagnosis of leprosy and tuberculosis,” *J. Clin. Microbiol.*, vol. 30, no. 5, pp. 1105–1110, May 1992.

[104] R. S. Pascual, J. B. Gee, and S. C. Finch, “Usefulness of serum lysozyme measurement in diagnosis and evaluation of sarcoidosis,” *N. Engl. J. Med.*, vol. 289, no. 20, pp. 1074–1076, Nov. 1973.

[105] K. R. Falchuk, J. L. Perrotto, and K. J. Isselbacher, “Serum lysozyme in Crohn’s disease. A useful index of disease activity,” *Gastroenterology*, vol. 69, no. 4, pp. 893–896, Oct. 1975.

[106] G. Liang, Y. Man, X. Jin, L. Pan, and X. Liu, “Aptamer-based biosensor for label-free detection of ethanolamine by electrochemical impedance spectroscopy,” *Anal. Chim. Acta*, vol. 936, pp. 222–228, Sep. 2016.

[107] L. D. Li, H. T. Zhao, Z. B. Chen, X. J. Mu, and L. Guo, “Aptamer biosensor for label-free impedance spectroscopy detection of thrombin based on gold nanoparticles,” *Sens. Actuators B Chem.*, vol. 157, no. 1, pp. 189–194, Sep. 2011.

[108] M. C. Rodriguez, A. N. Kawde, and J. Wang, “Aptamer biosensor for label-free impedance spectroscopy detection of proteins based on recognition-induced switching of the surface charge,” *Chem. Commun. Camb. Engl.*, no. 34, pp. 4267–4269, Sep. 2005.

[109] M. Du, T. Yang, C. Zhao, and K. Jiao, “Electrochemical logic aptasensor based on graphene,” *Sens. Actuators B Chem.*, vol. 169, pp. 255–260, Jul. 2012.

[110] E. Song, T. H. da Costa, and J.-W. Choi, “A chemiresistive glucose sensor fabricated by inkjet printing,” *Microsyst. Technol.*, vol. 23, no. 8, pp. 3505–3511, Aug. 2017.

[111] A. Maddaus *et al.*, “Design and fabrication of bio-hybrid materials using inkjet printing,” *Biointerphases*, vol. 11, no. 4, p. 041002, Nov. 2016.

[112] T. H. da Costa, E. Song, R. P. Tortorich, and J.-W. Choi, “A Paper-Based Electrochemical Sensor Using Inkjet-Printed Carbon Nanotube Electrodes,” *ECS J. Solid State Sci. Technol.*, vol. 4, no. 10, p. S3044, Aug. 2015.

[113] J. C. Cox and A. D. Ellington, “Automated selection of anti-Protein aptamers,” *Bioorg. Med. Chem.*, vol. 9, no. 10, pp. 2525–2531, Oct. 2001.

[114] R. J. White, N. Phares, A. A. Lubin, Y. Xiao, and K. W. Plaxco, “Optimization of electrochemical aptamer-based sensors via optimization of probe packing density and surface chemistry,” *Langmuir ACS J. Surf. Colloids*, vol. 24, no. 18, pp. 10513–10518, Sep. 2008.

[115] J. T. Wen, C.M. Ho, and P. B. Lillehoj, “Coffee Ring Aptasensor for Rapid Protein Detection,” *Langmuir*, vol. 29, no. 26, pp. 8440–8446, Jul. 2013.

[116] A. B. Steel, T. M. Herne, and M. J. Tarlov, “Electrochemical Quantitation of DNA Immobilized on Gold,” *Anal. Chem.*, vol. 70, no. 22, pp. 4670–4677, Nov. 1998.

[117] S. Balamurugan, A. Obubuafo, R. L. McCarley, S. A. Soper, and D. A. Spivak, “Effect of Linker Structure on Surface Density of Aptamer Monolayers and Their Corresponding Protein Binding Efficiency,” *Anal. Chem.*, vol. 80, no. 24, pp. 9630–9634, Dec. 2008.

[118] H. Wu, Y. Zuo, C. Cui, W. Yang, H. Ma, and X. Wang, “Rapid Quantitative Detection of Brucella melitensis by a Label-Free Impedance Immunosensor Based on a Gold

Nanoparticle-Modified Screen-Printed Carbon Electrode," *Sensors*, vol. 13, no. 7, pp. 8551–8563, Jul. 2013.

[119] M. R. Shoar Abouzari, F. Berkemeier, G. Schmitz, and D. Wilmer, "On the physical interpretation of constant phase elements," *Solid State Ion.*, vol. 180, no. 14, pp. 922–927, Jun. 2009.

[120] E. Katz and I. Willner, "Probing Biomolecular Interactions at Conductive and Semiconductive Surfaces by Impedance Spectroscopy: Routes to Impedimetric Immunosensors, DNA-Sensors, and Enzyme Biosensors," *Electroanalysis*, vol. 15, no. 11, pp. 913–947, Jul. 2003.

[121] R. Kirby *et al.*, "Aptamer-Based Sensor Arrays for the Detection and Quantitation of Proteins," *Anal. Chem.*, vol. 76, no. 14, pp. 4066–4075, Jul. 2004.

[122] M. Wang *et al.*, "An electrochemical aptasensor based on a TiO2/three-dimensional reduced graphene oxide/PPy nanocomposite for the sensitive detection of lysozyme," *Dalton Trans.*, vol. 44, no. 14, pp. 6473–6479, Mar. 2015.

[123] D. Xie *et al.*, "Click chemistry-assisted self-assembly of DNA aptamer on gold nanoparticles-modified screen-printed carbon electrodes for label-free electrochemical aptasensor," *Sens. Actuators B Chem.*, vol. 192, pp. 558–564, Mar. 2014.

[124] C. Ocaña, A. Hayat, R. K. Mishra, A. Vasilescu, M. del Valle, and J.L. Marty, "Label free aptasensor for Lysozyme detection: A comparison of the analytical performance of two aptamers," *Bioelectrochemistry*, vol. 105, pp. 72–77, Oct. 2015.

[125] H. Huang, Q. Zhang, J. Luo, and Y. Zhao, "Sensitive colorimetric detection of lysozyme in human serum using peptide-capped gold nanoparticles," *Anal. Methods*, vol. 4, no. 11, pp. 3874–3878, Oct. 2012.

[126] P. Subramanian *et al.*, "Lysozyme detection on aptamer functionalized graphene-coated SPR interfaces," *Biosens. Bioelectron.*, vol. 50, pp. 239–243, Dec. 2013.

[127] M. C. Rodríguez and G. A. Rivas, "Label-free electrochemical aptasensor for the detection of lysozyme," *Talanta*, vol. 78, no. 1, pp. 212–216, Apr. 2009.

[128] Z. Chen and J. Guo, "A reagentless signal-off architecture for electrochemical aptasensor for the detection of lysozyme," *Electrochimica Acta*, vol. 111, pp. 916–920, Nov. 2013.

[129] D. Niwa, K. Omichi, N. Motohashi, T. Homma, and T. Osaka, “Organosilane self-assembled monolayer-modified field effect transistors for on-chip ion and biomolecule sensing,” *Sens. Actuators B Chem.*, vol. 108, no. 1, pp. 721–726, Jul. 2005.

[130] J. Wang, K. Ito, T. Nakanishi, S. Kuroiwa, and T. Osaka, “Tb3+-enhanced Potentiometric Detection of Single Nucleotide Polymorphism by Field Effect Transistors,” *Chem. Lett.*, vol. 38, no. 4, pp. 376–377, Mar. 2009.

[131] S. Hideshima, R. Sato, S. Kuroiwa, and T. Osaka, “Fabrication of stable antibody-modified field effect transistors using electrical activation of Schiff base cross-linkages for tumor marker detection,” *Biosens. Bioelectron.*, vol. 26, no. 5, pp. 2419–2425, Jan. 2011.

[132] S. Xu *et al.*, “Direct growth of graphene on quartz substrates for label-free detection of adenosine triphosphate,” *Nanotechnology*, vol. 25, no. 16, p. 165702, Mar. 2014.

[133] Y. Huang, X. Dong, Y. Liu, L. J. Li, and P. Chen, “Graphene-based biosensors for detection of bacteria and their metabolic activities,” *J. Mater. Chem.*, vol. 21, no. 33, pp. 12358–12362, Aug. 2011.

[134] Y. Chen *et al.*, “Field-Effect Transistor Biosensor for Rapid Detection of Ebola Antigen,” *Sci. Rep.*, vol. 7, Sep. 2017.

[135] Y. Ohno, K. Maehashi, K. Inoue, and K. Matsumoto, “Label-Free Aptamer-Based Immunoglobulin Sensors Using Graphene Field-Effect Transistors,” *Jpn. J. Appl. Phys.*, vol. 50, no. 7R, p. 070120, Jul. 2011.

[136] J. Xia, F. Chen, J. Li, and N. Tao, “Measurement of the quantum capacitance of graphene,” *Nat. Nanotechnol.*, vol. 4, no. 8, Art. no. 8, Aug. 2009.

[137] M. B. Lerner *et al.*, “Scalable Production of Highly Sensitive Nanosensors Based on Graphene Functionalized with a Designed G Protein-Coupled Receptor,” *Nano Lett.*, vol. 14, no. 5, pp. 2709–2714, May 2014.

[138] R. J. Chen, Y. Zhang, D. Wang, and H. Dai, “Noncovalent Sidewall Functionalization of Single-Walled Carbon Nanotubes for Protein Immobilization,” *J. Am. Chem. Soc.*, vol. 123, no. 16, pp. 3838–3839, Apr. 2001.

[139] Z. Gao *et al.*, “Scalable Production of Sensor Arrays Based on High-Mobility Hybrid Graphene Field Effect Transistors,” *ACS Appl. Mater. Interfaces*, vol. 8, no. 41, pp. 27546–27552, Oct. 2016.

[140] G. Wu, X. Tang, M. Meyyappan, and K. W. C. Lai, “Doping effects of surface functionalization on graphene with aromatic molecule and organic solvents,” *Appl. Surf. Sci.*, vol. 425, pp. 713–721, Dec. 2017.

[141] X. Dong, Y. Shi, W. Huang, P. Chen, and L.J. Li, “Electrical Detection of DNA Hybridization with Single-Base Specificity Using Transistors Based on CVD-Grown Graphene Sheets,” *Adv. Mater.*, vol. 22, no. 14, pp. 1649–1653, Apr. 2010.

[142] E. L. Gui *et al.*, “Electrical detection of hybridization and threading intercalation of deoxyribonucleic acid using carbon nanotube network field-effect transistors,” *Appl. Phys. Lett.*, vol. 89, no. 23, p. 232104, Dec. 2006.

[143] C. J. Shih, G. L. C. Paulus, Q. H. Wang, Z. Jin, D. Blankschtein, and M. S. Strano, “Understanding Surfactant/Graphene Interactions Using a Graphene Field Effect Transistor: Relating Molecular Structure to Hysteresis and Carrier Mobility,” *Langmuir*, vol. 28, no. 22, pp. 8579–8586, Jun. 2012.

[144] Y. W. Tan *et al.*, “Measurement of Scattering Rate and Minimum Conductivity in Graphene,” *Phys. Rev. Lett.*, vol. 99, no. 24, p. 246803, Dec. 2007.

[145] J. H. Chen, C. Jang, S. Adam, M. S. Fuhrer, E. D. Williams, and M. Ishigami, “Charged-impurity scattering in graphene,” *Nat. Phys.*, vol. 4, no. 5, Art. no. 5, May 2008.

[146] C. C. F. Blake, D. F. Koenig, G. A. Mair, A. C. T. North, D. C. Phillips, and V. R. Sarma, “Structure of Hen Egg-White Lysozyme: A Three-dimensional Fourier Synthesis at 2 Å Resolution,” *Nature*, vol. 206, no. 4986, Art. no. 4986, May 1965.

[147] E. Stolyarova *et al.*, “High-resolution scanning tunneling microscopy imaging of mesoscopic graphene sheets on an insulating surface,” *Proc. Natl. Acad. Sci.*, vol. 104, no. 22, pp. 9209–9212, May 2007.

[148] A. K. Geim and K. S. Novoselov, “The rise of graphene,” *Nat. Mater.*, vol. 6, no. 3, pp. 183–191, Mar. 2007.

[149] X. Tang, H. Zhang, X. Tang, and K. W. C. Lai, “Photoresponse enhancement in graphene/silicon infrared detector by controlling photocarrier collection,” *Mater. Res. Express*, vol. 3, p. 076203, Jul. 2016.

[150] C. H. Liu, Y. C. Chang, T. B. Norris, and Z. Zhong, “Graphene photodetectors with ultra-broadband and high responsivity at room temperature,” *Nat. Nanotechnol.*, vol. 9, no. 4, pp. 273–278, Apr. 2014.

[151] P. T. Yin, S. Shah, M. Chhowalla, and K.B. Lee, “Design, Synthesis, and Characterization of Graphene–Nanoparticle Hybrid Materials for Bioapplications,” *Chem. Rev.*, vol. 115, no. 7, pp. 2483–2531, Apr. 2015.

[152] D. Yu and L. Dai, “Self-Assembled Graphene/Carbon Nanotube Hybrid Films for Supercapacitors,” *J. Phys. Chem. Lett.*, vol. 1, no. 2, pp. 467–470, Jan. 2010.

[153] S. Mao, K. Yu, G. Lu, and J. Chen, “Highly sensitive protein sensor based on thermally-reduced graphene oxide field-effect transistor,” *Nano Res.*, vol. 4, no. 10, p. 921, May 2011.

[154] J. Ping, R. Vishnubhotla, A. Vrudhula, and A. T. C. Johnson, “Scalable Production of High-Sensitivity, Label-Free DNA Biosensors Based on Back-Gated Graphene Field Effect Transistors,” *ACS Nano*, vol. 10, no. 9, pp. 8700–8704, Sep. 2016.

[155] S. Mao, K. Yu, G. Lu, and J. Chen, “Highly sensitive protein sensor based on thermally-reduced graphene oxide field-effect transistor,” *Nano Res.*, vol. 4, no. 10, p. 921, May 2011.

[156] M. Liss, B. Petersen, H. Wolf, and E. Prohaska, “An Aptamer-Based Quartz Crystal Protein Biosensor,” *Anal. Chem.*, vol. 74, no. 17, pp. 4488–4495, Sep. 2002.

[157] M. Minunni, S. Tombelli, A. Gullotto, E. Luzi, and M. Mascini, “Development of biosensors with aptamers as bio-recognition element: the case of HIV-1 Tat protein,” *Biosens. Bioelectron.*, vol. 20, no. 6, pp. 1149–1156, Dec. 2004.

[158] C. Nakamura, T. Kobayashi, M. Miyake, M. Shirai, and J. Miyakea, “Usage of a DNA Aptamer as a Ligand Targeting Microcystin,” *Mol. Cryst. Liq. Cryst. Sci. Technol. Sect. Mol. Cryst. Liq. Cryst.*, vol. 371, no. 1, pp. 369–374, Oct. 2001.

[159] W. U. Dittmer, A. Reuter, and F. C. Simmel, “A DNA-based machine that can cyclically bind and release thrombin,” *Angew. Chem. Int. Ed Engl.*, vol. 43, no. 27, pp. 3550–3553, Jul. 2004.

[160] T. G. McCauley, N. Hamaguchi, and M. Stanton, “Aptamer-based biosensor arrays for detection and quantification of biological macromolecules,” *Anal. Biochem.*, vol. 319, no. 2, pp. 244–250, Aug. 2003.

[161] H. Pinto and A. Markevich, “Electronic and electrochemical doping of graphene by surface adsorbates,” *Beilstein J. Nanotechnol.*, vol. 5, no. 1, pp. 1842–1848, Oct. 2014

[162] C.-T. Lin *et al.*, “Label-Free Electrical Detection of DNA Hybridization on Graphene using Hall Effect Measurements: Revisiting the Sensing Mechanism,” *Adv. Funct. Mater.*, vol. 23, no. 18, pp. 2301–2307, Jan. 2013.

[163] S. Islam *et al.*, “Microfluidic-based graphene field effect transistor for femtomolar detection of chlorpyrifos,” *Sci. Rep.*, vol. 9, no. 1, Art. no. 1, Jan. 2019.

[164] M. T. Stubbs and W. Bode, “A player of many parts: the spotlight falls on thrombin’s structure,” *Thromb. Res.*, vol. 69, no. 1, pp. 1–58, Jan. 1993.

[165] W. Berg, B. Hillvärn, H. Arwin, M. Stenberg, and I. Lundström, “The Isoelectric Point of Thrombin and its Behaviour Compared to Prothrombin at Some Solid Surfaces,” *Thromb. Haemost.*, vol. 42, no. 8, pp. 972–982, Oct. 1979.

[166] C. C. Heuck, U. Schiele, D. Horn, D. Fronda, and E. Ritz, “The role of surface charge on the accelerating action of heparin on the antithrombin III-inhibited activity of alpha-thrombin,” *J. Biol. Chem.*, vol. 260, no. 8, pp. 4598–4603, Apr. 1985.

[167] S. Afsahi *et al.*, “Novel graphene-based biosensor for early detection of Zika virus infection,” *Biosens. Bioelectron.*, vol. 100, pp. 85–88, Feb. 2018.

[168] L. Zuccaro *et al.*, “Real-Time Label-Free Direct Electronic Monitoring of Topoisomerase Enzyme Binding Kinetics on Graphene,” *ACS Nano*, vol. 9, no. 11, pp. 11166–11176, Nov. 2015.

[169] J. E. Schiel and D. S. Hage, “Kinetic studies of biological interactions by affinity chromatography,” *J. Sep. Sci.*, vol. 32, no. 10, pp. 1507–1522, Nov. 2009.

[170] E. K. Sackmann, A. L. Fulton, and D. J. Beebe, “The present and future role of microfluidics in biomedical research,” *Nature*, vol. 507, no. 7491, Art. no. 7491, Mar. 2014.

[171] Y. Jiang, S. Zou, and X. Cao, “Rapid and ultra-sensitive detection of foodborne pathogens by using miniaturized microfluidic devices: a review,” *Anal Methods*, vol. 8, no. 37, pp. 6668–6681, Aug. 2016.

[172] D. J. Beebe, G. A. Mensing, and G. M. Walker, “Physics and applications of microfluidics in biology,” *Annu. Rev. Biomed. Eng.*, vol. 4, pp. 261–286, Mar. 2002.

[173] X. Wang, Z. Hao, T. R. Olsen, W. Zhang, and Q. Lin, “Measurements of aptamer–protein binding kinetics using graphene field-effect transistors,” *Nanoscale*, vol. 11, no. 26, pp. 12573–12581, Jul. 2019.

[174] J. Yang, C. Wang, Y. Zhu, G. Liu, and Q. Lin, “A microfluidic aptasensor integrating specific enrichment with a graphene nanosensor for label-free detection of small biomolecules,” in *2015 28th IEEE International Conference on Micro Electro Mechanical Systems (MEMS)*, pp. 569–572, Jan. 2015.

[175] G. Saltzgaber *et al.*, “Scalable graphene field-effect sensors for specific protein detection,” *Nanotechnology*, vol. 24, no. 35, p. 355502, Aug. 2013.

[176] G. Shen, H. Zhang, C. Yang, Q. Yang, and Y. Tang, “Thrombin Ultrasensitive Detection Based on Chiral Supramolecular Assembly Signal-Amplified Strategy Induced by Thrombin-Binding Aptamer,” *Anal. Chem.*, vol. 89, no. 1, pp. 548–551, Jan. 2017.

[177] X. Li *et al.*, “Large-Area Synthesis of High-Quality and Uniform Graphene Films on Copper Foils,” *Science*, vol. 324, no. 5932, pp. 1312–1314, Jun. 2009.

[178] H. Cho *et al.*, “Aptamer-Based SERRS Sensor for Thrombin Detection,” *Nano Lett.*, vol. 8, no. 12, pp. 4386–4390, Dec. 2008.

[179] C.-H. Chu *et al.*, “Beyond the Debye length in high ionic strength solution: direct protein detection with field-effect transistors (FETs) in human serum,” *Sci. Rep.*, vol. 7, no. 1, pp. 1–15, Jul. 2017.

[180] N.-V. Nguyen, C.-H. Yang, C.-J. Liu, C.-H. Kuo, D.-C. Wu, and C.-P. Jen, “An Aptamer-Based Capacitive Sensing Platform for Specific Detection of Lung Carcinoma Cells in the Microfluidic Chip,” *Biosensors*, vol. 8, no. 4, p. 98, Dec. 2018.

[181] W. Yue *et al.*, “An electricity-fluorescence double-checking biosensor based on graphene for detection of binding kinetics of DNA hybridization,” *RSC Adv.*, vol. 7, no. 70, pp. 44559–44567, Sep. 2017.

[182] X. Wang *et al.*, “An aptameric graphene nanosensor for analyte detection in serum,” in *2016 IEEE 29th International Conference on Micro Electro Mechanical Systems (MEMS)*, Jan. 2016, pp. 286–289.

[183] G. I. Dovbeshko, N. Ya. Gridina, E. B. Kruglova, and O. P. Pashchuk, “FTIR spectroscopy studies of nucleic acid damage,” *Talanta*, vol. 53, no. 1, pp. 233–246, Oct. 2000.

[184] Y. Zhu *et al.*, “A graphene-based affinity nanosensor for detection of low-charge and low-molecular-weight molecules,” *Nanoscale*, vol. 8, no. 11, pp. 5815–5819, Mar. 2016.

[185] R. Gesztelyi, J. Zsuga, A. Kemeny-Beke, B. Varga, B. Juhasz, and A. Tosaki, “The Hill equation and the origin of quantitative pharmacology,” *Arch. Hist. Exact Sci.*, vol. 66, no. 4, pp. 427–438, Jul. 2012.

[186] J. N. Weiss, “The Hill equation revisited: uses and misuses,” *FASEB J.*, vol. 11, no. 11, pp. 835–841, Sep. 1997.

[187] X. Li *et al.*, “Electrochemical impedance spectroscopy for study of aptamer–thrombin interfacial interactions,” *Biosens. Bioelectron.*, vol. 23, no. 11, pp. 1624–1630, Jun. 2008.

[188] Z. Hao *et al.*, “Modulating the Linker Immobilization Density on Aptameric Graphene Field Effect Transistors Using an Electric Field,” *ACS Sens.*, vol. 5, no. 8, pp. 2503–2513, Aug. 2020.

[189] C. Diacci *et al.*, “Label-free detection of interleukin-6 using electrolyte gated organic field effect transistors,” *Biointerphases*, vol. 12, no. 5, p. 05F401, Sep. 2017.

[190] W. Gao *et al.*, “Fully integrated wearable sensor arrays for multiplexed *in situ* perspiration analysis,” *Nature*, vol. 529, no. 7587, pp. 509–514, Jan. 2016.

[191] K. Guk *et al.*, “Evolution of Wearable Devices with Real-Time Disease Monitoring for Personalized Healthcare,” *Nanomater. Basel Switz.*, vol. 9, no. 6, May 2019.

[192] J. Kim, A. S. Campbell, B. E.F. de Ávila, and J. Wang, “Wearable biosensors for healthcare monitoring,” *Nat. Biotechnol.*, vol. 37, no. 4, pp. 389–406, Apr. 2019.

[193] M. Chung, G. Fortunato, and N. Radacsi, “Wearable flexible sweat sensors for healthcare monitoring: a review,” *J. R. Soc. Interface*, vol. 16, no. 159, p. 20190217, Oct. 2019.

[194] Z. Wang *et al.*, “An Ultraflexible and Stretchable Aptameric Graphene Nanosensor for Biomarker Detection and Monitoring,” *Adv. Funct. Mater.*, vol. 29, no. 44, p. 1905202, Nov. 2019.

[195] M. Z. Pakhuruddin, K. Ibrahim, and A. A. Aziz, “Properties of polyimide substrate for applications in flexible solar cells,” *Optoelectron. Adv. Mater. - Rapid Commun.*, vol. 7, no. May-June 2013, pp. 377–380, Jun. 2013.

[196] P. Taptimthong, J. Rittinger, M. C. Wurz, and L. Rissing, “Flexible Magnetic Writing / Reading System: Polyimide Film as Flexible Substrate,” *Procedia Technol.*, vol. 15, pp. 230–237, Jan. 2014.

[197] S. Xu *et al.*, “Real-time reliable determination of binding kinetics of DNA hybridization using a multi-channel graphene biosensor,” *Nat. Commun.*, vol. 8, p. 14902, Mar. 2017.

[198] S. Islam *et al.*, “Microfluidic-based graphene field effect transistor for femtomolar detection of chlorpyrifos,” *Sci. Rep.*, vol. 9, no. 1, Art. no. 1, Jan. 2019.

[199] S. Ghosh, N. I. Khan, J. G. Tsavalas, and E. Song, “Selective Detection of Lysozyme Biomarker Utilizing Large Area Chemical Vapor Deposition-Grown Graphene-Based Field-Effect Transistor,” *Front. Bioeng. Biotechnol.*, vol. 6, pp. 1–7, Mar. 2018.

[200] S. Wang *et al.*, “Graphene field-effect transistor biosensor for detection of biotin with ultrahigh sensitivity and specificity,” *Biosens. Bioelectron.*, vol. 165, p. 112363, Oct. 2020.

[201] K. H. Kim *et al.*, “High-performance portable graphene field-effect transistor device for detecting Gram-positive and -negative bacteria,” *Biosens. Bioelectron.*, vol. 167, p. 112514, Nov. 2020.

[202] X. Wang, Z. Hao, T. R. Olsen, W. Zhang, and Q. Lin, “Measurements of aptamer–protein binding kinetics using graphene field-effect transistors,” *Nanoscale*, vol. 11, no. 26, pp. 12573–12581, Jul. 2019.

[203] Guangfu Wu, Xin Tang, M. Meyyappan, and K. W. C. Lai, “Chemical functionalization of graphene with aromatic molecule,” in *2015 IEEE 15th International Conference on Nanotechnology (IEEE-NANO)*, pp. 1324–1327, Jul. 2015.

[204] N. I. Khan, M. Mousazadehkasin, S. Ghosh, J. G. Tsavalas, and E. Song, “An integrated microfluidic platform for selective and real-time detection of thrombin biomarkers using a graphene FET,” *Analyst*, vol. 145, no. 13, pp. 4494–4503, Jun. 2020.

[205] M. M. Heravi, M. Ghavidel, and L. Mohammadkhani, “Beyond a solvent: triple roles of dimethylformamide in organic chemistry,” *RSC Adv.*, vol. 8, no. 49, pp. 27832–27862, 2018.

[206] J. Lin, Z. Zhu, C. F. Cheung, F. Yan, and G. Li, “Digital manufacturing of functional materials for wearable electronics,” *J. Mater. Chem. C*, vol. 8, no. 31, pp. 10587–10603, Aug. 2020.

[207] J. N. Lee, C. Park, and G. M. Whitesides, “Solvent Compatibility of Poly(dimethylsiloxane)-Based Microfluidic Devices,” *Anal. Chem.*, vol. 75, no. 23, pp. 6544–6554, Dec. 2003.

[208] N. I. Khan and E. Song, “Lab-on-a-Chip Systems for Aptamer-Based Biosensing,” *Micromachines*, vol. 11, no. 2, Art. no. 2, Feb. 2020.

[209] S. Farid *et al.*, “Detection of Interferon gamma using graphene and aptamer based FET-like electrochemical biosensor,” *Biosens. Bioelectron.*, vol. 71, pp. 294–299, Sep. 2015.

[210] S. Narayanan, J. Gall, and C. Richert, “Clamping down on weak terminal base pairs: oligonucleotides with molecular caps as fidelity-enhancing elements at the 5’- and 3’-terminal residues,” *Nucleic Acids Res.*, vol. 32, no. 9, pp. 2901–2911, 2004.

[211] “Labeling-Amine-Modified-Aptamers-Base-Pait-Bio.pdf.” Available: https://www.basepairbio.com/wp-content/uploads/2014/09/Labeling-Amine-Modified-Aptamers-Base-Pait-Bio.pdf. Accessed: Nov. 30, 2020. [Online].

[212] A. Sharma, A. Hayat, R. K. Mishra, G. Catanante, S. Bhand, and J. L. Marty, “Titanium Dioxide Nanoparticles (TiO2) Quenching Based Aptasensing Platform: Application to Ochratoxin A Detection,” *Toxins*, vol. 7, no. 9, Art. no. 9, Sep. 2015.

[213] F. Schwierz, “Graphene transistors,” *Nat. Nanotechnol.*, vol. 5, no. 7, Art. no. 7, Jul. 2010.

[214] A. Béraud, M. Sauvage, C. M. Bazán, M. Tie, A. Bencherif, and D. Bouilly, “Graphene field-effect transistors as bioanalytical sensors: design, operation and performance,” *Analyst*, Nov. 2020.

[215] I. Novodchuk, M. Bajcsy, and M. Yavuz, “Graphene-based field effect transistor biosensors for breast cancer detection: A review on biosensing strategies,” *Carbon*, vol. 172, pp. 431–453, Feb. 2021.

[216] Y. Li, Y. Zhu, C. Wang, M. He, and Q. Lin, “Selective detection of water pollutants using a differential aptamer-based graphene biosensor,” *Biosens. Bioelectron.*, vol. 126, pp. 59–67, Feb. 2019.

[217] G. Wu *et al.*, “Graphene Field-Effect Transistors for the Sensitive and Selective Detection of Escherichia coli Using Pyrene-Tagged DNA Aptamer,” *Adv. Healthc. Mater.*, vol. 6, no. 19, Oct. 2017.

[218] A. Svetlova, D. Kireev, D. Mayer, and A. Offenhaeusser, “Origins of leakage currents on electrolyte-gated graphene field-effect transistors,” *ArXiv201105913 Cond-Mat*, Nov. 2020, Accessed: Dec. 07, 2020. [Online]. Available: http://arxiv.org/abs/2011.05913.

[219] X. Zhang *et al.*, “Ultrasensitive Field-Effect Biosensors Enabled by the Unique Electronic Properties of Graphene,” *Small*, vol. 16, no. 15, p. 1902820, 2020.

[220] P. Joshi, H. E. Romero, A. T. Neal, V. K. Toutam, and S. A. Tadigadapa, “Intrinsic doping and gate hysteresis in graphene field effect devices fabricated on SiO2substrates,” *J. Phys. Condens. Matter*, vol. 22, no. 33, p. 334214, Aug. 2010.

[221] Z.-M. Liao, B.-H. Han, Y.-B. Zhou, and D.-P. Yu, “Hysteresis reversion in graphene field-effect transistors,” *J. Chem. Phys.*, vol. 133, no. 4, p. 044703, Jul. 2010.

[222] H. Wang, Y. Wu, C. Cong, J. Shang, and T. Yu, “Hysteresis of Electronic Transport in Graphene Transistors,” *ACS Nano*, vol. 4, no. 12, pp. 7221–7228, Dec. 2010.

[223] Z. Hao *et al.*, “Modulating the Linker Immobilization Density on Aptameric Graphene Field Effect Transistors Using an Electric Field,” *ACS Sens.*, vol. 5, no. 8, pp. 2503–2513, Aug. 2020.

[224] Z. Hao, Y. Pan, W. Shao, Q. Lin, and X. Zhao, “Graphene-based fully integrated portable nanosensing system for on-line detection of cytokine biomarkers in saliva,” *Biosens. Bioelectron.*, vol. 134, pp. 16–23, Jun. 2019.

[225] J. Huang, J. Harvey, W. H. D. Fam, M. A. Nimmo, and I. Y. A. Tok, “Novel Biosensor for InterLeukin-6 Detection,” *Procedia Eng.*, vol. 60, pp. 195–200, Jan. 2013.

[226] J. Y. Lichtenberg, Y. Ling, and S. Kim, “Non-Specific Adsorption Reduction Methods in Biosensing,” *Sensors*, vol. 19, no. 11, Jan. 2019.

[227] N. Gao *et al.*, “Specific detection of biomolecules in physiological solutions using graphene transistor biosensors,” *Proc. Natl. Acad. Sci.*, vol. 113, no. 51, pp. 14633–14638, Dec. 2016.

[228] Y. Liang, X. Liang, Z. Zhang, W. Li, X. Huo, and L. Peng, “High mobility flexible graphene field-effect transistors and ambipolar radio-frequency circuits,” *Nanoscale*, vol. 7, no. 25, pp. 10954–10962, Jun. 2015.

[229] Z. Hao *et al.*, “Measurement of cytokine biomarkers using an aptamer-based affinity graphene nanosensor on a flexible substrate toward wearable applications,” *Nanoscale*, vol. 10, no. 46, pp. 21681–21688, Nov. 2018.

[230] J. Fernández-Rossier, J. J. Palacios, and L. Brey, “Electronic structure of gated graphene and graphene ribbons,” *Phys. Rev. B*, vol. 75, no. 20, p. 205441, May 2007.

[231] R. Gesztelyi, J. Zsuga, A. Kemeny-Beke, B. Varga, B. Juhasz, and A. Tosaki, “The Hill equation and the origin of quantitative pharmacology,” *Arch. Hist. Exact Sci.*, vol. 66, no. 4, pp. 427–438, Jul. 2012.

[232] J. N. Weiss, “The Hill equation revisited: uses and misuses.,” *FASEB J.*, vol. 11, no. 11, pp. 835–841, Sep. 1997.

[233] M. B. Lerner *et al.*, “Scalable Production of Highly Sensitive Nanosensors Based on Graphene Functionalized with a Designed G Protein-Coupled Receptor,” *Nano Lett.*, vol. 14, no. 5, pp. 2709–2714, May 2014.

[234] J. Ping, R. Vishnubhotla, A. Vrudhula, and A. T. C. Johnson, “Scalable Production of High-Sensitivity, Label-Free DNA Biosensors Based on Back-Gated Graphene Field Effect Transistors,” *ACS Nano*, vol. 10, no. 9, pp. 8700–8704, Sep. 2016.

APPENDIX A

A.1. Calculation of Printed Volume of CNT-Aptamer Ink

Number of droplets printed on a 4 mm length = $\frac{4.0\ \text{mm}}{20\times10^{-3}\ \text{mm}}$ = 200

Total number (#) of droplets in the 4 mm square = $(200)^2$ = 40,000

# of droplets in the 4mm diameter circular electrode = $\frac{\pi r^2}{d^2} \times 40000 = 31416$, where $r = \frac{d}{2}$

Hence, the amount of ink per layer printed on the electrode = $31416 \times 10\ \text{pL} = 0.31416\ \mu\text{L} \approx$ 315 nL.

A.2. Lysozyme Binding Confirmation

To confirm that lysozyme binds to the aptamer, we performed lysozyme binding experiments with MB-labelled thiolated DNA aptamers on gold rod electrode. The electrochemical DNA-based lysozyme sensor was fabricated on a 3 mm gold rod electrode (A-002421, Bio-Logic USA Science Instruments, TN, USA) using a previously described method [244]. The experiments were performed using Ag/AgCl as the reference electrode and platinum as the counter electrode. The results are presented in Figure A2.

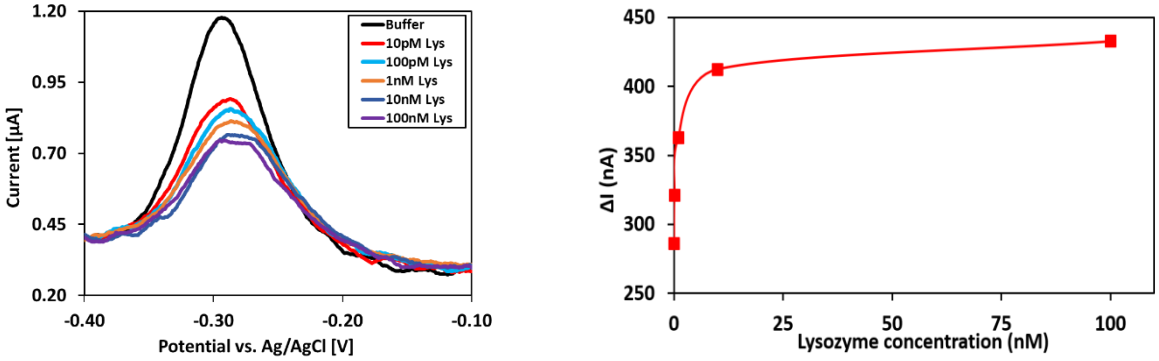

(**a**) (**b**)

Figure A2. Square wave voltammograms obtained for different concentrations of lysozyme in 10 mM PBS buffer.

It can be seen that, when lysozyme is exposed to the aptamer-modified gold electrode, the peak current reduces until it reaches saturation for higher concentration of lysozyme. These results suggest specific binding of lysozyme to the aptamer-based recognition element [245], [246].

In the absence of lysozyme, the MB-labelled aptamer probes are relatively flexible; allowing the attached MB to collide with the electrode that enables efficient electron transfer from the MB to the electrode. This is in accordance with the relatively high voltammetric peak current for the reversible reduction of MB as characterized using square wave voltammetry (SWV). When lysozyme binds to the aptamer due to the specific affinity, the aptamer undergoes conformational change that alters the electron tunneling distance hindering the charge transfer from the MB to the electrode. As a result, the voltametric peak current decreases.

A.3. Chronocoulometric Experiments

To perform chronoloculometry, the printed sensor was incubated in 1mM RuHex in 10 mM Tris-HCl solution for 1 h. During the incubation, RuHex ions electrostatically bind to the negative backbones of the DNA aptamers. The number of probe molecules are thus proportional to the number of bound RuHex ions to the DNA probes. After RuHex incubation, the electrode is then washed thoroughly in DI water to remove the unbound RuHex ions.

We first characterized the redox reaction of RuHex at the printed electrode using cyclic voltammetry (CV). The CV curves are presented in Figure A3(a) before and after the RuHex incubation. The two CV peaks with almost zero peak separation in the presence of RuHex indicates the electrostatically bound RuHex ions to the backbones of the surface-confined DNAs [247]. Figure A3(b) displays the CC curves at the printed electrode in the presence and absence of 1 mM RuHex. Q_{SE} is obtained from the CC intercepts at $t = 0$ and the surface density of probe DNAs can be calculated using Equations (4) and (5) in Section 3.3 where $z = 3$ and $m = 30$ in our case.

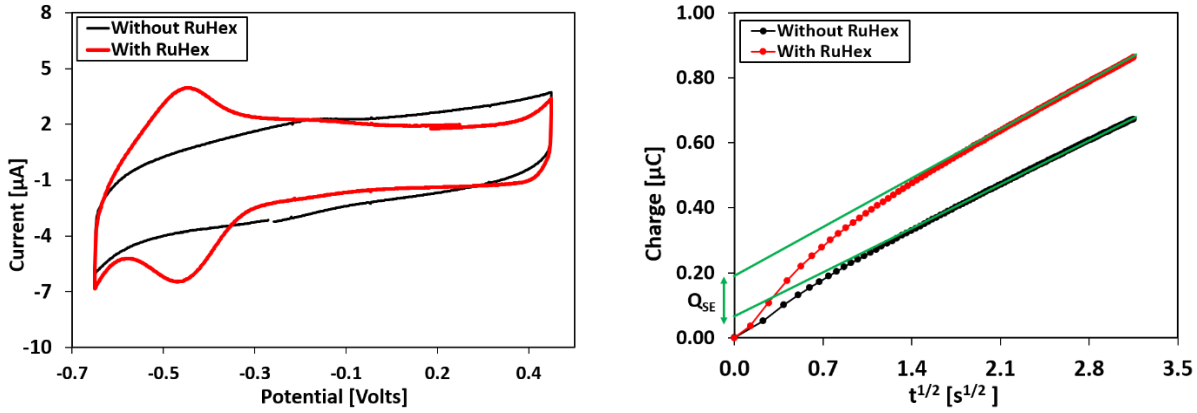

(**a**) (**b**)

Figure A3. (a) Cyclic voltammograms (scan rate: 500 mV/s); and (**b**) CC responses curves of printed electrode in the presence (red) and absence (black) of RuHex.

A.4. LOD Calculation

The limit of detection (LOD) can be calculated by the following equation [248]:

$$LoD = \frac{3.3 \times Stabdard\ deviation\ at\ 0\frac{\mu g}{mL} Lys\ concentration}{Slope\ of\ the\ calibration\ curve\ at\ 0\frac{\mu g}{mL} Lys\ concentration}$$

$$= \frac{3.3 \times 1.97}{71.89\ mL/\mu g} = 90.4\ \text{ng/mL}$$

A.5. Effect of number of printed layers on sensor responses

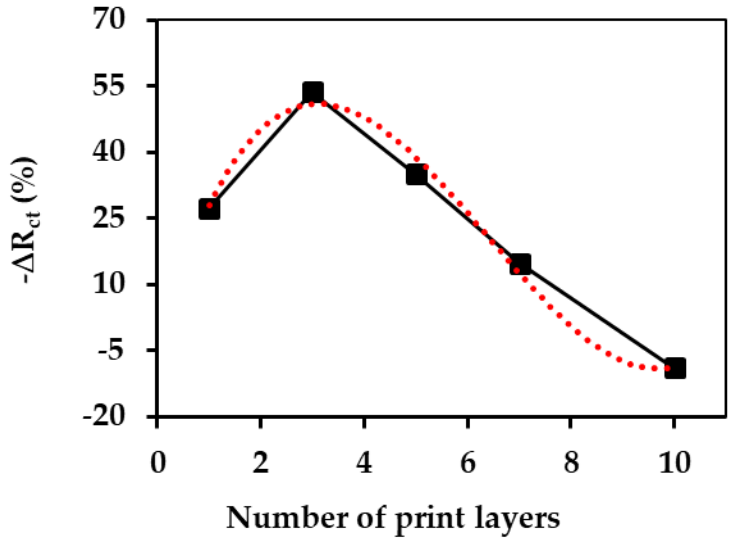

Figure A4. Comparison of the sensor responses as a function of the different printing layers. Each sensor was exposed to 1 µg/mL of lysozyme protein.

APPENDIX B

B.1. Lysozyme Binding Confirmation

Lysozyme binding to the aptamers was confirmed by performing experiments with methylene blue (MB)-labelled thiolated DNA aptamers (LGC Biosearch Technologies, CA, USA) with the same sequence as used by Ellington *et al*. [122] on gold rod electrode. The DNA-based electrochemical lysozyme sensor was fabricated on a gold rod electrode (A-002421, Bio-Logic USA Science Instruments, TN, USA) of 3 mm diameter using a previously described method [244]. The experiments were performed in a 3-electrode electrochemical cell with Ag/AgCl as the reference electrode and platinum as the counter electrode. The results are presented in Figure B1.

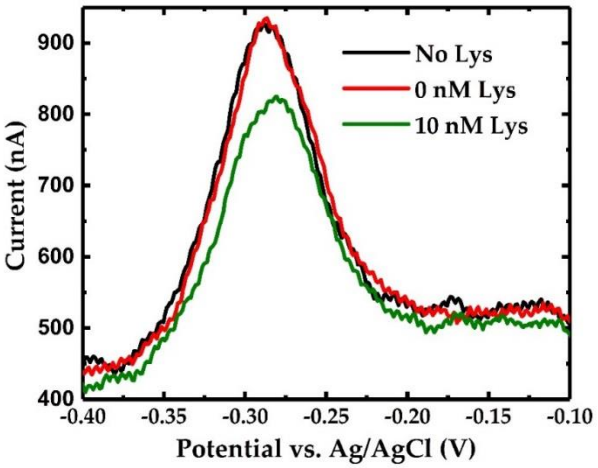

Figure B1. Square wave voltammograms obtained for different concentrations of lysozyme in 0.01X PBS.

It can be seen from Supplementary Figure B1 that the peak current reduces when lysozyme is exposed to the aptamer-modified gold electrode which suggests that specific binding of lysozyme to the aptamer-based recognition element has occurred [245], [246]. In the absence of lysozyme, the MB-labels are easily accessible to the electrode which enables efficient electron transfer between the MB and the electrode. This causes high voltammetric peak current for the reduction of MB as characterized using square wave voltammetry (SWV). When lysozyme comes in proximity to the aptamers, due to the specific affinity the aptamers undergo conformational change

to capture the proteins. This alters the electron tunneling distance hindering the charge transfer from the MB to the electrode. As a result, the voltammetric peak current decreases.

APPENDIX C

C.1. Device Fabrication

C.1.1. Graphene transfer

To transfer graphene onto the substrate, the monolayer graphene on polymer film was immersed in deionized water slowly while the graphene film protected by the sacrificial layer was detached from the support polymer film and remained floating on the water. The floating sacrificial layer/graphene layer was then collected by the patterned gold electrode substrate which was then dried at room temperature for 30 minutes followed by annealing on hot plate at 150 °C for 1 hour. To remove the top sacrificial layer, the sample was then treated with acetone for 1 hour followed by dipping into ethanol for another 1 hour. Finally, the sample was dried with an air gun and thermally annealed in an oven at 300 °C in argon atmosphere for 2 hours.

C.1.2. Microfluidic channel fabrication

The microfluidic channel was fabricated with a PDMS block using the cast molding technique [180]. For this, an SU-8 (MicroChem Corp.) master mold with the desired channel pattern (width: 600 µm, height: 100 µm) was formed on silicon wafer surface. The degassed mixture of PDMS prepolymer and curing agent (Sylgard 184) mixed at a weight ratio of 10:1 was poured on the prepared master mold. Then the PDMS block was cured at 60 °C for 4 hours and then peeled off from the SU-8 mold.

C.2. GFET Devices Labels

Table C1: Summary of the labels for the 6 GFET devices in the microfluidic-integrated GFET device.

Device #	Source/Drain electrodes	Gate electrode

GFET- 1	2/3	1
GFET- 2	3/4	1
GFET- 3	4/5	1
GFET- 4	6/7	10
GFET- 5	7/8	10
GFET- 6	8/9	10

C.3. Aptamer Packing Density Estimation

The change of surface charge (ΔQ) can be expressed as [197],

$$\Delta Q = C \times \Delta V_D \quad (1)$$

Where, ΔV_D is the shift in Dirac voltage, and C is the total gate capacitance, which can be expressed in by the following equation [197]:

$$\frac{1}{C} = \frac{1}{C_{G1}} + \frac{1}{C_{G2}} + \frac{1}{C_Q} \quad (2)$$

Where, C_{G1} and, C_{G2} are the geometrical capacitances formed due to the electrical double layer capacitances on different interfaces and denote the capacitance between the graphene and solution, and the capacitance between the gate electrode and solution, respectively. d_1 and d_2 represent the plate distances for C_{G1} and C_{G2}, respectively where $d_1 = d_2 = d =$ Debye length. C_Q which is related to the Fermi level shift, denotes the quantum capacitance of graphene associated with finite density of states due to Pauli principle [230].

From the model of parallel plate capacitors, we can write the following expressions for C_{G1} and C_{G2}.

$$C_{G1} = \frac{S_{graphene}\varepsilon_r\varepsilon_0}{d} \text{ and } C_{G2} = \frac{S_{gate}\varepsilon_r\varepsilon_0}{d}$$

where, $S_{graphene}$ is the contact area between the electrolyte and graphene monolayer, S_{gate} is the contact area between the electrolyte and gold gate electrode, ε_0 is the vacuum permittivity ($8.854 \times 10^{-12}\ F/m$) and ε_r is the relative dielectric constant of PBS solution (80). Estimated Debye length for a 0.01× PBS buffer concentration, $d = 7.3\ nm$.

$S_{graphene}$ can be expressed as:

$$S_{graphene} = L_{gf} \times W_{mc}$$

where, L_{gf} is length of the graphene film which equals to 5 mm or 5000 µm and W_{mc} is the width of the microfluidic channel that equals to 600 µm. Therefore,

$$S_{graphene} = 3{,}000{,}000\ \mu m^2.$$

Similarly, S_{gate} can be expressed as:

$$S_{gate} = L_{gate} \times W_{mc}$$

where, L_{gate} is the width of each gate electrode which equals to 100 µm and W_{mc} is the width of the microfluidic channel that equals to 600 µm. Therefore,

$$S_{gate} = 100 \times 600 = 60{,}000\ \mu m^2.$$

Therefore, the geometrical capacitance values can be calculated as:

$$C_{G1} = \frac{S_{graphene}\varepsilon_r\varepsilon_0}{d} = \frac{3{,}000{,}000 \times 10^{-12} \times 80 \times 8.854 \times 10^{-12}}{7.3 \times 10^{-9}} = 291.1\ \text{nF}$$

$$C_{G2} = \frac{S_{gate}\varepsilon_r\varepsilon_0}{d} = \frac{60{,}000 \times 10^{-12} \times 80 \times 8.854 \times 10^{-12}}{7.3 \times 10^{-9}} = 5.822\ \text{nF}$$

The total geometrical capacitance (C_{TG}) can be calculated as the series combination of C_{G1} and C_{G2} and the value yields, $C_{TG} = 57.08\ nF$.

The quantum capacitance C_Q can be expressed as:

$$C_Q = C_{q\times} S_{graphene}$$

where C_q is the quantum capacitance per unit area and the value is ~ 2 µF/cm^2 [197] . Therefore, $C_Q = 0.6$ nF.

Now, the total gate capacitance, C can be calculated from Equation (2) as: C= 0.593 nF.

From **Figure** 6.3D, the attachment of 27-mer thrombin-binding aptamer leads to a Dirac voltage shift, ΔV_{Dirac}= 403.9 mV.

$$\text{So, } \Delta Q = C \times \Delta V_D = 0.593 \times 10^{-9} \times 403.9 \times 10^{-3} = 2.4 \times 10^{-10}\ \text{C}.$$

If the probe density is n, ΔQ can be written as:

$$\Delta Q = 27neS_{graphene}$$

$$\Rightarrow \quad n=\frac{\Delta Q}{27eS_{graphene}}=\frac{2.4\times10^{-10}}{27\times1.6\times10^{-19}\times3000000\times10^{-12}}=1.85\times10^{13}/m^2=1.85\times10^{9}/cm^2.$$

Therefore, the aptamer probe density can be estimated to be $1.85\times10^{9}/cm^2$. This is equivalent to 232 nm aptamer probe spacing which is comparable to other reported values in literature [154].

C.4. Control Experiments

To examine the inertness of the bare graphene to thrombin, a set of control experiments were performed by exposing bare graphene to thrombin solution of various concentrations. The measured transfer curves are presented in Figure C1. It can be seen that there is no significant shift in the Dirac voltage, indicating non-responsive behavior of bare unmodified graphene to thrombin.

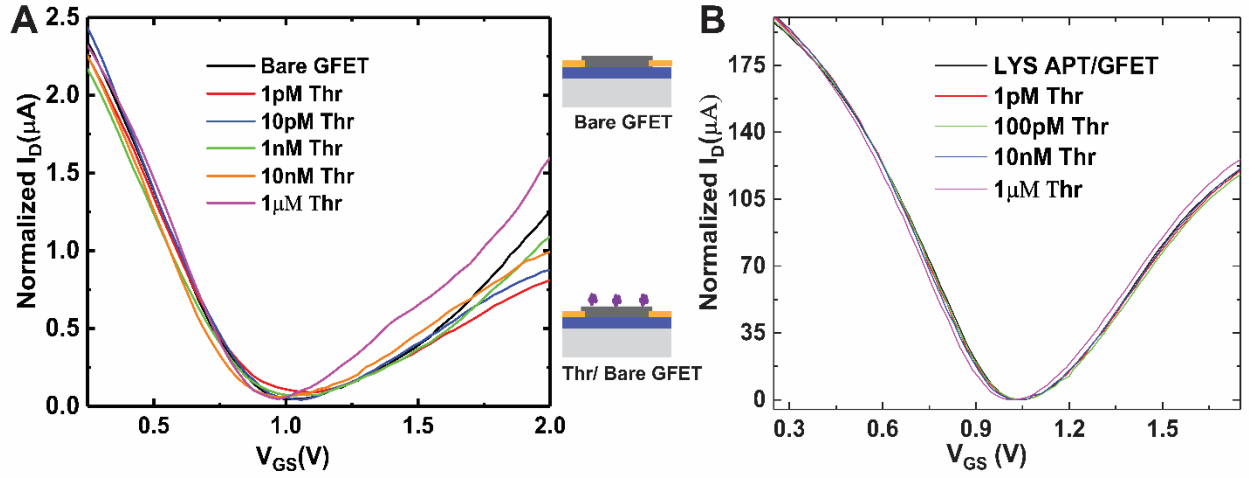

Figure C1: Control experiments. I_D-V_{GS} transfer curves of (A) bare graphene, and (B) lysozyme (LYS) aptamer modified graphene exposed to different concentrations (from 1 pM to 1 μM) of thrombin.

C.5. Calculation of Limit of Detection (LOD)

Limit of detection can be calculated according to the following equation:

$$LOD=\frac{3.3\times standard\ deviation\ at\ the\ lowest\ concetration\ measured}{Slope\ of\ the\ calibration\ curve}$$

$$=\frac{3.3\times11.8521}{14.8715}=2.63\ \text{pM}$$

C.6. Calculation of the Transconductance, g_m

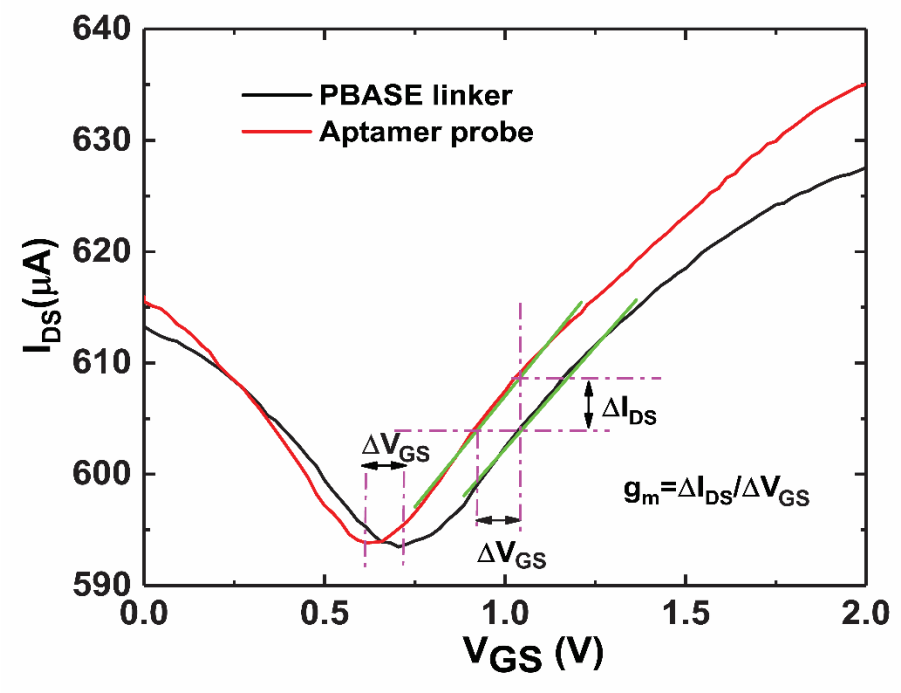

Figure C2. Calculation of transconductance

C.7. Current Calibration Curve from Transient Measurements

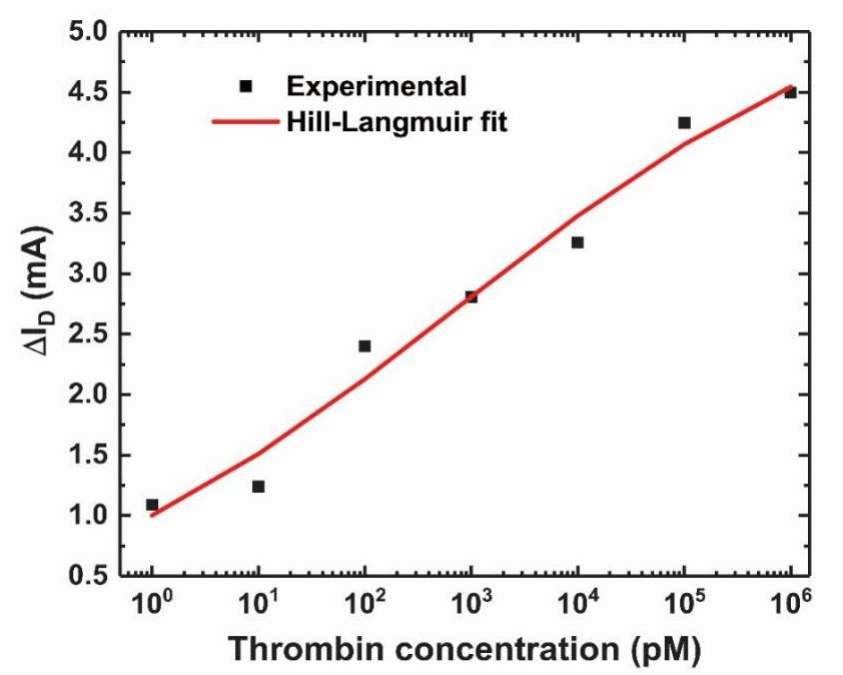

Figure C3. The concentration-dependent drain current (I_D) calibration plot and its Hill-Langmuir fit curve (R^2 = 97.78%).

The data can be fitted by the same Hill-Langmuir equation in the current domain:

$$\Delta I_D = \frac{I_0 + I_m \left(\frac{x}{K_D}\right)^n}{1 + \left(\frac{x}{K_D}\right)^n}$$

Table C2 summarizes the best fit (R^2=0.9778) values of the Hill-Langmuir equation. It gives a dissociation constant of K_D = 0.7317 nM which is comparable to the value obtained from the voltage calibration curve.

Table C2. Summary of the Hill Langmuir fitting parameters of the current calibration curve in Figure C3.

Hill-Langmuir parameters	**Value**	**Error**
$\boldsymbol{I_0}$	-0.1729 µA	±2.6456 µA
$\boldsymbol{I_m}$	5.6025 µA	±2.3776 µA
$\boldsymbol{K_D}$	0.7317 nM	±1.8664 nM
$\boldsymbol{n}$	0.2070	±0.2193

APPENDIX D

D.1. Confirmation of the presence of DNA nucleobases in the synthesized product

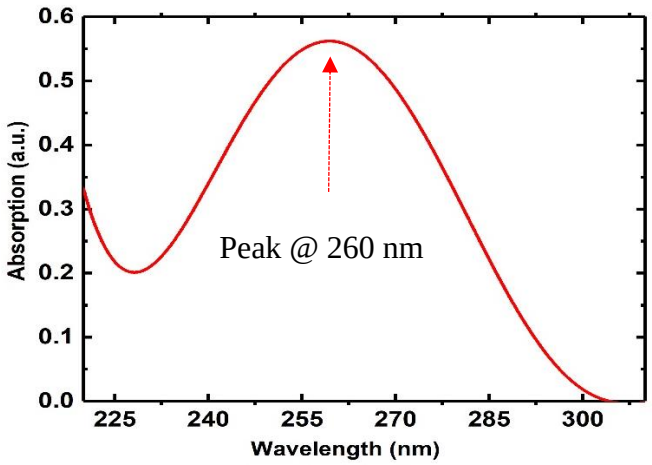

Figure D1. UV-visible spectrum of the pyrene tagged DNA aptamer. The peak at 260 nm is the characteristic DNA peak that corresponds to the presence of DNA nucleobases in the synthesized product.

D2. Leakage current and hysteresis in the GFET transfer curve

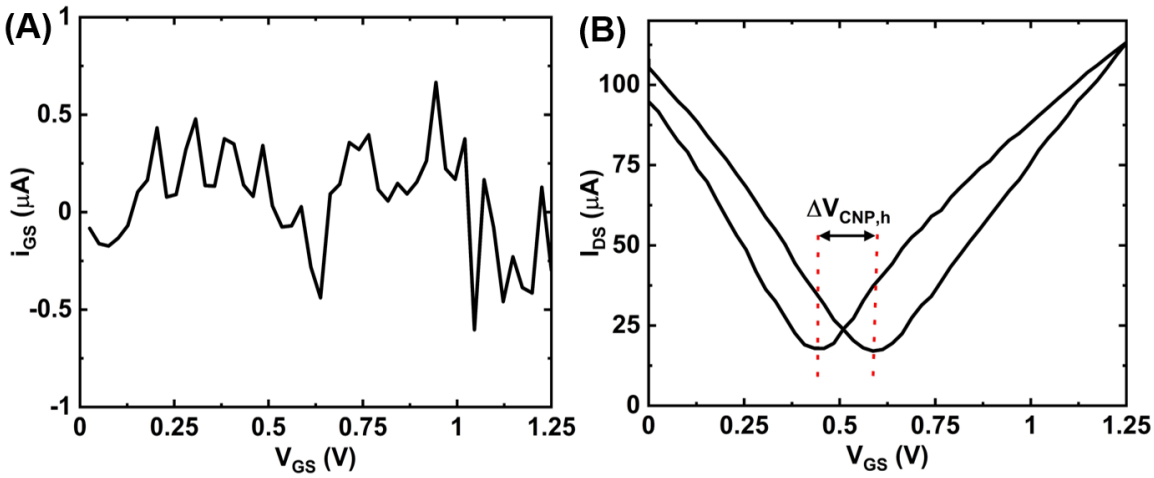

Figure D2. Measurement data for a gate (Pt) electrode: (A) gate leakage (I_{GS}) vs gate-source voltage (V_{GS}), and (B) I_{DS}-V_{GS} transfer curve showing the amount of hysteresis ($\Delta V_{CNP,h}$).

D3. Hill-Langmuir fitting of aptamer-protein equilibrium binding

The calibration curve profile presented in Figure 8.8 can be best modeled by the Hill-Langmuir equation that describes the equilibrium binding of a ligand by a receptor [231]–[233]:

$$r = \frac{r_0 + r_m \left(\frac{c}{K_D}\right)^n}{1 + \left(\frac{c}{K_D}\right)^n}$$

where r_0 represents the estimated minimum response while all the binding sites are empty, r_m is the estimated maximum response while the binding sites are occupied, c indicates the target concentration, K_D is the effective dissociation constant which is defined as the concentration where half of the available binding sites are occupied, and n represents the Hill coefficient.

Table 1 summarizes the values of the parameters that result in the best fit (R^2 = 0.9925) for the Hill-Langmuir model of the calibration curve. A Hill coefficient value of n = 0.3 (which should be close to 1 under ideal conditions) indicates a decreased binding affinity with the target which may be caused by the interactions among the neighboring proteins or by the increased charge carrier scattering as more ligand bindings occur on the graphene surface [137], [234]. The best fit value of $K_D = 3.4 \pm 2$ nM is nearly identical to the value reported by the aptamer manufacturer. Based on the obtained calibration curve, the limit of detection (LOD) of our sensor is calculated to be ~8 pM.

Table 1: Summary of the Hill-Langmuir fitting parameters of the calibration curve.

Hill-Langmuir parameters	**Value**	**Error**
$\boldsymbol{r_0}$	-9.6 %	±3.1 %
$\boldsymbol{r_m}$	179.4 %	±18.6 mV
$\boldsymbol{K_D}$	3.4 nM	±2 nM
$\boldsymbol{n}$	0.3	±0.03

D4. Specificity test with a random sequence aptamer

To test the specificity of the GFET sensor, the GFET was functionalized with a randomized aptamer sequence using the same one-step functionalization protocol as the IL-6 aptamer. The sequence of the randomized single-stranded DNA was: ATCAGGGCTAAAGAGTGCAGAGTTACTTAG. Following functionalization, the aptamer modified GFET was exposed to different concentrations (1, 10 and 100 nM) of IL-6 protein. The results are presented in Figure D3, which shows no significant shift of the charge neutrality point upon exposure of the IL-6 protein. This is due to the fact that the random sequence aptamer does not exhibit high affinity toward IL-6 protein suggesting the specificity of our sensor toward the target protein IL-6.

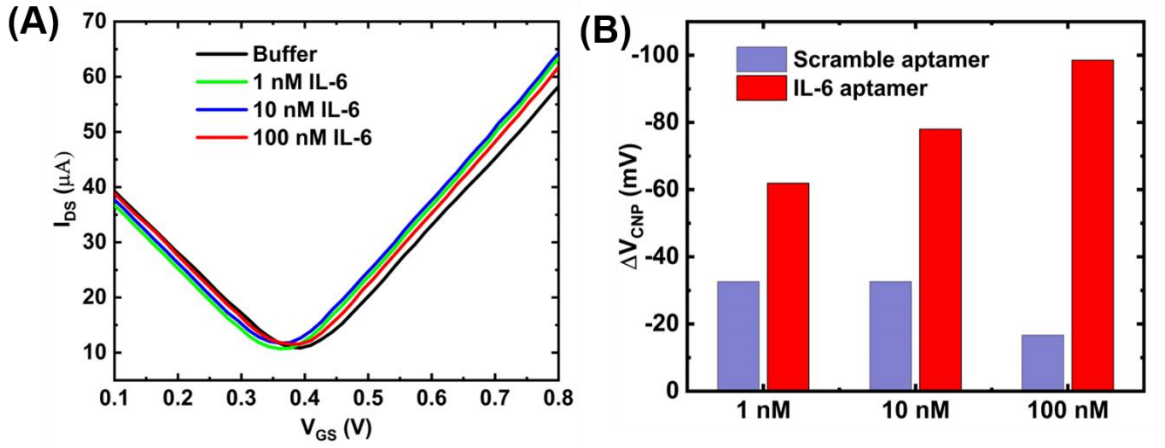

Figure D3: Scramble aptamer test: (A) GFET measurements of the scramble aptamer modified GFET upon exposure of different concentrations of IL-6 protein, and (B) Comparative bar chart showing the response of IL-6 protein to the aptamer-modified GFET.